SIMULATION AND NUMERICAL MODELLING OF THREE-PHASE FLOW IN AUTOMOTIVE HIGH-PRESSURE FUEL INJECTORS

Thesis submitted for the fulfilment of
the requirements for the Degree of
Doctor of Philosophy

by

Eduardo Gomez Santos

Advanced Gasoline Components

Delphi Technologies, Luxembourg

School of Mathematics, Computer Science & Engineering

City, University of London

May, 2020

Abstract

In the last 20 years the automotive industry has managed an impressive reduction in emissions, in agreement to relevant regulations. One key component in achieving lower emissions is the fuel injector nozzle. This PhD Thesis aims to present an experimentally validated computational fluid dynamics (CFD) method able to better describe the flow developing inside Diesel and gasoline fuel direct injection nozzles. The compressible Navier-Stokes equations are numerically solved considering the vertical motion of the injector's needle valve. A homogenous three-phase (liquid, vapour and air) barotropic equation of state linking the variation of density and pressure is implemented into the utilised flow solver. This model is able to capture cavitation and its collapse as well as the air entrainment inside the injector taking place in between successive injection events. The flow turbulence is modelled using LES, in order to better understand the details of the physical processes, and URANS, as a suitable method for industry product development time scales and the available CPU resources. For the case of Diesel fuel injection, high-speed visualisations of a transparent nozzle tip replica are used to validate the proposed methodology. The numerical simulations describe the interaction between the vortex flow and cavitation formation that take place simultaneously with air entrainment from the surrounding environment into the injector's sac volume during the injection and the dwell time between successive injections. The experimentally observed flow phenomena are well predicted by the simulation model, namely, the compression of pre-existing air bubbles inside the injector's sac volume during the injector opening, cavitation vapour condensation and air suction after the needle closure. In the case of Gasoline direct injection (GDi) nozzles operated with ethanol (E100) fuel, emphasis is put on the prediction of erosion sites. E100 represents a challenge to the durability of the fuel injection system components since it can result in corrosion which is further enhanced by cavitation induced erosion as a result of the collapse of vapour structures. CFD predictions for both the flow development and the locations prone to cavitation erosion inside GDi injectors are reported. The CFD simulations predict the flow structures leading to the observed erosion locations in the nozzle. Three cavitation erosion indices reported in literature are evaluated against new experimental data of erosion damage. Scanning electron microscope erosion images are found to correlate well with the accumulated erosive power predicted by the simulation.

Acknowledgements

In the first place I would like to thank Dr. -Ing. Junmei Shi for giving me the opportunity to carry out the research for my thesis. His dedication and unfaltering motivation regardless of the situation are values I admire and hope to take with me. I would also like to thank Delphi Technologies and its management for giving the material means to carry out this research.

I would like to express my most sincere gratitude to Prof. Manolis Gavaises for his immense support and guidance in getting my research published and building such outstanding PhD programs. The incredible network of people he has managed to build is an admirable feat.

I am extremely thankful to the European Union for their funding to the Marie Curie ITN HAoS project which provided my financial support. The values of freedom and partnership the EU embodies should never be taken for granted. I would also like to thank ANSYS and Dr. Wolfgang Bauer for providing the research licenses needed to cary out the simulations during my research.

To the Delphi colleagues that became true friends of mine, in the chronological order that we met: Dr. Pablo Aguado Lopez, Kristijan Krapic, Dr. Harun M. Ismail, Kevin Saavedra Castellano, Ramesh Venkatasubramanian, Alex Mieuguem and Kacper Stasiuk, a big thanks for all the shared moments. Thanks as well to the rest of the Delphi colleagues, my peers from the HAoS project for their great collaboration and the rest of the people I met at City.

To my parents, for their support and because with out them I would not be who I am today also thank you.

Finally, I would like to thank Antonia for putting up with me and all the shared time together during this journey.

Declaration

I hereby declare that the content of this dissertation is original and has not been submitted in whole or in part for consideration for any other degree or qualification in this, or any other university. This dissertation is my own work, except where specific reference is made to a joint effort in the text and accordingly acknowledged.

Contents

Chapter 1

Introduction

This Thesis summarises my work as Research Engineer at Delphi Technologies' Technical Centre in Luxembourg as a member of the Computational Fluid Dynamics (CFD) Team. Delphi Technologies is a big stakeholder in the fuel injector field as one of the biggest world Fuel Injection Equipment (FIE) suppliers. During the last 4 years, my research focoused on providing CFD methodology to support the development of Diesel fuel injectors for the first one and a half years and then in GDi injectors for the remaining time.

This Thesis comprises 5 chapters. In Chapter 1, an introduction to the research topic, the research motivations, objectives and a statement of the main contributions is given. Chapter2, presents a critical summary of the theoretical models and numerical approaches used. Chapter 3 "Investigation of cavitation and air entertainment during pilot injection in real size multi-hole diesel nozzles" is based on my first journal publication. It describes a compressible LES numerical framework to simulate fuel injection nozzle flow with needle valve movement. The numerical framework is validated by comparison to available micro-visualisations of a serial production transparent nozzle tip. Chapter 4 "Modelling and prediction of cavitation erosion in GDi injectors operated with E100 fuels" is based on my second journal publication. It reports erosion damage in GDi nozzles when operated with E100 fuel. The numerical framework previously developed is adapted to the prediction of cavitation erosion by use of a barotropic cavitation model. Cavitation erosion indicators are assessed and the physical mechanisms behind the erosion sites are clarified. Finally, Chapter 5 critically discusses the main findings of the research, its practical implications and suggests future lines of work worth exploring.

1.1   Background

Engine technology has advanced due to implementation of common-rail fuel systems for all engine types together with electronic control of the injector's needle, responsible for the flow through the injector. This has allowed not only a substantial increase of the

injection pressure but also to efficient control of very short injection quantity pulses and multiple injections within one combustion cycle. It is accepted that further decrease in emissions can be achieved through the injection of such very small injection quantities during pilot/post injection. Nevertheless, the fuel flow during such injection events leads to large droplets, classical atomisation and nozzle wall wetting, all contributing to increased and insufficient control of emissions.

Internal combustion (IC) engines using fossil fuels provide the 25% of the power produced in the world [1]. Although electrification of passenger cars is accelerating, a majority of the world light-duty fleet is expected to run on fossil fuels even by 2040 (see Figure 1.1). Concerns over global warming and air quality are driving policy makers to take measures to reduce emissions of CO_2 and other pollutants.
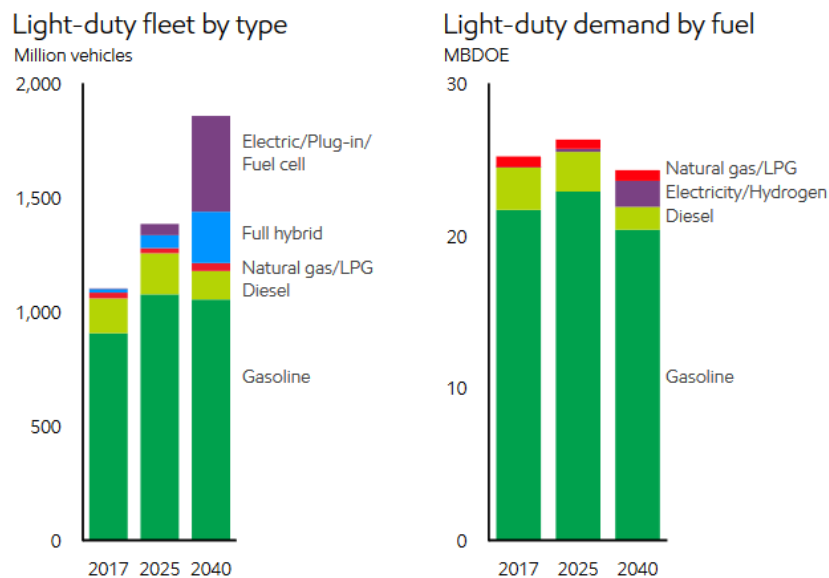
Figure 1.1: Forecast for number of passenger cars (left) and fuel demand in million oil-equivalent barrels per day - MBDOE, (right). Reproduced from [2].

Figure 1.2-left presents how different worldwide automotive regulations have aimed at limiting the automotive fuel consumption; a clear downward trend is visible. These efficiency requirements are being accompanied by limits on other exhausted pollutants such as nitrogen oxides (NOx), particulate matter (PM), carbon monoxide (CO) and unburned hydrocarbons (HC). Fuel consumption and CO_2 reduction in spark ignition engines in particular, is causing a technology shift from traditional port fuel injection (PFi) towards gasoline direct injection (GDi). However GDi engines present a particulate number and mass emission penalty (Figure 1.2-right). Additionally the implementation of the new Real Driving Emission (RDE) cycles to verify the compliance of light duty cars with the Euro 6d emission legislation sees the introduction a limit on particle number emissions of GDi engines [3]. The net reduction of CO_2 emissions is also partially being tackled with

the use of bio-fuel blended mineral fuel. In Europe, E10 (gasoline fuel mixed 10% ethanol) and B7 (Diesel fuel mixed with 7% bio-diesel) are standard. A further increase of the ethanol percentage is under discussion while in Brazil there is even a market demand to develop engines for E100 fuels [1].
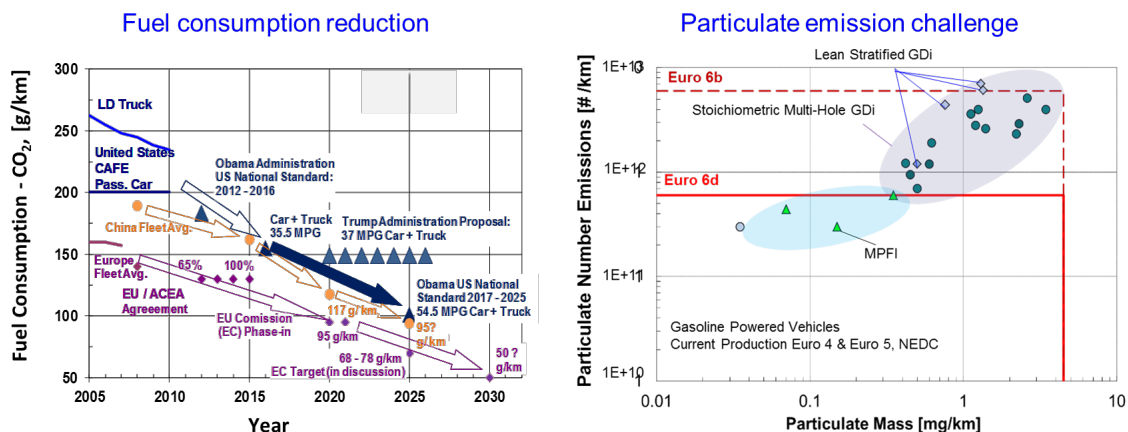
Figure 1.2: Evolution of fuel consumption legislations (left), and particulate emission for different types of spark ignition engines. Source Delphi Technologies internal.

Given this regulation framework, understanding the fuel injection process in passenger cars is of paramount importance since it has direct impact on the spray introduced into the engine and therefore on the pollutant formation by affecting fuel-air mixing and the combustion process. Fuel is injected into the engine by means of a device called injector and it is the injector nozzle flow that controls the spray introduced into the engine. The injector nozzle flow refers to the flow of fuel inside the injector and more specifically through small orifices (usually called injection holes) used to accelerate the fuel and direct it into the combustion chamber. As a consequence, many efforts by the fuel injection community over the last years have been dedicated to study the influence of the injector design and operation on the spray atomisation, mixture formation and combustion, but even if great advances have been made, the progress in the development of fuel injector systems is generally hindered by the difficult experimental access to the injector nozzle due to high injection pressures, small orifice dimensions ($\sim 100\mu m$) and fast operating times.

Technology overview

In the context of Diesel fuel engines, meeting the emission regulations requires resorting to multiple-injection. i.e. dividing the mass of injected fuel into smaller injections. These injection schemes are often operated with fast injector needle opening and closing and with very small separation between injections; in the order of $50\mu s$. They allow for the simultaneous reduction of combustion noise, pollutants and fuel consumption. However,

complex phenomena in the nozzle flow, spray and mixture formation are generated due to the transient operation of the injector, which leads to a highly transient flow and the formation of cavitation (liquid fuel vaporisation) inside the injector nozzle. For instance, by the introduction of a pilot injection it was shown that the ignition delay could be reduced which lead to a slower heat release rate resulting in lower NOx and noise emissions [4]. The use of a pilot injection together with high injection pressures (modern systems employ pressures $> 2000 bar$) significantly reduces both NOx and smoke without increasing fuel consumption [5, 6]. Combining Exhaust Gas Recirculation (EGR) and multiple injections further decreases NOx emissions but worsens soot formation due to increased temperature in rich regions created as a result of oxygen reduction [7].

In order to optimise soot formation, injection timing and dosing is key since injecting into the remains of a pilot injection worsens its emissions [8]. Another factor in soot emission optimization particularly in the early combustion process is the injector needle valve opening slope [9]. As can be seen from Figure 1.3-right and Figure 1.3-left a sharp needle opening makes the spray initially narrower and pushes the combustion away from the nozzle tip (increased lift-off length); this shows the possibility to control the spray, combustion layout in the chamber and therefore soot emissions by controlling the needle speed and lift.
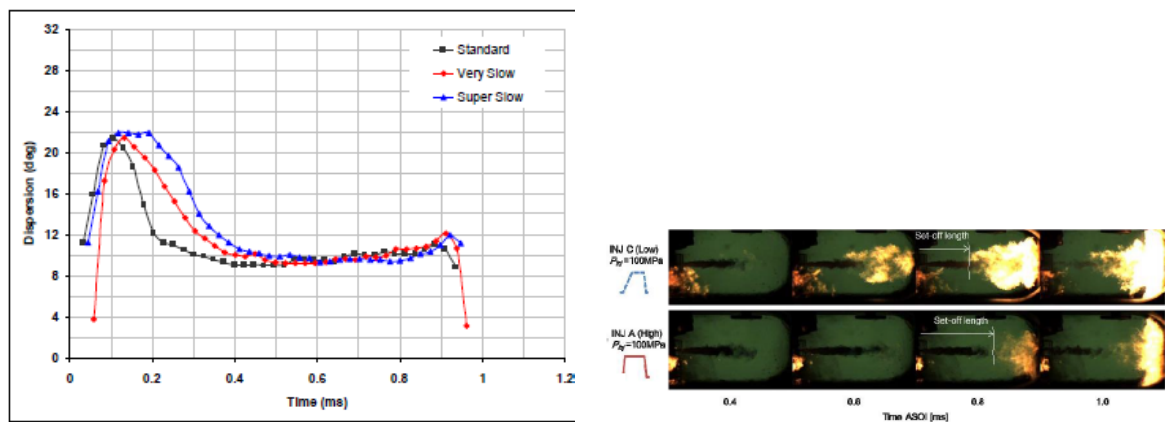
Figure 1.3: Dispersion angle measurements made at Delphi Luxembourg for injectors with different needle opening speeds (left), and effect of needle speed on the combustion process reproduced from [9] (right).

With reference to GDi engines a major challenge for FIE suppliers is the particulate emission. This process is attributed to a complex combination of factors. Two factors of particular relevance to injector manufacturers are the injector tip diffusion flame [10] and spray impingement in the combustion chamber boundaries [11]. The injector tip diffusion flame is caused by residual fuel inside the nozzle tip (sac volume, spray hole, counter bore) and injector tip wetting at the end of the injection. In this process, deposit forms over the injector tip surface that results in absorption of fuel in a layer when the next

injection occurs. This further enhances the diffusion flame. In this way, the deposit layer grows over time and causes injector emission drift over time as depicted in Figure 1.4. One effective approach to reduce this effect is to increase fuel injection pressure (the latest system released by Delphi Technologies employs pressures $> 500 bar$), which enhances the shear surface cleaning effect [12].
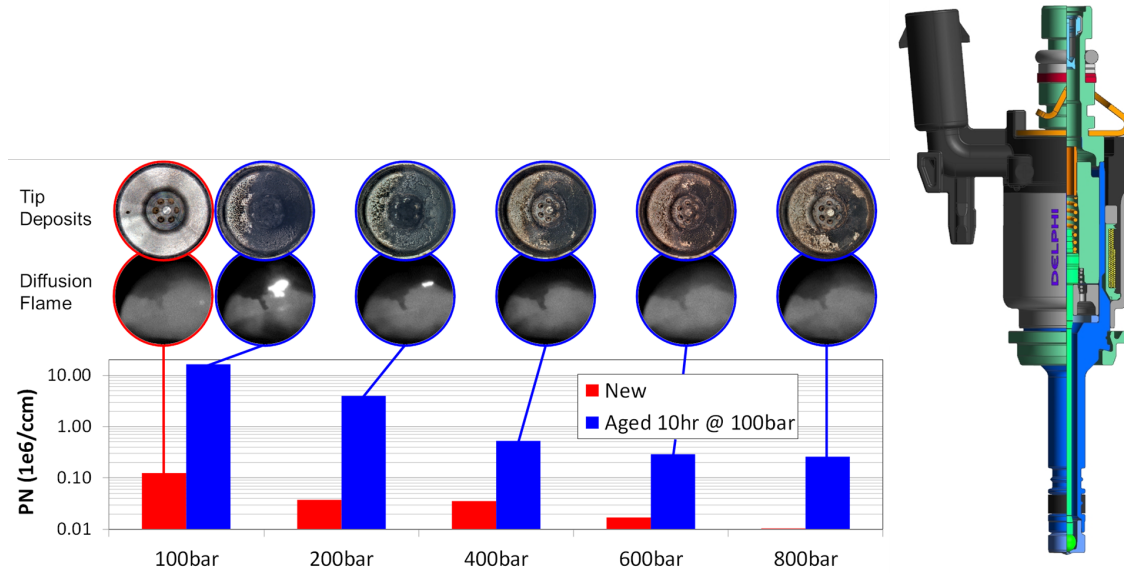
Figure 1.4: A comparison of clean injector performance with pressure and the injector performance after accelerated tip ageing at 100bar for 10hrs on engine. Reproduced from [12].

The wetting of the combustion chamber (piston and cylinder liner) can be usually attributed to over-penetration of certain spray plumes under certain engine operating conditions. Multi-hole GDi injectors are required to provide different spray shapes and characteristics depending on the engine application. In particular, two types of GDi injectors stand out, central mounted and side mounted [13]. Within the engine, the former are placed vertically in the axis of the engine cyclinder, while the latter are placed at an angle. For central mount injectors the spray layout and shape can be symmetric however for side mount injectors the target of the different spray plumes has to be tailored so that no impingement on the different engine components (walls, valves, spark plug, etc.). For the same injector design, the nozzle tip will present holes with different orientations and shapes so that the spray shape, mass distribution and momentum distribution are optimal to the specific engine and provide the right fuel-air mixing. This poses a challenge to build a prototype for a new application that meets the customer requirement based on historical data. Therefore the prototype definition phase can require several iterations.

In summary, light duty vehicles powered by IC engines are likely to still power the majority of the world fleet in the next 20 years. In order to palliate the impact of the pro-

duced emissions, FIE suppliers have to explore the use bio-fuels, higher injection pressures and sophisticated injector control schemes. Therefore there is a clear need to explore, understand and quantify the injector nozzle flow under transient needle conditions given the use of multiple injections in Diesel fuel injectors and end-of-injection phenomena relating to particulate emissions in GDi injectors.

1.2   Literature Overview

Each chapter in this thesis is designed to be self contained and the literature is extensively reviewed in them. However, with the aim of contextualising the research, a non-exhaustive overview on the literature of the physics and modelling of fuel injector nozzle flow and spray now follows.

Nozzle flow and spray physics

The fuel injection process involves a wide range of space and time scales and thermodynamic conditions. Fuel injected at high pressure, is strongly accelerated in the injection holes and then broken inside the combustion chamber where it is atomised into small droplets. The full fuel injection process is shown in Figure 1.5 including the nozzle flow, and spray primary and secondary break-up. The nozzle flow comprises the flow inside the injector and injection hole orifices. The flow is subject to strong acceleration and sudden depressurisation leading to flow separation, compressibility effects, turbulence, the formation of cavitation (vaporisation of the fuel when pressure drops below vapour pressure), and thermal effects. The primary breakup refers to the disintegration into ligaments and droplets of the liquid in the close vicinity of the nozzle exit. Downstream of the the primary breakup, the generated droplets interact with each other and with the ambient air, this double interaction changes significantly the mean droplet diameter by further atomisation of the droplets (secondary breakup) or droplet regroupment and coalescence [14].

The qualitative study of the nozzle flow and cavitation has usually involved visualisation of transparent real or scaled up nozzles. Using high resolution CCD camera visualizations of a transparent nozzle identified geometric cavitation on the upper side of the hole and cavitation strings [16]. The first type of cavitation is related to the hole entrance geometry and can be controlled by means of the hole inlet rounding and conicity while the second due to the low pressure areas inside vortex cores [17]. Strings formed in the sac volume and injection holes have shown correlation with the fluctuation of the spray dispersion angle in scaled up nozzles [18] as well as in real sized nozzles [19]. Moreover cavitation formation has been reported to promote erosion of the nozzle due to transient needle valve operation [20]. Although transparent nozzles provide useful phenomenolo-
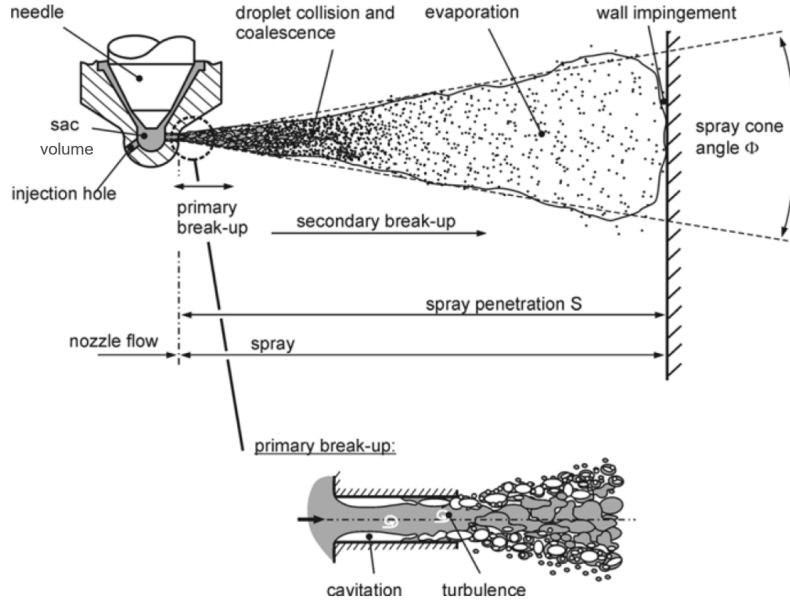
Figure 1.5: Schematic representation of the fuel injection process. Reproduced from [15].

gical information they do not provide quantification of cavitation distribution and do not distinguish between cavitation and air (either contained in the fuel or entrained into the nozzle) [21]. Application of X-ray technology has allowed to quantify average vapour distribution in single-hole nozzles by [22] and to get line of sight mass projections [23] but unfortunately this is only time averaged. Characterisation of the flow velocity has been attempted with micro-PIV in multi-hole injectors [24, 9] but the resolution is still far away from the real scales developed in real sized nozzles. X-ray Phase Contrast Imaging (PCI) is an intricate technique that has been used to measure the velocity of vapour pockets in a simplified single-hole nozzle [25], but the experimental complexity involved makes the technique not applicable at an industrial scale. In brief, nowadays to the best of the author's knowledge no experimental technique exists to fully quantify in space and time the nozzle flow of modern real sized multi-hole injectors.

In the near nozzle region the liquid fuel undergoes atomisation and primary breakup. The non-dimensional parameters that control the process of atomisation are:

- the liquid to gas density ratio $\left(\frac{\rho_{gas}}{\rho_{liq}}\right)$, where ρ_g is the air density and ρ_l the liquid fuel density.

- Reynolds number or ratio of inertial forces to viscous forces, $Re = \frac{\rho_{liq} V_{liq} D}{\mu_{liq}}$, where V_{liq} is the velocity of the injected liquid fuel, and D, the diameter of the injection hole and μ_l the liquid fuel viscosity.

- Weber number or ratio of the inertial forces to the liquid surface tension forces, $We = \frac{\rho_{liq} V_{liq}^2 D}{\sigma}$, where σ is the surface tension between the liquid fuel and the air.

7

Additionally either the density ratio or the Weber number can be substituted by the Ohnesorge number ($Oh = \frac{\sqrt{We}}{Re}$, ratio of the viscous forces to the surface tension forces) [14]. Although optical accessibility is easier than for the nozzle flow and different atomisation regimes have been described based on these numbers (see Figure 1.6), the near nozzle region still presents limited optical access due to the spray being very dense. Therefore how the nozzle design impacts the breakup is still unclear since simultaneous visualisation of the nozzle flow and near nozzle spray in real size multi-hole nozzles remains a challenge. Two techniques worth highlighting have allowed a clearer visualisation of the near nozzle flow, the high resolution X-ray PCI developed at Argonne National Laboratory (ANL) [26, 27], and the application of Transmitted Light Microscopy to the near-nozzle spray visualization [28]. Very recently, with the aid of X-ray PCI simultaneous characterisation of the nozzle flow and near nozzle spray structure in the case of GDi aluminium nozzles has been reported [29]. However the expense of building aluminium nozzles and the reliance on the worldwide unique ANL facility diminish the practical applicability and impact of such a remarkable technique.
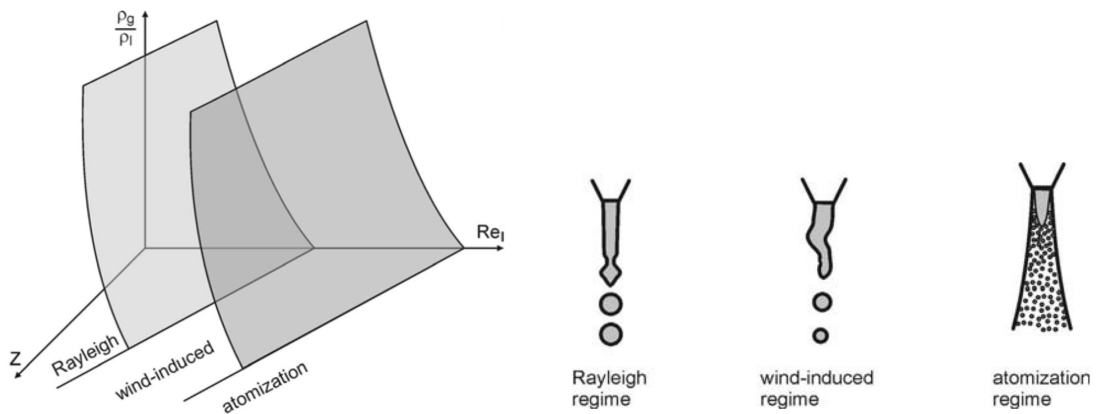
Figure 1.6: Schematic representation of the primary breakup regimes. Reproduced from [15].

Other peculiar effects in Diesel fuel injection include extreme injection pressure, which cause the liquid fuel to reach supercritical conditions and the phase boundaries to become indistinguishable, making the common atomisation knowledge not applicable [30]. While for GDi applications, fuel flash boiling has become frequent due to high in-cylinder temperatures combined with sub-atmospheric in-cylinder pressure causing the fuel to vaporise as soon as the injection starts significantly changing its properties [31].

The complexity of the phenomena and the difficulty in their quantification make the task of designing a nozzle that produces certain far spray characteristics (such as spray penetration and spread angle) challenging.

Modelling of nozzle flow and sprays

Given the experimental complexity and its limitations, resorting to mathematical and numerical modelling together with CFD simulations is an attractive option to shed light and quantify the phenomena present in fuel injection systems. However the diversity of scales and phenomena involved do not make this task any less problematic.

The fuel injector nozzle flow presents important compressibility [32], turbulent [33, 20] and in some cases even thermal effects [34, 35, 36] that must be modelled. Although multiphase models in their most general form treat each phase with its own pressure, velocity and temperature and source terms in the conservation equations determine the momentum mass and energy exchange between the phases [37], nozzle flow simulations found in the literature usually use a homogeneous mixture approach, since the inertia of the gas phases due to cavitation and air expansion is small compared to the bulk liquid therefore mechanical and thermal equilibrium is assumed, leading to a single velocity, pressure and temperature for the mixture [38]. The resulting model is formally identical to the Navier-Stokes equations with an additional transport equation for the mass or volume fraction of the phases; mixing laws determine the local fuel properties based on the phase concentration [39].

Cavitation can be accounted by a source term in the mass or volume fraction transport equation (finite rate mass transfer models) that includes empirical calibration constants [40]. Another option is to consider full thermodynamic equilibrium, the mixture's vapour volume fraction is then obtained from the mixture density and the saturation densities of liquid and vapour at the equilibrium temperature, without the need to solve for any additional transport equation [41]. If thermal effects are small, thermodynamic equilibrium models can be further simplified by not solving the energy equation and considering the density to be exclusively a function of pressure (barotropic models) [42]. Irrespective of the cavitation modelling approach the correct collapse speed of cavitation structures, required for instance to predict erosion phenomena can only be recovered if the model relaxes "fast" the fluid towards equilibrium conditions [33]. In the case of finite rate mass transfer models this is achieved by increasing the mass transfer empirical calibration constants at the expense of imposing restrictive time step integration restrictions [33, 43].

As if matters where not complex enough, resolution of turbulent structures is key in describing vortex cavitation, cavitation shedding and flow unsteadiness. Turbulence is an unsteady flow phenomenon arising at high Reynolds numbers, characterised by the chaotic formation, transport and break down of vortices into smaller vortices until viscous forces are strong enough to dissipate the energy of the flow; a process known as turbulent cascade and first proposed by Kolmogorov [44]. Simulation of all fluid scales, commonly known as Direct Numerical Simulation (DNS) is impractical for industrial high Reynolds number flows, a limitation which will likely remain in the foreseeable future [45]. Under this context

other approaches are available, that try to either partially simulate the turbulent cascade scale resolving simulations (SRS) such as Large Eddy simulation (LES), or model its effect on the mean flow such as the Reynolds Averaged Navier-Stokes (RANS) approach.

LES approaches aim at resolving the large scales that depend on the problem under consideration, while modelling the turbulent scales below the mesh resolution (sub-grid scales) by assuming they have a higher degree of universality. This is usually achieved by filtering of the Navier-Stokes equations using a spatial low-pass filter determined by the cell size (cut-off scale) of the computational domain used. This filtering operation leaves the set of differential equations formally unchanged except for the appearance of extra terms; these represent the sub-grid scale contributions that require modelling [46]; one possibility to judge the cut-off scale is to use the Taylor micro-scale characteristic length (intermediate length scale at which fluid viscosity significantly affects the dynamics of turbulent eddies in the flow [47]) as a guide for the grid resolution required. On the other side of the spectrum, in the URANS approach the equations of fluid motion are averaged; the averaging of the non-linear convective terms leads to the so-called Reynolds stress tensor which also requires modelling [46]. URANS models are considerably less intensive computationally due to less stringent integration time step and mesh resolution requirements than LES, and can be very useful to asses the impact of multiple nozzle design on the flow in a fast way. URANS approaches can predict global flow patterns such as big scale vortices [48], global instabilities such as those caused by transient needle motion [49] and integral values such as mass flow rate and overall phase volumes. However they may fail to predict simple local instabilities such as vortex and cavitation shedding at the inlet corners of a throttle flows; by modifying and reducing the eddy viscosity in cavitating regions the unsteadiness can be reproduced in some situations [50, 51]. Despite this, in [33] URANS models failed to predict incipient cavitation when the pressure difference driving the flow was low. This shows that URANS models are situational and lack universality in the prediction of cavitation. On the other hand, SRS (such as LES and Detached Eddy Simulation - DES) can predict the formation of cavitation in the case of incipient cavitation for both barotropic and finite rate mass transfer models [33]. This type of modelling can also predict areas prone to cavitation erosion in fuel injectors, using both finite rate mass transfer [20] and barotropic models [52]. Unfortunately, the computational cost of scale resolving simulations is still prohibitive for use in daily industrial simulations since they require the use of much finer computational grids and smaller integration time steps than URANS models; see for instance the data discussed in [20, 33] for fuel injection applications.

In terms of modelling the spray, the atomisation process leads to the creation of liquid surface in the form of ligaments and droplets. The simplest approach and widely used in the industry is the so-called Discrete Droplet Method (DDM) Eulerian-Lagrangian

approach; droplets are modelled as a finite number of Lagrangian points called parcels which represent a collection of droplets [53]. These parcels exchange mass, momentum and energy with the Eulerian carrier gas phase. The dynamics of these parcels are resolved using models that account for droplet breakup [54, 55], droplet collision and coalescence [56, 57] and wall impingement [58]. Although the DDM provides a reasonable description of sparsely distributed spherical droplet dynamics far from the vicinity of the nozzle, ligaments in the near nozzle region are not necessarily spherical and the spray can be dense. Additionally, assumptions on the initial parcel velocity, droplet size distribution, spray angle and primary atomisation have to be made which require the tuning of many parameters in order simply to match the macroscopic behaviour of the spray such as the far spray angle and penetration. Therefore DDM can be useful for engine optimisation once a nozzle has been built and spray measurements are available [59, 60], but they do not allow reliable exploration of the nozzle design impact on the results since they ignore the nozzle flow.

One technique aiming at coupling the nozzle flow, near nozzle atomisation and the dilute spray region in a unified framework is the Eulerian-Lagrangian Spray Atomization (ELSA) originally proposed in [61] and its different extensions, for example to LES [62]. It solves in an Eulerian way two extra equations: one corresponding to the liquid volume fraction and the other to the liquid-gas surface density. The model attempts to directly predict magnitudes like the Sauter Mean Diameter (SMD) and liquid dispersion based on relations between surface density and volume. Nevertheless the model makes assumptions regarding the interface behaviour that lead to models with calibration of parameters and difficult generalisation.

Worth mentioning is also the inhomogeneous mixture model [63], referred as well as the multifluid model, in which each of the interpenetrating phases is considered separately with a different set of conservation equations; source terms modelling the the mass, momentum and energy exchange between phases is required to simulate the interaction between them. Based on such models an atomization model for liquid fuel spray simulations has been integrated in AVL FIRE commercial software, using a fully Eulerian formulation, the interacting phases are resolved with the incorporation of a specific number of Eulerian droplet classes, which share the same properties [64].

Other suitable techniques to represent the liquid ligaments and droplets of arbitrary shape in the near nozzle region are based on the advection of a scalar field representing the interface and the most popular are the volume of fluid (VOF) method [65, 66] and the level-set method (LS) [67]. The VOF method has the desirable property of mass conservation and reconstructs the interface sharply from the different phase volume fraction fields with special numerical algorithms. The LS method advects an additional (level-set function), consisting on the signed distance to the interface. This is a smooth function allows for the

interface curvature to be accurately calculated but presents lack of mass conservation. It is worth noticing both methods can be combined into a single Coupled - LSVOF approach [68].

These methods in combination with very fine grids which allow the full resolution of the turbulence spectrum are the most accurate to simulate the atomisation process despite their great computational cost. However the DNS of the primary atomisation is very challenging since there is no clear resolution requirement and grid convergence in the smallest scales is rarely achieved [69, 70], even if some works have attempted to establish practical guidelines on the required resolution [71, 72]. In order alleviate the resolution requirements, one option is to model turbulence with LES and ignore the sub-grid scale contribution of the interface motion and surface tension with the hope that the smallest structures below the grid do not affect the dynamics of the resolved structures. Even if the work of [73, 62] shows that sub-grid scale interface motions can be important to accurately capture the primary atomisation, published LES studies simulating the coupled nozzle flow and near-nozzle spray of Diesel fuel [19] and gasoline [72] injection do exist that derive relevant information on how the nozzle design impacts the spray. Further, alternative promising methods consist on using Eulerian DNS or LES predictions to simulate the nozzle flow and near-nozzle flow while transitioning appropriate ligaments and droplets into Lagrangian parcels [71] or using size and velocity distribution statistics from these predictions as an input for Lagrangian spray models as applied for GDi injection in [74, 75]. Nevertheless, the resolution of the near nozzle spray is still prohibitive for daily industrial simulations and remains a research tool usually applied to just a few case studies.

Given the limitations of both experiments and simulation, differences in the atomisation due to nozzle design in both Diesel fuel injection and GDi have been usually interpreted based on a correlation approach, consisting on applying simulation for the nozzle flow and measurement techniques for the near-nozzle spray characterization and try to find a link between both [76, 77, 78, 17]. Most of this studies however address the problem for static needle lift conditions an needle movement is ignored.

In terms of modelling the dynamic needle movement of the nozzle flow, recent work performed at Delphi Technologies over which this Thesis builds up include the work of [79] who developed a moving needle URANS approach for the simulation of Diesel fuel nozzle flow and was further expanded by [80] who coupled a 1D/3D solvers (AMESim/Fluent) for improved small injection quantity prediction, successfully validated the approach with hydraulic and momentum rig measurement data and also estimated the impact on injector performance of the eccentric needle motion. In terms of comparing URANS and scale-resolving simulations, [49] simulated the start and end on injection for a single hole Diesel fuel nozzle with the cut cell Cartesian method with both URANS and LES. This study concludes that integral values like sac pressure, liquid volume fraction are not greatly

affected but that the local flow morphology is. The same group of authors also investigated the impact of real geometry imperfections on the development of a GDi spray with moving needle [72]. The work of [52] uses the cut cell Cartesian method to simulate a 3-phase flow of a whole 9-hole diesel injector focusing on the vortical development of the flow and the assessment erosion sensitive areas during operation of the injector. After the closing of the needle valve, strong collapse events of vapour structures in the needle seat and the sac hole cause the formation of violent shock waves and they conclude a fully compressible description of the flow is essential to capture such phenomena. Additionally vapour production during certain phases of the injection can only be predicted if the unsteady needle motion is considered in the simulation. Further research on the prediction of cavitation erosion prone locations in Diesel fuel injectors was performed in [20] using a 2-phase dynamic needle approach based on a combination of layering and stretching algorithms to compute the opening phase of two different injector designs managing to correlate the pressure peaks in the domain with areas which suffer from erosion problems.

All aforementioned studies either lack direct validation [52, 72], have only indirect validation [20] or deal with single hole Diesel fuel injection nozzles [49], which lack a complex sac volume flow and present spray characteristics less relevant to industrial applications [76]. Additionally all published studies dealing with cavitation erosion in fuel injectors the author is aware of, pertain to Diesel fuel injectors not GDi.

1.3   Objectives and research methodology

Knowledge on how the injector nozzle geometry, dynamic nozzle flow phenomena (such as the sac volume filling and evacuation, cavitation development, etc.) and the dynamic spray phenomena (such as the near nozzle spray breakup) are linked with the injector tip wetting, the far spray characteristics (such as spray penetration and spread angle) and the injector durability (cavitation erosion) is of great interest to FIE suppliers as it allows to directly the control the nozzle design for improved performance. This knowledge requires full quantification of the injector nozzle flow, but this information is not fully available using experiments in real size multi-hole nozzles while. Quantification of such flows is however possible with CFD and for this purpose there is a need of developing CFD simulation tools able to reliably predict the fuel injector nozzle flow behaviour.

This thesis aims at furthering the understanding of fuel injector nozzle flow under dynamic needle valve conditions by developing a 3-phase (liquid fuel, vapour fuel and air) moving needle LES simulation methodology including the compressibility of the phases under dynamic needle conditions, both for Diesel fuel injection and GDi.

The need of LES stems from the need to correctly predict developing vortical and cavitation features from each injection as opposed to averaged distributions. A 3-phase flow

formulation is considered due to the presence inside the injector of liquid fuel, cavitation (fuel vapour), and the residual air inside the injector. Additionally any further attempt to extend the methodology to the near nozzle spray region would require the inclusion of air. Concerning the compressibility, it is necessary for resolving the complex liquid, cavitation formation and development and air compression/expansion inside the injector.

At first, the developed methodology is validated against existing transparent nozzle flow micro-visualisations of a real size 6-hole Diesel fuel injector nozzle pilot injection. The experimental visualisations show residual air inside the injector sac volume for which the origin is unclear and show evidence of cavitation, however the fuel vapour due to cavitation can not be distinguished from the residual air in the experiments.

Secondly the methodology is adapted and applied for the prediction of erosion prone locations in GDi nozzles operated with E100 fuel. Hardware durability tests performed at Delphi Technologies in prototype nozzles show signs of erosion in the injector tip nozzle after 400 million injection cycles, specifically in the sac centre and spray hole inlet, where cavitation occurrence is expected. Although corrosion due to the use of E100 as working fluid is commonly expected, cavitation is suspected to be a significant enhancing factor of the corrosion damage as a result of the violent collapse of vaporous structures in the condensation process. Hardware durability tests are very resource consuming since they take a long time, in the order of months. A more efficient approach to facilitate the understanding of the physics behind the erosion/corrosion phenomenon is to combine test and simulation analysis, namely use test to record the damage development process and use simulation to verify and understand the test results. Therefore a barotropic model suitable for cavitation erosion prediction is implemented and several cavitation erosion indicators have been evaluated. Nevertheless, the computational expense of LES in this case, limits the applicability of the methodology to a single geometrical sector hole, therefore exploration of whether the URANS modelling approach could return reasonable results for the full nozzle geometry at a significantly reduced computational cost has been performed.

1.4 Present contribution

The novelty of the thesis can be summarised in the following points:

- **Development of an experimentally validated 3-phase (liquid fuel, vapour fuel and air) simulation methodology able to resolve the flow in gasoline (operating with E100) and Diesel fuel injector nozzles including the compressibility of all phases.** Both URANS and LES models have been considered for resolving turbulence while the transient motion of the needle valve has been considered. Simulations have been performed for a pilot injection event, the dwell time

period between successive injection events and the subsequent injection.

- **For the Diesel fuel case, validation has been performed against high speed visualization from a real-scale fully transparent 6-hole nozzle; it is the first time that such a comparison in made.** The simulations have been initialised from a partially-filled with air sac volume, as obtained from the experiments. It has been demonstrated that the simulation methodology compares well against the experiments.

- **For the E100 fuel, validation has been performed against cavitation erosion images obtained from durability tests; it is the first time that such predictions for E100 fuel are presented in the literature.** It has been demonstrated that the simulation methodology predicts well the relevant experimental data.

- **Post-processing of the simulation results has revealed the flow structure during the sac volume filling process with the co-existence of cavitation and surrounding air.** During the closing phase of the needle and the dwell time between successive injection events, the simulations have revealed the process of backflow of air from the combustion chamber into the nozzle and its influence on the next injection cycle. It is the first time that such effects are described with CFD simulations.

During the course of my research, the previous contributions have been summarised in 2 peered reviewed journal publications:

- "Investigation of cavitation and air entrainment during pilot injection in real size multi-hole diesel nozzles" [81].

- "Modelling and prediction of cavitation erosion in GDi injectors operated with E100 fuels" (submitted to FUEL on the 1st of April 2020).

Partial results on the topic of the second paper were presented at the IMECHE Fuel Systems - Engines Conference that took place in London on December 2018:

- "Modelling and Prediction of Cavitation Erosion in Gasoline Direct Injection Injectors Operated with E100 fuel using a Barotropic Equation of State" [82].

During the course of my research I co-authored the following peered review conference publications which are not included in this dissertation:

- "Evidence of vortex driven primary breakup in high pressure fuel injection", ILASS Europe 2017 Valencia [19].

- "High pressure diesel spray development: the effect of nozzle geometry and flow vortex dynamics", ICLASS 2018 Chicago [83].

Awards

I received the "ANSYS Hall of Fame" 2018 award in the Commercial category rewarding the best industry simulation realised with ANSYS products together with Ramesh Venkatasubramanian. I generated the grids, performed the simulation, produced the visualisations and supported Ramesh in creating the winning the animation [84].

Chapter 2

Theoretical model

2.1 Multi-phase modelling

The simulations presented in this Thesis are computed using the commercial CFD code ANSYS Fluent [85]. The flow is solved using a 3-phase (fuel liquid, fuel vapour and air) homogeneous mixture model where all phases share the same velocity, pressure and temperature, this assumes that the inertia of the vapour/air phases is small compared to that of the bulk liquid, and that mechanical and thermal equilibrium can be assumed, leading to a single velocity field for all co-existing phases. For nozzle flow applications, this assumption was tested in [38], by comparing between the multi-fluid approach (where slip between phases is taken into consideration) and the homogeneous in a throttle flow with a Gasoline surrogate. Both models are attributed good predictive capabilities by the authors although the homogeneous mixture approach overestimates by 30% the amount of void (air+fuel vapour) in the experiments. Nevertheless, both approaches underestimated significantly the mass flow rate compared to the experiments (by 8% in the multi-fluid approach and 10% in the homogeneous case) due to real geometry effects in the experiment that were not modelled in the simulation, making it difficult to draw solid conclusions. However, the simulations of [86] for a throttle flow resembling a Diesel injector, found that the slip velocity between the phases was less than 15% of the liquid bulk velocity and only in very localized regions. It is however acknowledged, that the simulation of micro-bubbles of air present in the fuel and their accumulation in vortex cores resulting in vortex strings as in the experiments of [21], might require the inclusion of slip effects between the fuel and the air, however the reduced modelling and computational effort of the homogeneous approach together with no obvious disadvantage, is the reason it is chosen in this work.

The properties appearing in the transport equations are determined by the presence of the component phases in each control volume. The volume fraction of phase i in a cell can be defined as $\alpha_i = \frac{V_i}{V}$, where V_i is the volume of the phase inside the computational cell and V is the volume of the computational cell. The mixture density in each cell is then

given by

$$\rho = \alpha_{liq}\rho_{liq} + \alpha_{vap}\rho_{vap} + \alpha_{air}\rho_{air} \tag{2.1}$$

All other transport properties (viscosity and thermal conductivity) are computed in this manner despite the fact that for homogeneous mixtures it is not clear how one should average each phase's effect, whether based on mass, volume or area (which would require knowledge of inter-facial surface-area density). Although in the case of bubbly flows some theoretical derivations attributed to Einstein do exist [87], viscosity in general depends non linearly on the void fraction and in order to achieve accurate pressure drop calculations the mixture viscosity has to be empirically corrected by fitting coefficients to match experimental data sets [88]. For a review on the available correlations for the transport properties the interested reader is referred to [39]. Obviously, the volume constraint $\alpha_{liq} + \alpha_{vap} + \alpha_{air} = 1$, in each cell must be respected.

The solved model consists on the following equations (reproduced from [85]):

- Mass conservation equations of vapour and air phases

$$\frac{\partial \alpha_{vap}\rho_{vap}}{\partial t} + \nabla \cdot (\alpha_{vap}\rho_{vap}\mathbf{v}) = R_e - R_c \tag{2.2}$$

$$\frac{\partial \alpha_{air}\rho_{air}}{\partial t} + \nabla \cdot (\alpha_{air}\rho_{air}\mathbf{v}) = 0 \tag{2.3}$$

where the source terms R_e and R_c represent the mass transfer between liquid and vapour phase due to cavitation. When the barotropic homogeneous equilibrium model is employed Eq. 2.2 is not solved.

- Continuity equation of the mixture:

$$\frac{\partial \rho}{\partial t} + \nabla \cdot (\rho \mathbf{v}) = 0 \tag{2.4}$$

- Momentum equation of the mixture:

$$\frac{\partial \rho \mathbf{v}}{\partial t} + \nabla \cdot (\rho \mathbf{v}\mathbf{v}) = -\nabla(p) + \nabla \cdot \sigma \tag{2.5}$$

where the effective viscous stress tensor is defined as $\sigma = \tau + \tau_t = \mu(\nabla\mathbf{v} + (\nabla\mathbf{v})^T) + \tau_t$, μ is the viscosity of the mixture and τ_t are the turbulent stresses defined according to the turbulence model being used.

- Energy equation of the mixture:

$$\frac{\partial \rho E}{\partial t} + \nabla \cdot (\mathbf{v}(\rho E + p)) = \nabla \cdot (k_{eff}\nabla T + \sigma \cdot \mathbf{v}) \tag{2.6}$$

where the energy is treated as a mass averaged value $\rho E = \sum \alpha_i \rho_i E_i$ and the total energy for each phase E_i is based on the local thermodynamic conditions of that phase. $k_{eff} = \sum \alpha_i (k_i + k_t)$ is the shared effective thermal conductivity and k_t is the turbulent

thermal conductivity, defined according to the turbulence model being used (note that the previous summations are extended to all phases). In the current Thesis the energy equation is only solved in the calculations involving Diesel fuel. For GDi simulations either constant fluid properties or the barotropic cavitation model are employed effectively decoupling the energy equation or making it redundant, respectively.

The handling of moving and or defroming grids requires special treatment with regards to space and flux conservations as descirbed in [85].

2.1.1 Cavitation model

Although cavitation has been widely studied by many authors in the Diesel fuel injection as reviewed in Chapters 1, 3 and 4, cavitation is also relevant in GDi injection; from some studies it is difficult to draw the difference between cavitation from flash-boiling [89, 90]. The studies with cold fuel in [91] and [92] show that cavitation is present in GDi injectors. In the context of a fuel injector manufacturer, many of the assessments used to judge the injector performance (mass flow rate characterisation, cold spray shape characterisation, spray targeting, etc.) are realised in cold conditions for which flashing is not expected; cavitation modelling is therefore essential in GDi injectors in this context.

Finite rate mass transfer model based on the Rayleigh Plesset equation

The source terms appearing in equation 2.2 represent mass transfer between fuel liquid and vapour phases due to cavitation bubble expansion and collapse respectively. When finite rate mass transfer models are utilised in this Thesis, calculation of these values is based on the Rayleigh-Plesset equation for bubble expansion and collapse [93], and its magnitude based on the Zwart-Gerber-Belamri cavitation model [40] which reads as:

$$
\begin{aligned}
R_e &= F_{vap} \frac{3\alpha_{nuc}(1-\alpha_{vap})\rho_{vap}}{R} \sqrt{\frac{2}{3} \frac{max((p_{vap}-p),0)}{\rho_{liq}}} \\
R_c &= F_{cond} \frac{3\alpha_v \rho_{vap}}{R} \sqrt{\frac{2}{3} \frac{max((p-p_{vap}),0)}{\rho_{liq}}}
\end{aligned}
\tag{2.7}
$$

F_{vap} and F_{cond} are empirical calibration coefficients, α_{nuc} is the volume fraction associated with the nuclei contained in the liquid and R the assumed bubble radius. Other formulations for this source terms exist such as the Schner-Sauer [94], they have been shown to be equivalent if the coefficients are chosen appropriately [95]. According to [40], values of $R = 10^{-6}m$, $\alpha_{nuc} = 5 \cdot 10^{-4}$,$F_{vap} = 50$, $F_{cond} = 0.01$ give reasonable results in a wide range of flows. However, the mass transfer magnitude for these values could be insufficient creating areas of unrealistic liquid tension and not reproducing correctly the Rayleigh-Plesset bubble collapse, a possible solution is to increase the empirical calibration coefficients several orders of magnitude to approximate the model to a Homogeneous

19

Equilibrium Model (HEM) [33].

Barotropic cavitation model

Barotropic models, are a subset of thermodynamic equilibrium models, which ignore thermal effects and exclusively focus on the variations of density with pressure. They are particularly suited for the analysis of cavitation erosion prone locations due to their simplicity and capability to accurately reproduce the collapse of cavitation structures [33]. Linear barotropic cavitation models have been previously employed in the literature for Diesel fuel nozzle flow simulations (see for example [52]), however as remarked by [96] non-linear models are preferred due to their capability of reproducing the right mixture compressibility (speed of sound) and having continuous speed of sound, this facilitates the solution convergence in iterative pressure based solvers. In this work a polynomial barotropic cavitation model is similar to [97] is proposed; whereas [97] uses a 5th order polynomial in this work a 3rd order polynomial is considered since it enables to impose 4 constraints (continuity of density and speed of sound), at the two extremes of the pressure interval in which mass transfer takes place.

Indeed, given the vapour saturation pressure of the working fluid p_{sat} and a pressure interval δp over which the mass transfer takes place we can define:

$$
\begin{aligned}
p_{satL} &= p_{sat} + \frac{\delta p}{2} \\
p_{satV} &= p_{sat} - \frac{\delta p}{2}
\end{aligned}
\tag{2.8}
$$

The fuel is in liquid state when $p > p_{satL}$ and follows a Tait equation of state (EOS):

$$
\rho(p) = \rho_{satL}(\frac{p - p_{satL}}{B'} + 1)^{1/n}, \; p > p_{satL}
\tag{2.9}
$$

The constants n and B' are dependent on the fluid and are fitted from the density measurements and can be fitted to a high degree of accuracy such as in Chapter 4. The model assumes a polytropic evolution for the vapour phase (when $p < p_{satV}$) and a third order polynomial for the mixture (when $p_{satV} < p < p_{satL}$). The full barotropic cavitation model proposed reads as:

$$
\rho_{fuel}(p) = \begin{cases} \rho_{satL}(\frac{p - p_{satL}}{B'} + 1)^{1/n} & p > p_{satL} \\ Ap^3 + Bp^2 + Cp + D & p_{satV} < p < p_{satL} \\ (\frac{p}{C_{vap}})^{1/\gamma_{vap}} & p < p_{satV} \end{cases}
\tag{2.10}
$$

In the case of the of the vapour phase, the value of γ_{vap}, C_{vap} can be determined by knowledge of the vapour phase density ρ_{satV} at pressure p_{satV}. Early trials have shown that using low values of ρ_{satV} lead to difficulty in obtaining a stable solution. Constants

A, B, C, D for the mixture are unknowns and are calculated so that both density and speed of sound ($c^2_{fuel} = \frac{\partial p}{\partial \rho_{fuel}}$) are piece-wise continuous by solving the following linear system of equations:

$$
\begin{aligned}
Ap^3_{satL} + Bp^2_{satL:} + Cp_{satL} + D &= \rho_{satL} \\
Ap^3_{satV} + Bp^2_{satV} + Cp_{satV} + D &= \rho_{satV} \\
3Ap^2_{satL} + 2Bp_{satL} + C &= 1/c^2_{satL} \\
3Ap^2_{satV} + 2Bp_{satV} + C &= 1/c^2_{satV}
\end{aligned}
\tag{2.11}
$$

This model presents a small pressure difference δp over which the mass transfer takes place and regulates the compressibility of the mixture (minimum speed of sound in the mixture), see Figure 2.1.

Figure 2.1: Role of δp in the regulation of the compressibility of the mixture. The model was fitted for N-heptane from the data available in [98].

For homogeneous mixtures according to [93, 99], the minimum speed of sound should be between two extremes; the frozen speed of sound (also known in the literature as Woods or Wallis speed of sound) which is derived assuming no mass transfer:

$$
\frac{1}{\rho c^2_{frozen}} = \frac{1 - \alpha_V}{\rho_L c^2_L} + \frac{\alpha_V}{\rho_V c^2_V}
\tag{2.12}
$$

and the equilibrium speed of sound (derived assuming infinitely fast heat exchange and mass transfer):

$$
\frac{1}{\rho c^2_{frozen}} = \frac{1 - \alpha_V}{\rho_L c^2_L} + \frac{\alpha_V}{\rho_L c^2_L} + \frac{(1 - \alpha_V)\rho_L c_{p,L} T}{(\rho_V L)^2}
\tag{2.13}
$$

where $c_{p,L}$ is the liquid specific heat capacity and L is the latent heat of evaporation, both at a reference temperature T. The value of δp is chosen to respect these bounds.

A typical test case to asses the performance of cavitation models is the Rayleigh collapse. The incompressible Rayleigh collapse solution, describes the compression of a vapour bubble embedded in high pressure liquid [99]. The bubble collapse velocity is given

21

by:

$$\frac{dR}{dt} = -\sqrt{\frac{2}{3}\frac{p - p_{sat}}{\rho_L}((\frac{R_0}{R}))^3 - 1)} \qquad (2.14)$$

where p is the far field pressure, p_{satv} is the vapour saturation pressure, ρ the liquid density, R_0 is the initial bubble radius and R is the bubble radius at time t. Integration of the previous equation yields an approximate collapse time of $\tau \approx 0.915 R_0 \sqrt{\frac{\rho_L}{p-p_{sat}}}$ [99]. Verifications of the capability of both finite rate mass transfer and barotropic cavitation models to reproduce the Rayleigh collapse of a vapour bubble exist in the literature, see for example [33] where the authors compare a barotropic homogeneous equilibrium model to the ZGB cavitation model with different values of the mass transfer coefficients. However this verification for the polynomial barotropic model introduced in this Thesis is not available in the literature to the best of the authors knowledge.

The implementation of the polynomial barotropic cavitation model into the CFD code is verified for a 2D axis symmetric case, starting from a 20 μm radius bubble at p_{satV}, embedded in 100 bar liquid; the used fluid properties are those of Ethanol detailed in Chapter 4. The results of the simulation for the radius of the collapsing bubble against time is shown in Figure 2.2 (top). The difference found in the collapse time between the theoretical solution and the barotropic model is 2.6%; in the process a maximum pressure of 15403 bar at the bubble centre is achieved, see Figure 2.2 (middle and bottom).

2.1.2   Fluid properties

In the next paragraphs the fuel properties that have been employed in this Thesis are reviewed.

Diesel Fuel properties

Diesel injectors are operated with high injection pressures and fast needle transients involving low needle lifts. These factors cause high injection speed velocities and important transient heating effects making an incompressible approach not justified [35, 20]. Moreover the Diesel fuel fluid properties are significantly impacted by the high injection pressures employed. At injection pressures of 2000bar, Diesel fuel viscosity can increase by a factor of 7 and density by 10% [100]. In this work the Diesel fuel liquid phase is modelled as a compressible liquid based on measurements made for the calibration oil Normafluid ISO4113. This is the usual fuel for testing and calibrating diesel fuel injection systems in both laboratories and at an industrial level. All diesel properties that follow are taken from [101, 102], where details of the measurement methodology, range of validity, method for fitting the coefficients and their values can be found. These properties were implemented into ANSYS Fluent following the available User-Defined-Real-Gas-Model (UDRGM)
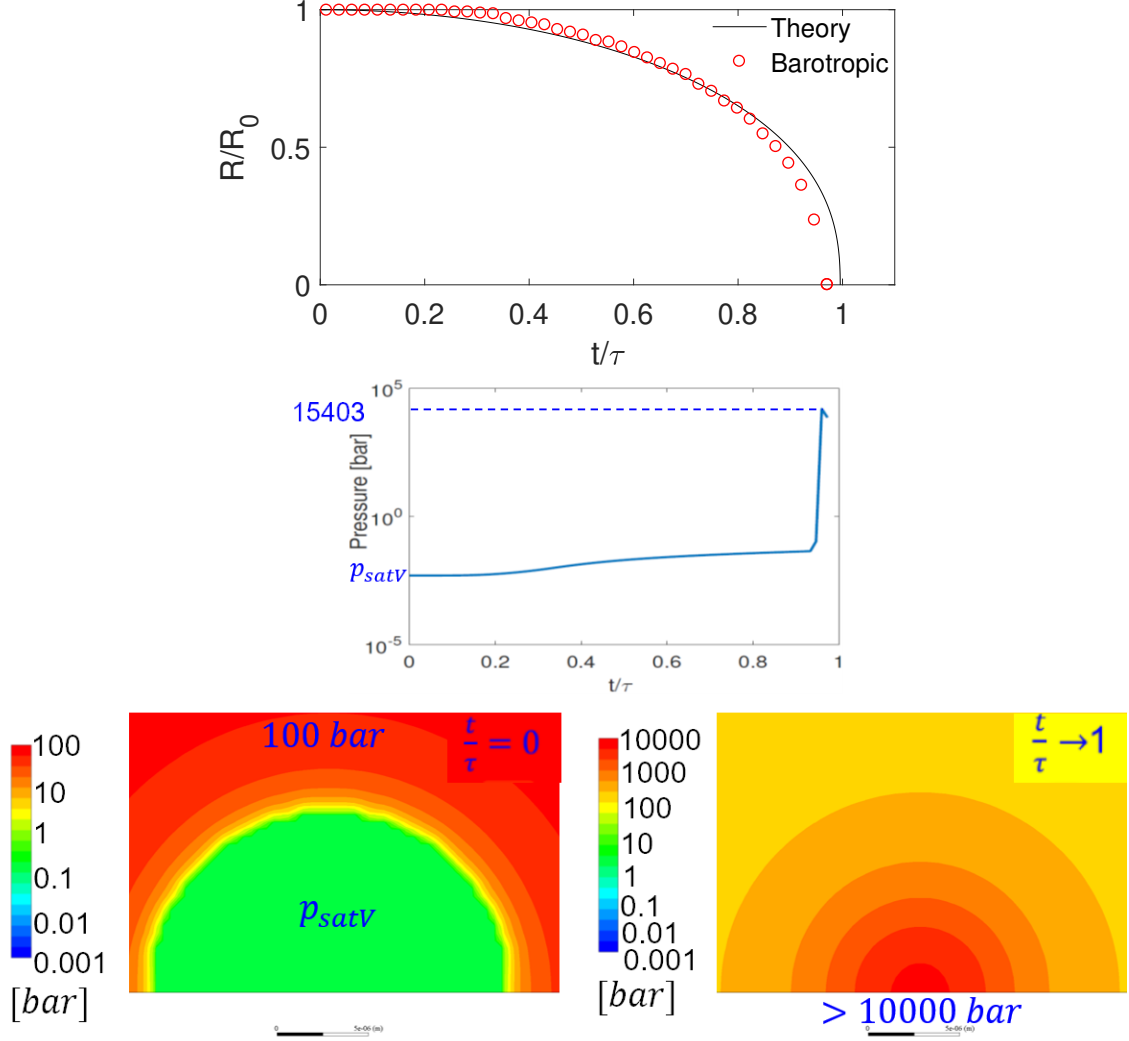
Figure 2.2: Radius of collapsing bubble vs time (top), pressure at the bubble centre vs time (middle) and pressure contours (bottom)

functionality in order to follow the modelling approach of [35].

The liquid density (ρ_{liq}) follows a Tait-like equation:

$$\frac{1}{\rho_{liq}(p,T)} = \frac{1}{\rho_{atm}} + aln(\frac{P+b}{P_{atm}+b}) \tag{2.15}$$

with $a = a_0 + a_1 T + a_2 T^2$ and $b = b_0 + b_1 T + b_2 T^2$. The density at atmospheric pressure is given by $\rho_{atm} = \rho_0 + \rho_1 T + \rho_2 T^2 + \rho_3 T^3$. The range of validity of the previous expression is for temperatures in the range 283.15 to 403.15K and pressures up to 2000bar [101]. The behaviour of density for different pressures and temperatures can be observed in Chapter 3 - Figure 2 (left).

The the liquid viscosity (μ_{liq}) measurements where made in the range 293.15 to 353.15K for pressures at up to 2000bar. Figure Chapter 3 - Figure 2 (right) shows the variation of viscosity as a function of pressure along isotherms. It is worth observing the

viscosity exponential increase with pressure. These data were fitted into the following expression:

$$\mu_{liq} = A e^{\left(\frac{B}{T-C} + D \ln\left(\frac{P+E}{P_{atm}+E}\right)\right)} \tag{2.16}$$

E100 properties

Ethanol's fluid properties are presented in detail in Chapter 4 and follow the experiments of [103].

N-heptane and Stoddard properties

N-heptane has a similar density to gasoline blends but its composition is unique and is therefore used at Delphi Technologies for GDi injector hydraulic characterisation (assessing flow rate and injector control). All the fuel properties of N-heptane are available from the NIST database [98]. Stoddard is a petroleum-derived liquid used as a common organic solvent and is less flammable than N-heptane and is therefore used at Delphi Technologies for GDi spray characterisation (assessing spray shape and penetration) [104].

Fluid	Density [kg/m^3]	Viscosity [$Pa\,s$]	Vapour saturation pressure [Pa]
N-heptane	683.82	0.000411	4722
Stoddard	783	0.00098	200

Table 2.1: Fluid properties of different gasoline like fluids used in this thesis.

Air properties

Air compressibility effects can be important during the sac volume filling event of an injection. This was observed in [105, 106, 107] where the compression of air bubbles inside the sac volume at the start of the injection is evident. Therefore the air density is modelled as an ideal gas with equation of state $p = \rho R T$ when the energy equation is solved or otherwise via an isentropic equation of state ($\rho_{air} = (\frac{p}{C_{air}})^{1/\gamma_{air}}$), where the constant is calculated at ambient conditions (1 bar and 293 K) and $\gamma_{air} = 1.4$.

2.1.3 Solution methods

For the numerical integration of Equations 2.1 to 2.6, two big families of algorithms exist: the pressure based solvers and the density based solvers [85]. Originally, pressure-based approaches were developed for incompressible flows, while the density-based approaches were used used for high Mach compressible flows. However, both methods have been extended to be able to solve a wide range of operating conditions beyond their original application. Regardless of the method the velocity vector is obtained from the momentum equations. In the pressure-based approach, the pressure field is determined by solving a

pressure or pressure correction equation which is obtained by combining continuity and momentum equations. Conversely, the density-based solvers, use the continuity equation to determine the density field and the pressure field is determined from the equation of state.

In fuel injection applications both compressible LES pressure based solutions [20] and density based solutions [52] can be found in the literature. In density based solvers however the integration time step is limited by the speed of wave propagation in the liquid (speed of sound), which can result in small integration time steps and long computational times. For example, [20] used an integration time step of $5 \times 10^{-9} s$ for a grid resolution of $\sim 7 \mu m$, an injection pressure of $p_{inj} \sim 1800 bar$ and a Reynolds number of $Re \sim \frac{\rho V D}{\mu} \sim 30000$. On the other hand [52] used an integration time step of $1.75 \times 10^{-9} s$ and 0.74×10^{-9} for grid resolutions of $\sim 10 \mu m$ and $\sim 5 \mu m$, respectively an injection pressure of $p_{inj} \sim 1500 bar$ and $Re \sim 22000$. This illustrates the different time step requirements between both approaches.

In this Thesis, the flow equations are solved with a pressure based algorithm since it is the only one available in ANSYS Fluent for multi-phase flows. Depending on the cavitation model two different pressure based approaches have been used. For the ZGB model, the segregated SIMPLEC algorithm [108] was used and the governing equations are solved sequentially. For the barotropic model, the chosen solution algorithm was the coupled solver [109], where the momentum and continuity equations are solved in a coupled manner. Trials have shown that for the barotropic model the coupled approach is far superior in terms of convergence rate than the segregated approach. In terms of discretization scheme for the momentum, the second order upwind [110] is used in the URANS cases. In the LES cases a second order a bounded central differencing scheme based on the normalised variable diagram (NVD) approach together with the convection boundedness criterion (CBC) was used [111]. This scheme has small numerical dissipation and sufficient numerical stability for industrial LES simulations [45]. For all simulations a body-force-weighted scheme is employed for pressure interpolation[85] and a second order upwind scheme in the case of the ZGB cavitation model or a first order upwind scheme in the case of the Barotropic cavitation model for the density interpolation [110]. This choice is again motivated to ease the solver convergence when using the barotropic model. Finally the calculation of gradients is done using the Least Squares Cell-Based method.

Even if the used solver is pressure-based and therefore the simulation stability is not limited by the acoustic wave propagation time scale, the temporal resolution for LES requires minimum diffusion for the advection of the turbulent eddies. Therefore the time integration time step is chosen for the LES simulations so that $CFL = \frac{v \Delta t}{\Delta x} \sim 1$ in the spray hole, where v is the local velocity magnitude, Δt is the time integration time step and Δx is the local mesh resolution. For the URANS cases where only the integral simulation

values are of interest the time step can be increased.

2.2   Turbulence modelling

Unsteady Reynolds Averaged Navier Stokes (URANS) model

The objective when using URANS turbulence model is to obtain an averaged affordable solution to the Navier-Stokes equations. To obtain the averaged equations all the variables are decomposed into their mean and fluctuating parts. For instance for the velocity vector one can write:

$$u_i = \bar{u}_i + u_i' \tag{2.17}$$

where $\bar{u}_i$ is the mean field and u_i' is the fluctuating part of the velocity vector components ($i = 1, 2, 3$). By proceeding in an analogous way with the rest of scalar quantities and substituting into the flow equations one arrives to the averaged equations in tensor form:

$$\frac{\partial \bar{\rho}}{\partial t} + \frac{\partial}{\partial x_i}(\bar{\rho} u_i) = 0 \tag{2.18}$$

$$\frac{\partial \bar{\rho} \bar{u}_i}{\partial t} + \frac{\partial}{\partial x_j}(\bar{\rho} \bar{u}_i \bar{u}_j) = -\frac{\partial p}{\partial x_i} + \frac{\partial}{\partial x_j}(\mu(\frac{\partial \bar{u}_i}{\partial x_j} + \frac{\partial \bar{u}_j}{\partial x_i})) + \frac{\partial}{\partial x_j}(-\bar{\rho u_i' u_j'}) \tag{2.19}$$

For compressible flows, it is convenient to introduce instead the the density-weighted (Favre) filtering operator $\tilde{\phi} = \frac{\overline{\rho \phi}}{\bar{\rho}}$, for each variable ϕ. These equations known as the Unsteady Reynolds-Averaged Navier-Stokes (URANS) equations have the same form as the original Navier-Stokes but additional terms appear: $\frac{\partial}{\partial x_j}(-\bar{\rho u_i' u_j'})$, which represent the effect of turbulence. Theses terms are known as the Reynolds stresses and have to be modelled to close the problem. The usual way to model these stresses is through the Boussinesq hypothesis which states that they are proportional to the mean strain rate tensor:

$$-\bar{\rho u_i' u_j'} = \mu_t(\frac{\partial \bar{u}_i}{\partial x_j} + \frac{\partial \bar{u}_j}{\partial x_i}) - \frac{2}{3}\rho k \delta_{ij} \tag{2.20}$$

and where $k = \frac{1}{2}\bar{u_i' u_i'}$ is the turbulent kinetic energy. Only the turbulent kinetic energy k and the turbulent viscosity μ_t remain unknown. In the case of the $k - \epsilon$ and $k - \omega$ models, two additional transport equations (for k and either the turbulence dissipation rate, ϵ, or the specific dissipation rate, ω) are solved, and μ_t is computed from k and of ϵ or ω. In this work the $k - \omega\ SST$ model is employed [112], a blend between the standard $k - \varepsilon$ and $k - \omega$, which solves two extra equations for modelled turbulent kinetic energy

transport (k) and specific dissipation rate (ω), offering better accuracy in the vicinity of walls than the $k - \varepsilon$ and less sensitivity to the boundary conditions than the $k - \omega$ model.

The use of the $k - \omega$ SST model is standard and widely used for simulating the flow in Diesel fuel (see for example [76, 78]) and GDi injectors (see for example [48, 77, 113]). It has also been employed for cavitation erosion prediction in Diesel fuel injectors [114], high pressure fuel pumps [115] and hydrofoils [116]; part of the novelty of this work is the application of such model to predict cavitation erosion in GDi injectors, see Chapter 4.

Large Eddy Simulation

The objective when using LES is to simulate the big inertial scales that are dependent of the problem while modelling the smaller universal scales. This is achieved by filtering of the Navier-Stokes equations using a spatial low-pass filter determined by the cell size of the computational domain used. For any variable ϕ, the filtering procedure consists in applying the following mathematical operator:

$$\bar{\phi} = \frac{1}{V} \int_V \phi(\mathbf{x}', t) d\mathbf{x}' \tag{2.21}$$

at each computational cell, for all the $\mathbf{x}'$ contained in the volume V of the cell. This operator leaves the flow equations mostly unchanged, but transforms the equations into equations for the filtered magnitudes. During this operation terms in the equations appear representing the sub-grid scale contributions to the equations of motions and have to be modelled. For instance applying this filter operator to the equation 2.5 yields:

$$\frac{\partial \bar{\rho} \tilde{\mathbf{v}}}{\partial t} + \nabla \cdot (\bar{\rho} \tilde{\mathbf{v}} \tilde{\mathbf{v}}) = -\nabla(\bar{p}) + \nabla \cdot \bar{\sigma} - \nabla \cdot (\bar{\rho} \widetilde{\mathbf{v}\mathbf{v}} - \bar{\rho} \tilde{\mathbf{v}} \tilde{\mathbf{v}}) \tag{2.22}$$

where for compressible flows, it is convenient to introduce the density-weighted (Favre) filtering operator $\tilde{\phi} = \frac{\overline{\rho \phi}}{\bar{\rho}}$. The last term in equations 2.22:

$$\tau = (\bar{\rho} \widetilde{\mathbf{v}\mathbf{v}} - \bar{\rho} \tilde{\mathbf{v}} \tilde{\mathbf{v}}) \tag{2.23}$$

is the sub-grid scale momentum stress tensor and energy flux vector resulting from the filtering process which are unknown and must be modelled.

In the case of the sub-grid scale momentum stress tensor, the deviatoric part may be modelled following the Boussinesq hypothesis [46]:

$$\tau_{ij} - \frac{1}{3}\tau_{kk}\delta_{ij} = -2\mu_t(\tilde{S}_{ij} - \frac{1}{3}\tilde{S}_{kk}\delta_{ij}) \tag{2.24}$$

where $\tilde{\mathbf{S}} = \frac{1}{2}(\nabla(\tilde{\mathbf{v}}) + \nabla(\tilde{\mathbf{v}})^T)$ is the resolved strain rate tensor and Einstein's notation has been used. The isotropic part of the tensor can be added to the filtered pressure or neglected [117]. The closure of the model requires calculating a suitable sub-grid turbulent

viscosity μ_t. For such purpose, the Wall-Adapting Local Eddy-Viscosity (WALE) [118] model is chosen:

$$\mu_t = \bar{\rho}L_s^2 \frac{(S_{ij}^d S_{ij}^d)^{3/2}}{(\tilde{S}_{ij}\tilde{S}_{ij})^{5/2} + (S_{ij}^d S_{ij}^d)^{5/4}} \tag{2.25}$$

where $L_s = min(\kappa d, C_w V^{1/3})$ is the mixing length for the sub-grid scales. $\kappa = 0.4$ is the von Karman constant, d is the normal distance to the nearest wall and $C_w = 0.325$ is the WALE constant following the values published in [45].

Finally S_{ij}^d is defined in the WALE model as:

$$S_{ij}^d = \frac{1}{2}\left(\frac{\partial \tilde{v}_i}{\partial x_j}^2 + \frac{\partial \tilde{v}_j}{\partial x_i}^2\right) - \frac{1}{3}\delta_{ij}\left(\frac{\partial \tilde{v}_k}{\partial x_k}^2\right) \tag{2.26}$$

This model is capable of correctly reproducing the correct turbulence wall behaviour ($\mu_t \sim o(y^3)$) and becomes 0 at $y = 0$, being y the distance to the wall. Another advantage is it returns a zero turbulent viscosity for laminar shear flows which allows the correct treatment of laminar zones in the domain [85], necessary for modelling the start of injection when flow velocities are low.

For the energy equation apart from the terms related to viscous dissipation which are modelled based on the above description of the sub-grid stress tensor, the compressible sub-grid enthalpy flux term is modelled using a sub-grid scale turbulent Prandtl number following the gradient hypothesis [85]:

$$q = \frac{\mu_t c_p}{Pr_{SGS}}\nabla T \tag{2.27}$$

where μ_t is the sub-grid viscosity, Pr_{SGS} is a sub-grid Prandtl number equal to 0.85 and c_p the specific heat at constant pressure. It is worth mentioning that no sub-grid scale contributions stemming from the multiphase model are accounted for.

The LES model settings in this Thesis is adapted from the basis of the previous successful studies on Diesel fuel injection primary breakup [17, 19, 119, 83]. In order to choose the appropriate filter/mesh size for the LES, the Taylor micro-scales (λ_g) is used. This is an intermediate length scale at which fluid viscosity significantly affects the dynamics of turbulent eddies in the flow [47]. An estimation of the Reynolds number inside of the injection hole of diameter D yields a value of $Re = \frac{(\rho v D)}{\mu}$, where ρ, μ are respectively the liquid density and the viscosity and v is the characteristic injection velocity, conservatively estimated for a given injection pressure difference Δp with the Bernouilli relationship $v = \sqrt{\frac{2\Delta p}{\rho}}$. For a given Re this corresponds to a $\lambda_g \sim \sqrt{\frac{10D}{Re}}$ [46]. Consequently, a fully hexahedral mesh is created in each case with a resolution of λ_g in the regions of interest, namely the seat, sac and spray hole, and is progressively coarsened in the counter bore and discharge volume regions. Since resolution of the smallest eddies in the wall vicinity

requires the non-dimensional wall distance based on the friction velocity to be of the order of 1 ($y^+ \sim 1$) [46], additional refinement is applied in the wall region so as to achieve an average y^+ is about 1 in the region of interest and a maximum wall y^+ of about 10 around the sharp edge of the spray hole entrance.

Chapter 3

Investigation of cavitation and air entrainment during pilot injection in real size multi-hole diesel nozzles

This Chapter is based on my first publication [81] and brings together both experiments and simulations of the complex three-phase (liquid fuel, vapour fuel and air) flow developing inside a real sized multi-hole diesel injector nozzle during the pilot injection period. High speed micro visualisations of a transparent nozzle tip are used to record cavitation and air flow while LES is used to assist in the interpretation of the underlying physics. The literature on this topic has been examined and critically correlated to the topic under investigation. It was found that the numerical framework is capable of reproducing the observed phenomena. For the first time, simulations of compressing air bubbles during the start of the injection in the injector sac are presented. This shows the importance of modelling air compressibility. Additionally, other phenomena such as void stemming from the sac entry, needle seat and hole entry induced cavitation are captured through a cavitation model based on the Rayleigh-Plesset equation. Finally, air entrainment into the injector's sac volume from the ambient is observed and predicted at the end of injection. An extra unpublished critical review section is provided discussing the choice of model for the boundary movement.

I curated the transparent nozzle images for the investigation, developed and implemented the thermo-hydraulic model for Diesel fuel into the CFD software, developed the moving mesh methodology, generated the grids, performed the simulation, analysed the results, produced the visualisations and wrote the original draft of the manuscript.

3.1 Introduction

New European Real Driving Emission (RDE) driving cycle legislations require significant research efforts to develop emission compliant and efficient passenger car engines [120]. In this context, the so-called digital injection schemes, used to split the fuel injection into multiple small injections with close separation among them, are widely applied in modern diesel engines in order to obtain simultaneous reductions in noise and emissions without compromising engine performance and fuel consumption [5, 4].Although the nozzle flow for static needle lift conditions has been extensively investigated (see selectively [121, 122, 32, 123]), not much work is available for the flow development during the dynamic operation of the injector, which plays a key influence on emissions [9, 124].

The digital injection schemes are often operated with fast injector needle opening and closing and with very small separation between injections; with typical dwell time of the order of $50\mu s$. This results in highly transient flow and formation of cavitation inside the injection nozzle. In addition, modern diesel engines are operated under high injection pressure ($> 2500bar$) and utilise injectors with small injection hole diameters ($90 - 120\mu m$); these conditions pose significant difficulties in measuring and/or optically visualising the processes occurring in both the injector nozzle and within the high temperature combustion chamber. The majority of transparent real-size nozzle investigations featuring simplified single-hole geometries that generally confirm the presence of geometric-induced cavitation [125, 126, 127]. The work of [16, 128, 129], and the relevant early modelling work [130] were the first to substitute one of the holes of a production nozzle with a quartz window of identical geometric characteristics and was an experimental breakthrough that provided valuable information on flow and cavitation structures inside such micro-channels under realistic operating conditions; further studies were reported in [131]. A step forward was realised in [24], where a 3-hole, real-size, fully transparent nozzle allowed for unobstructed optical access inside the sac volume. Vortex cavitation is dramatically enhanced by vapour or air already present inside the nozzle volume [21]. Moreover, [132] showed that the structure of a vortex core is significantly affected by entrained vapour bubbles. Similarly, [133] demonstrated possible fragmentation of the vortex core so as to increase the vorticity at the core centre. Finally, the strong interaction observed between vortex properties and bubble dynamics[134], the coupling of radial and axial growth of bubbles trapped in vortices [135] and the interaction between shear (or normal strain) flow and bubble volume change [136] form a tremendously complex flow field inside an injector nozzle, where dynamic changes in the behaviour of vortices and vapour bubbles strongly affect the emerging fuel spray. Highly transient flow phenomena caused by the fast needle response times, give rise to formation of vortical structures and therefore, to string cavitation [137]. Transient effects have also been correlated to increased probability

of surface erosion damage, which is attributed to both, geometric and string cavitation [138]. Cavitation in simplified nozzle replicas has been visualized even at pressures as high as 2000bar, as shown in [139, 140]. Remarkably, in very recent studies, sonoluminescence from cavitation collapse observed in a simplified nozzle replica has been observed for the first time[141] and a neutron imaging technique has been developed overcoming the disadvantages of using materials transparent to visible light[142]. All aforementioned studies report data from one or just a few injection events. The group of the authors has reported in [105, 106, 107]] for the first time averaged images of cavitation developing in a real-size 6-hole transparent tip nozzle for single and pilot-main split injections up to 400bar. Data from these investigations are further reported here and utilized for validation of the newly developed model. Only the very recent work of [143] has extended the range of operating conditions (injection pressures up to 1000bar and back pressures up to 30bar) and geometrical features studied (hydro erosively ground inlet orifice) for long injections. These studies provide qualitative data on cavitation and air-entrainment inside the fuel injector during the opening and closing of the injector's needle valve. A drawback of the images is that one cannot distinguish between cavitation and air, as they both appear as an indistinguishable black shadow in the obtained images.

Given the limited quantitative information around the flow structure inside diesel injectors, fuel injection equipment manufacturers require robust predictive Computational Fluid Dynamics (CFD) tools, in order to understand the physical mechanisms taking place during injection. From a physical viewpoint, modelling of such flow conditions requires the fluid compressibility [20], mass transfer (cavitation, flash boiling, evaporation etc.) and heat transfer [34, 35, 36] to be taken into account, which increase the complexity as well as the computational cost of the simulations. Additionally, the fluid dynamics processes occur at high Reynolds number and therefore accounting for the effect of turbulence structures and vortex dynamics, is key in explaining how the injected fuel spray is formed [17, 19, 119, 83]; this can only be resolved using very fine computational grids and scale resolving simulations, such as Large Eddy Simulation (LES).

Recent LES including dynamic needle movement for the in-nozzle flow includes the work of Battistoni et al. [49] who simulated the start and end of injection for a single hole nozzle using the cut cell cartesian method for modelling the boundary movement and a homogeneous relaxation model for cavitation phenomena. The work concludes that URANS predictions for the residual liquid back flow occur without fragmentation, while in LES liquid breaks up generating complex three dimensional structures. The URANS approach predicted at the end of the injection an annular void region stemming from the needle seat, which then re-condenses as the pressure is recovered. This was not observed in LES, where regions of low pressure are produced even in areas detached from the needle seat. The predicted near spray region was also different as no ligaments

were formed in URANS; instead diffusion disperses the liquid in the surrounding air even if integral values like sac pressure and liquid volume fraction were not greatly affected. Ligament formation and gas ingestion into the nozzle at the end of injection are predicted, as observed experimentally in Phase Contrast X-ray images (for additional Phase Contrast X-ray studies see for example [124, 27]). The start-of-injection simulation shows how gas is ejected first, and liquid fuel starts being injected with a delay. The main result of these analyses is that if the sac volume is initially filled with gas, the liquid exit is delayed several tens of μs after the start of needle movement, which is in good agreement with the experimental evidence. This delay is of the order of $100\mu s$, and it is compatible with the duration of the first slow rising part of the needle movement. Orley et al. [52] used the cut cell cartesian method to simulate with implicit LES, a barotropic homogeneous equilibrium model for cavitation and a fully compressible 3-phase flow model a complete 9-hole diesel injector. The focus of the work was on the vortical development of the flow and the assessment of erosion sensitive areas during the operation of the injector. After the injector closing, strong collapse events of vapor structures in the needle seat and the sac hole cause the formation of violent shock waves. The authors highlighted that a fully compressible description of the flow is essential to capture such phenomena. It was also concluded that despite steady needle simulations capturing the main flow features reasonably well, vapor creation during the closing phase of the needle valve requires information on the previously developed flow; thus, reliable prediction of erosion-sensitive areas due to collapse events during and after the closing of the needle can only be predicted accurately by including the unsteady needle motion. Finally, the work of Koukouvinis et al. [20] used a 2-phase dynamic needle approach based on a combination of layering and stretching algorithms together with a Rayleigh-Plesset based cavitation model with increased mass transfer, to compute the opening phase of two different injector designs; the findings have correlated the pressure peaks in the domain with areas that suffer from erosion. Whichever the chosen modelling approach may have been, previous studies have lacked validation [52], had indirect validation [20] or were not of direct relevance to modern applications [49], since a single hole nozzle lacks the complex sac recirculation flow present in modern diesel injectors.

On the broader perspective, reduction of exhaust gas and in the same time noise emissions from engines, relies on multiple injection strategies, such as digital rate shaping (DRS) [144, 145, 146, 147], which allow the use of a variety of options for pilot, main, and post-(main) injection events in order to provide a degree of control over the timing and phasing of the ignition delay and heat release events, as reported in [148]. Recent investigations from the group of the authors suggest that when the dwell-period is shortened, there is significant reduction in soot while exhaust-out NOx is controlled by EGR. Similarly, the CN-soot trade-off can be decoupled by reducing pilot-main dwell time, adding a

greater number of pilots and increasing rail pressure without compromising fuel consumption [149]. The use of such complex strategies described relies on the ability of the fuel injection equipment to accurately meter extremely small quantities of fuel per event (which may be of the order of $1mg$ of fuel being injected in a period of less than $0.25ms$) over the engine lifetime [147]. During these short metering events the injector will not reach full lift and will be operating within the transient part of the rate curve. To meet these demands, it is extremely important to avoid the accumulation of excessive carbonaceous deposits on, and within the fuel injector. Nozzle hole deposits can reduce the effective flow area of the fuel or cause it to be mis-directed. These effects give rise to poorer atomisation and mixing, excessive spray penetration, and increased risk of fuel impacting on the combustion chamber surfaces, with the potential to adversely affect emissions. The impact of deposit formation within nozzle holes and their effect on engine performance are well summarised in [150], concluding that residual fuel remaining within the injector nozzle's sac and holes are thought to be instrumental in the process [124]. With increasing number of pilot injections with short dwell time, the residual fuel in the nozzle sac after needle closure can be critical for the HC and soot emissions. However, experimentation of the detailed flow dynamics inside the injector at such conditions is practically impossible; currently there is no study reporting quantitative data on the flow development during the injection events for such processes. The experimental data reported in [105, 106, 107, 143] clearly indicate that the flow and cavitation development inside the injector is different in every injection cycle, and differ significantly from the experimentally derived time-averaged field, as shown in [106]. An alternative to shed light to those processes, is the use of computational fluid dynamics. The current work, to the best of the authors knowledge, presents for the first time application of a 3-phase LES to the flow in a diesel injector for a pilot injection event, including cavitation and compressibility of all phases; simulations have utilised the optically measured needle valve movement from fully transparent real size 6-hole nozzle tips [105, 106, 107], as reported by the group of the authors. Moreover, the high-speed shadowgraph images from those studies serve as validation of the developed model; these include the location/timing of cavitation initiation, its further extent and eventual collapse and the air entering into the injection holes and sac volume of the nozzle tip.

The need to employ LES derives from the necessity to predict the flow formation of individual injection cycles, as opposed to cycle-averaged flow distribution. The complexity of the flow is not only linked to the formation of cavitation, but also to the residual air present inside the injector; this has been considered in the present work by initialising the residual air distribution inside the injector's sac volume and injection holes from the images recorded for individual injection events. Moreover, inclusion of compressibility effects for all phases is deemed as necessary for resolving the complex liquid, cavitation formation and development and air compression/expansion inside the injector, as it is

34

shown in the reported results.

The present paper is structured in the following way: first an overview on the experimental results is given for a diesel pilot injection visualization of a transparent nozzle tip. Then the numerical methodology employed is described in detail, followed by the comparison of the CFD results with the transparent nozzle visualisations for which good agreement is obtained and interpretation of the observed phenomena is provided.

3.2   Experimentally observed multiphase phenomena

As already mentioned, the 3-phase simulation methodology has been validated against high speed visualisations of a transparent Delphi Technologies Diesel 6-hole nozzle tip manufactured by City, University of London. The metallic injector nozzle tip was substituted with a transparent acrylic tip. The design is a standard serial production geometry, i.e not just a multi-hole nozzle, but a fully operational, serial production type. The detailed results and findings of that experimental campaign as well as the setup details were reported in [105, 106, 107] and will not be repeated here. The 6-hole transparent tip has holes with no taper (zero conicity) and a nominal diameter (D) of $160\mu m$. The electrical pulse activation width for a pilot injection was $0.5ms$. High speed cameras recorded the events at a frame rate of $30000fps$. An example of a pilot injection for a rail pressure of 300bar into atmospheric conditions can be found in Figure 3.1. Given the image acquisition rate, the pilot injection including all major events after closing lasts for 24 frames. As discussed in [106, 107] air trapped in the sac after the end of the injection aggregates forming bubbles in the sac and occupying part of the hole. Prior to $233.33\mu s$ after the electrical trigger, no change is observed and therefore images are not shown. Then the trapped bubble shows slight expansion due to the initial volume created by the needle as it starts lifting ($300\mu s$ after the trigger) and subsequent compression ($400\mu s$ after the trigger) highlighting the need to model air compressibility. This is followed by void coming from the seat passage and its advection into the hole ($500\mu s$ after the trigger). Then, due to flow acceleration at the hole entrance, void structures are seen in the hole during the opening phase ($600\mu s$ after the trigger). During the needle closing phase, vapour increases substantially in the hole and void coming from the seat reappears ($633.33\mu s$ after trigger). At the end of the injection, the sac gets full with bubbles and the spray greatly weakens ($733.33\mu s$ after the trigger), followed by what seems to be air suction ($766.66\mu s$ after the trigger). Finally, a bubbly mixture is observed floating in the sac as well as an oscillatory movement of the air in the hole ($1000\mu s$ after the trigger). An important input for nozzle flow moving needle simulations is the needle lift profile which was extracted from the images [105, 106, 107].

Figure 3.1: Experimental results. Time sequence of a pilot injection transparent nozzle tip visualisation.

3.3 Modelling approach

The simulations are computed using the commercial CFD code ANSYS Fluent [85]. The nozzle flow is solved using a homogeneous, three-phase mixture model (liquid fuel, vapour fuel and air) where all phases share the same velocity, pressure and temperature. The code is supplemented with user defined functions (UDFs) for implementation of the thermo-hydraulic properties of diesel and the needle movement.

3.3.1 Multiphase model

The properties appearing in the transport equations are determined by the presence of the component phases in each control volume. Defining α_{liq}, α_{vap}, α_{air} as the volume fraction of liquid fuel, air and vapour fuel in a cell, respectively, the density in each cell is given by: $\rho = \alpha_{liq}\rho_{liq} + \alpha_{vap}\rho_{vap} + \alpha_{air}\rho_{air}$.

All other transport properties (viscosity and thermal conductivity) are computed in this manner despite the fact that for homogeneous mixtures it is not clear how one should

average each phase's effect, whether based on mass, volume or area (which would require knowledge of interfacial surface-area density). Although in the case of bubbly flows some theoretical derivations attributed to Einstein do exist [87], viscosity in general depends non linearly on the void fraction and in order to achieve accurate pressure drop calculations the mixture viscosity has to be empirically corrected by fitting coefficients to match experimental data sets [88]. For a review on the available correlations for the transport properties the interested reader is referred to [39]. Obviously, the volume constraint $\alpha_{liq} + \alpha_{air} + \alpha_{vap} = 1$, in each cell must be respected. The solved equations consist of the continuity, momentum and energy of the mixture, and the mass conservation equations for the vapor and the air:

$$\frac{\partial \rho}{\partial t} + \nabla \cdot (\rho \boldsymbol{v}) = 0 \tag{3.1}$$

$$\frac{\partial \rho \boldsymbol{v}}{\partial t} + \nabla \cdot (\rho \boldsymbol{v} \boldsymbol{v}) = -\nabla p + \nabla \cdot \sigma \tag{3.2}$$

$$\frac{\partial \rho E}{\partial t} + \nabla \cdot (\boldsymbol{v}(\rho E + p)) = \nabla \cdot (k_{eff} \nabla T) + \sigma \cdot \boldsymbol{v} \tag{3.3}$$

$$\frac{\partial \alpha_{vap} \rho_{vap}}{\partial t} + \nabla \cdot (\alpha_{vap} \rho_{vap} \boldsymbol{v}) = R_e - R_c \tag{3.4}$$

$$\frac{\partial \alpha_{air} \rho_{air}}{\partial t} + \nabla \cdot (\alpha_{air} \rho_{air} \boldsymbol{v}) = 0 \tag{3.5}$$

The source terms R_e and R_c represent the mass transfer between liquid and vapour phase due to cavitation. The effective viscous stress tensor is defined as $\sigma = \tau + \tau_t = \mu(\nabla v + (\nabla v)^T) + \tau_t$,

where μ is the viscosity of the mixture and τ_t are the turbulent stresses defined per the turbulence model being used. The energy is computed as the mass average for each phase and the internal energy of each phase is based on the local thermodynamic conditions of that phase [35].

The source terms appearing in the vapour volume fraction transport equation ($R_e - R_c$) represent the mass transfer between fuel liquid and vapour phases due to cavitation bubble expansion and collapse respectively. The calculation of these values is based on the Rayleigh-Plesset equation describing bubble expansion and collapse [93], and its magnitude is based on the Zwart-Gerber-Belamri cavitation model [40] which reads as:

$$R_e = F_{vap} \frac{(3\alpha_{nuc}(1 - \alpha_{vap})\rho_{vap})}{R_b} \sqrt{\frac{2}{3} \frac{max((p_{vap} - p), 0)}{\rho_{liq}}} \tag{3.6}$$

$$R_c = F_{cond}\frac{(3\alpha_{vap}\rho_{vap})}{R_b}\sqrt{\frac{2}{3}\frac{max((p - p_{vap}), 0)}{\rho_{liq}}} \qquad (3.7)$$

F_{vap} and F_{cond} are empirical calibration coefficients, α_{nuc} is the volume fraction associated with the nuclei contained in the liquid and R_b the assumed bubble radius and p_{vap} is the vapour pressure. According to [40], values of $R_b = 10^{-6}m$, $\alpha_{nuc} = 5 \times 10^{-4}$, $F_{vap} = 50$, $F_{cond} = 0.01$ give reasonable results in a wide range of flows. Nevertheless, as discussed in [33] the mass transfer magnitude for these values could be insufficient creating areas of unrealistic liquid tension and not reproducing correctly the Rayleigh-Plesset bubble collapse, the suggested solution is to increase the empirical calibration coefficients several orders of magnitude to approximate the model to a Homogeneous Equilibrium Model (HEM). However, within this work the original coefficients published in[40]were used.

3.3.2 Turbulence model

The target when using LES is to capture the large scales that are dependent of the physical domain simulated while modelling the sub-grid turbulent scales. This is achieved by filtering of the Navier-Stokes equations using a spatial low-pass filter determined by the cell size of the computational domain used. This operation leaves the flow equations unchanged, but transforms the equations into equations for the filtered magnitudes [46]. During this operation terms in the equations appear representing the sub grid scale contributions to the equations of motions and have to be modelled. The closure of the model requires calculating a suitable sub grid turbulent dissipation (viscosity) μ_t. For such purpose, the Wall-Adapting Local Eddy-Viscosity (WALE) model is chosen [118]. This model is capable of correctly reproducing the correct turbulence wall behaviour ($\mu_t \sim o(y^3)$) and becomes 0 at $y = 0$, being y the normal distance to the wall. Another advantage is that it returns a zero turbulent viscosity for laminar shear flows which allows the correct treatment of laminar zones in the domain, this is necessary for modelling the start of injection when flow velocities are low.

3.3.3 Fluid properties

High injection pressures and low lifts cause high injection velocities and transient heating effects making an incompressible approach unjustifiable [34, 35, 20]. Even if for the transparent nozzle tip testing conditions the pressure is lower than engine conditions, the diesel liquid phase is modelled as a compressible liquid based on the measurements made for the calibration oil Normafluid ISO4113. This is the usual fuel for testing and calibrating diesel fuel injection systems in both laboratories and at an industrial level. All diesel properties that follow are taken from [101, 102], where details of the measurement methodology, range of validity, method for fitting the coefficients and their values can be

found (see Figure 3.2 for plots of the density and viscosity values for different pressures and temperatures). These properties were implemented into ANSYS Fluent following the available User-Defined-Real-Gas-Model (UDRGM) functionality as in [35]. As mentioned in the experimental results section, air compressibility effects are observed during the sac filling event and therefore the air density is modelled as an ideal gas with equation of state $p = \rho RT$.
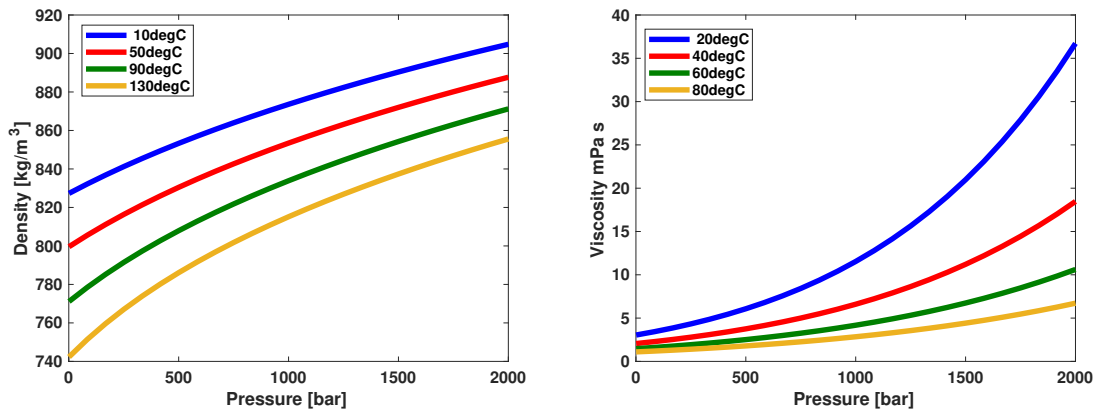

Figure 3.2: Diesel fuel properties implemented. Density (left) and viscosity (right) diesel fuel properties used.

3.3.4 Moving mesh methodology. Mesh generation and boundary conditions.

Modelling the dynamic movement of the needle is inherently difficult. At low lifts the cells in the seat are squeezed into very small gaps deteriorating their quality, which can have an impact on the robustness and accuracy of the simulation. Moreover, the contact between walls is not trivial to model since the continuity of the mesh is broken. Recent advances have been reported in [148] where the immersed boundary method has allowed simulations to be performed even at zero needle lift; however, this method has not been adopted here and as a compromise, the closed needle is modelled using the seat surface as a wall when the needle lift is below $1\mu m$.

The approach followed is based on an interpolation approach between two topologically identical meshes (key-grids) with the same number of cells and was already employed by the authors in [82]. The initial mesh has a $1\mu m$ lift and the high lift mesh is based on the maximum lift reached for the pilot injection $36\mu m$. Based on the node position of this two meshes any intermediate lift is achieved by linear interpolation between the node position of the two key-grids. Another difficulty associated is the loss of resolution in the seat passage as the needle reaches high lifts, this requires interpolating the results into another pair of key-grids such as in [35]. For the pilot injection cases considered

39

here, this was not needed due to the relatively low lift attained ($36\mu m$). Moreover, in order to save computational resources, just a 60° sector is model (one hole) based on the nominal (target) geometry. Figure 3.3 (left) shows the computational domain, consisting of different surfaces; the hole, housing, needle, seat inlet and side surfaces. Additionally, a 2mm long conical discharge volume is added in order to move away the outlet boundary condition from the areas of interest. The computational mesh used for the LES flow simulation is a fully hexahedral mesh.

The LES settings are adapted from the basis of the previous successful studies on diesel [17, 19, 119, 83] and gasoline [82, 12] direct injection and primary breakup simulations. In order to choose the appropriate filter/mesh size for the LES, the Taylor micro-scales (λ_g) have been estimated. This length scale is the intermediate length scale at which fluid viscosity significantly affects the dynamics of turbulent eddies in the flow [47]. For the flow inside the transparent tip, the Reynolds number based on the nozzle hole diameter, outlet pressure and inlet temperature can be estimated to be $Re = \frac{(\rho V D)}{\mu} \sim 13000$. The Taylor micro-scales can then be approximated by [46]: $\lambda_g = \sqrt{\frac{10D}{Re}} = 4.4\mu m$. However, in order to resolve the smallest eddies close to the wall, the non-dimensional wall distance based on the friction velocity has to be of the order of 1 ($y^+ \sim 1$) [46]. Therefore, additional refinement close to the walls is needed. An estimate of this value based on the turbulent boundary layer theory yields a cell wall distance of $\sim 0.2\mu m$. In order to reach a value of $\sim 5\mu m$ in the bulk flow without increasing excessively the number of cells, a cell growth ratio of 1.1 was applied in the wall. Under these constraints, a $\sim 5M$ element mesh was produced, with a volume change between neighbouring cells below 3, minimum cell angle of 27° and $3D$ determinant (normalized triple product of the vectors starting from each cell node) above 0.6 for both key-grids. Special care was taken to refine the needle seat area in the stream-wise direction in order not to exceed for low lifts aspect ratios of 100 in the direction of the bulk flow. Figure 3.3 (right) depicts the two meshes needed for the interpolation method, and a front view of the mesh showing the additional refinement in the seat area. A pressure boundary conditions was applied to the inlet of the domain. The pressure at the injector entrance in the high-pressure pipe was taken from the experimentally recorded values for every individual injection event. During the opening phase, pressure decreases at the injector entrance due to the increasing flow through it. At the end of the injection an over pressure is observed due to the water hammer effect after needle closing. The pressure at the entrance of the injector was provided in [105]. A temperature of $300K$ was chosen for the flow entering the domain and an air mass fraction value of 2×10^{-5} was imposed to take into account the possible dissolved air since it is a typical value for fuel or water exposed to ambient pressure [38]. The non-slip boundary conditions was applied to the non-moving wall (housing, hole, discharge volume wall, and, seat surface below $0.1\mu m$) as well as to the needle according to the motion profile resulting

from the needle lift profile extracted from the images [105]. Periodic boundary condition have been applied to the side surfaces. Finally, a fixed pressure outlet was applied to the outlet surfaces, with pressure $1bar$ and $300K$ and air volume fraction prescribed as 1 in the case of back-flow.
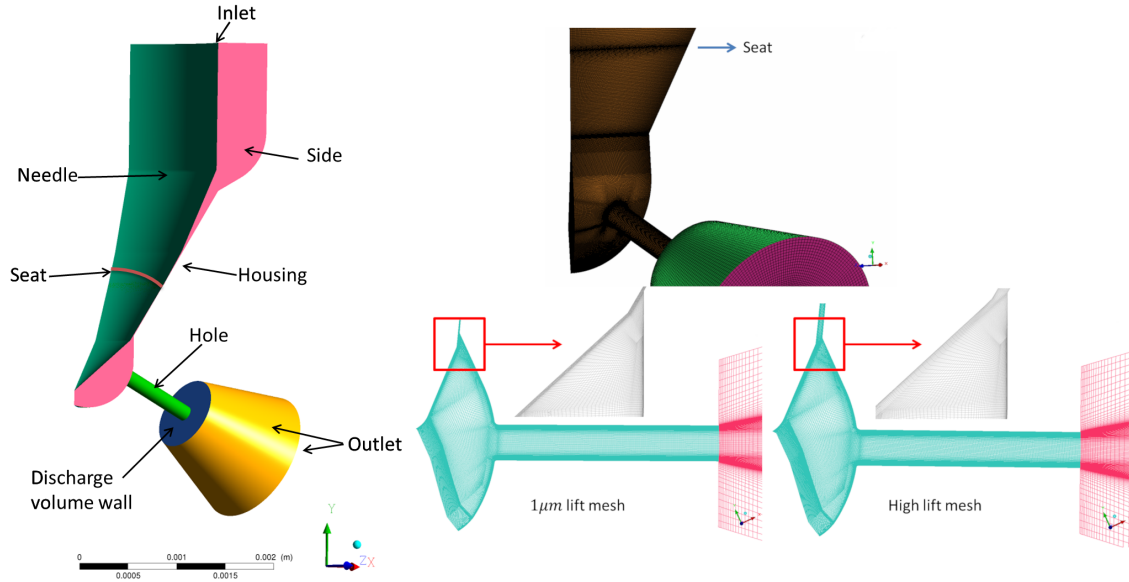

Figure 3.3: Geometrical model and mesh. Domain simulated and boundary conditions (left). Mesh showing seat refinement (right-top) and mesh cross section for both high and low lift meshes (right-bottom).

The experimental images of the transparent nozzle show trapped air bubbles inside the injector before the start of injection. The mechanism behind the appearance of this bubble is not straight forward to derive from the experimental images. Regardless, the LES nozzle flow simulation is initialised in qualitatively similar way; half of the hole is filled with air and an air spherical bubble is included in the sac (see Figure 3.4).

The computational domain above the seat surface is initialised at the pressure corresponding to that instant. Below the needle seat, the simulation is initialised at a pressure of $1bar$. All the domain is initialised at a temperature of $300K$ and with zero velocity. For the closing phase the movement of the needle is stopped when it reaches $1\mu m$ however the seat surface is not switched from interior to wall until the needle lift profile reaches $0.1\mu m$.

The solver used is segregated and pressure-based. The pressure-velocity coupling is achieved using the SIMPLEC algorithm [108]. Density is interpolated using a second order upwind scheme [110] while for the momentum a bounded central differencing scheme based on the normalized variable diagram (NVD) approach together with the convection boundedness criterion (CBC) [111] was used. The bounded central differencing scheme is a composite NVD-scheme that consists of a pure central differencing, a blended scheme of
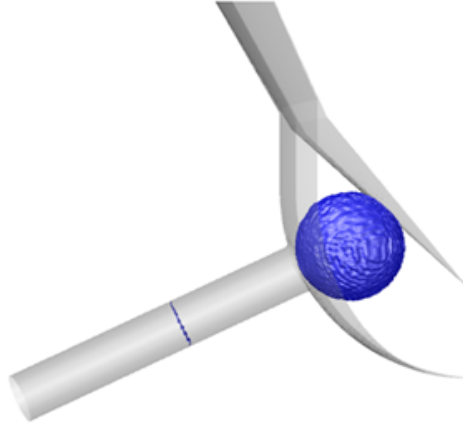
Figure 3.4: Initial simulation instant. Iso-surface of 0.5 liquid volume fraction and a mid-plane for the initial instant.

the central differencing and the second-order upwind scheme, and the first-order upwind scheme. The first-order scheme is used only when the CBC is violated. This scheme has small numerical dissipation and sufficient numerical stability for industrial LES simulations [45]. Among the volume fraction interpolation schemes available in ANSYS Fluent when using the mixture model, the quadratic upstream interpolation for convective kinetics (QUICK) scheme is selected in order to reduce the smearing of sharp volume fraction gradients and capture high density ratios [151]. Pressure interpolation follows the body force weighted scheme [85] and the temperature the first order upwind scheme. Finally the calculation of gradients was done using the Least Squares Cell-Based method.

The used solver is pressure-based and therefore the simulation stability is not limited by the acoustic wave propagation time scale. However, temporal resolution for LES requires minimum diffusion for the advection of the turbulent eddies. Therefore, an adaptive time step method is employed to ensure the advection CFL number stays below 1 throughout the computational domain.

3.3.5 LES mesh quality evaluation

The instantaneous fields of the LES quality metric of by Celik et al.[152] and y^+ for a representative moment at the highest lift ($t = 0.608ms$) are shown in Figure 3.5. Based on the y^+ the boundary layer resolution can be assessed; this value only exceeded 1 in areas above the seat and gradually transitions to values well under 1 ensuring a good wall shear resolution for the small eddies near the walls. Following [46] a good LES requires the modelled turbulent kinetic energy (k_{sgs}) to be less than 20 of the total turbulent energy ($k_{sgs}+k_{res}$), that is $\frac{k_{sgs}}{k_{sgs}+k_{res}} < 0.2$. However, as mentioned in [49] knowledge of k_{res} in the case of a moving needle injection can only be gained by repeating the simulation multiple

times which could not be afforded computationally. Although they are point indicative measures which are not particularly accurate for anisotropic turbulence, another option is to use metrics based on the turbulence resolution length scale such as the LSR metric; see for example [153] and its application by Battistoni et al. [49] to a moving needle injection, or the similar metric by Celik et al.[152]:

$$LESIQ_\nu = \frac{1}{1 + 0.05(\frac{\mu+\mu_t}{\mu})^{0.53}} \qquad (3.8)$$

where μ_t is the sub-grid scale viscosity introduced by the WALE model. This is a number between 0 and 1 for which the constants are calibrated such that the index is perceived similar to the ratio of resolved to total turbulent kinetic energy i.e. the higher the value the better the resolution is (0.8 or above). Although [152] suggests to include as well the artificial visocsity introduced by the numerical methods, it is beyond the scope of this work to estimate such contribution. As seen in Figure 3.5 the value of $LESIQ_\nu$ for the same representative time instant is mostly over 0.95 throughout the domain and having a minimum values of 0.9 in the separation region that occurs at the entrance of the sac, confirming the suitability of the mesh.
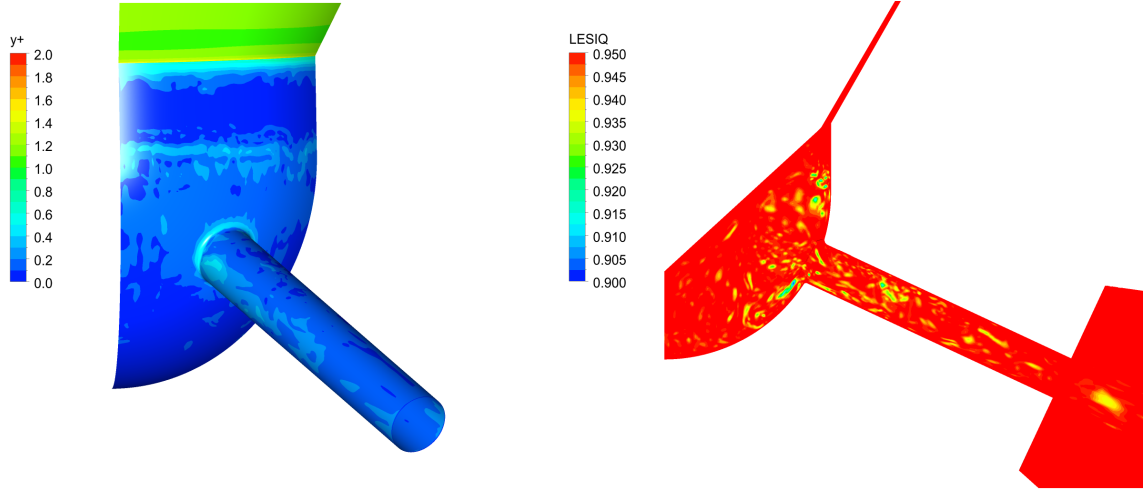

Figure 3.5: Mesh resolution evaluation. y^+ contours on the nozzle wall (left) and the LES quality metric of [152] (right) for highest needle lift during the pilot injection.

3.4   Results and discussion

The evolution of the volume fraction inside the nozzle for the different phases is shown in Figure 3.6. Additionally, the imposed needle lift extracted from the image sequence shown in Figure 3.1 is shown as well. The simulation is started at the physical time $0.4874ms$ coincident with a lift of $1\mu m$ for the imposed profile. During the opening phase it follows from this plot that initially there is air present inside the nozzle. This air is evacuated

out of the nozzle while cavitation is generated showing a peak between $0.5ms$ and $0.6ms$, while it decreases afterwards. As the injection transitions towards the closing phase the amount of vapour increases, showing a peak just after the needle closes, while the amount of air continually increases by a process of air suction as it will be shown in the following section.
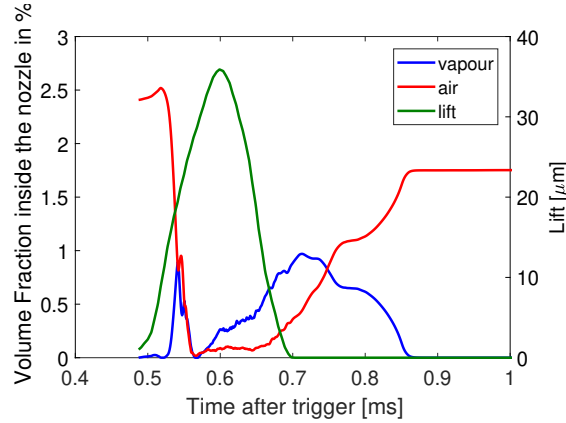

Figure 3.6: Integral results. Volume of vapour and air inside the nozzle and needle lift against time.

A comparison between the transparent nozzle tip images and the simulation results at the start of the injection is shown in Figure 3.7. In particular, a snapshot of the predicted liquid volume iso-surface of 50 at $t = 0.532ms$ is shown. At the early stages of the injection the simulation reproduces the compression of the air bubble inside the sac volume. The compression is caused by the pressure build up in the sac, justifying the inclusion of the compressibility of the air. This is quickly followed by cavitation originating at the needle seat passage, due to flow separation and shear in this area.
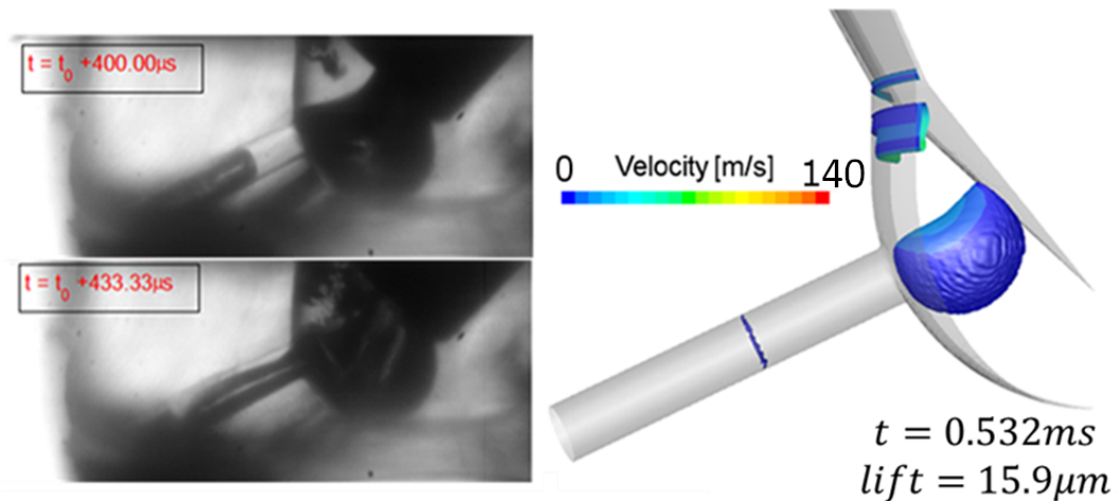

Figure 3.7: Start of injection results. Experimental visualisations (left), 50% liquid volume fraction iso-surface coloured by velocity magnitude (right).

44

Sample simulation results and the transparent nozzle tip images for the needle opening phase are shown in Figure 3.8. The CFD results indicate that cavitation produced at the sac entrance is transported directly into the injection hole. Simultaneously, the air bubble is further compressed and is pushed to recirculate parallel to the needle in the direction of the needle motion. Similarly to the experimental images, the air bubble is seen breaking down and mixing with any remaining cavitation into a fine bubbly mixture which is then advected into the hole.
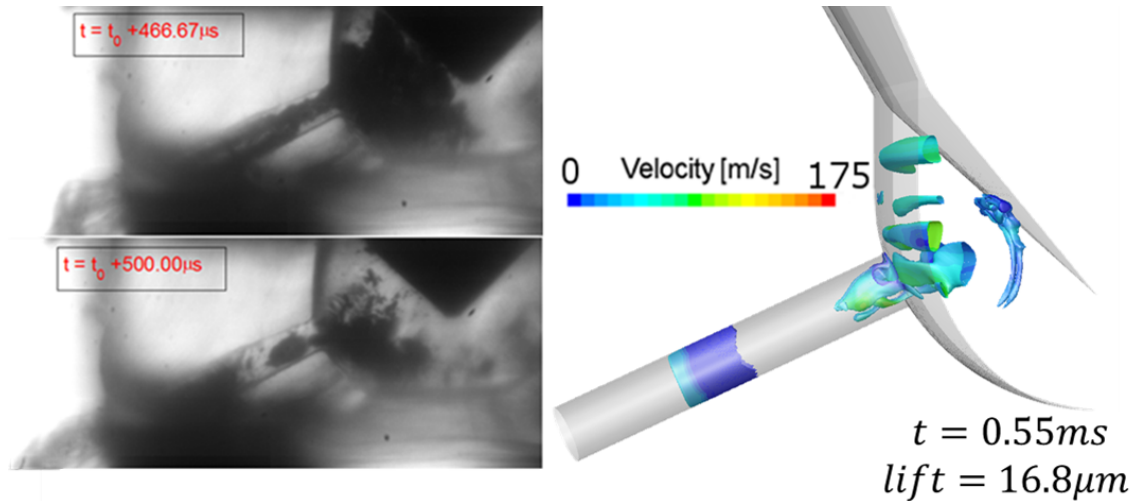

Figure 3.8: Needle opening phase results. Experimental visualisations (left), 50% liquid volume fraction iso-surface coloured by velocity magnitude (right).

As the needle lift increases and the flow further develops, the simulation indicates that air disappears from the sac volume, as seen in Figure 3.9. This is attributed to a combination of two effects. Firstly, the sac pressure build up causes the air to be compressed, reducing its volume fraction. Secondly, as the air is trapped within the recirculation zone developing inside the sac volume, it enters into the injection hole, where it expands due to the local pressure drop at its entrance. This contributes to the void areas observed and suggests that the void observed experimentally is a combination of air and fuel vapour. In addition, part of the void visible in the simulation can be attributed to geometrical cavitation developed at the hole inlet upper lip, which can be also seen from the experimental images.

The only two experimental frames available for the needle closing phase together with the simulation results are shown in Figure 3.10 (top). As the needle valve moves into the closing phase, the amount of void in the hole increases. This is in agreement with the simulation results from Figure 3.6, where volume content as a percentage of the injector volume of both air and vapour are plotted against time; it follows that these quantities increase during the needle closing phase. This void in the simulation has two sources, one from the unstable vortical flow developing inside the sac volume and entering into the
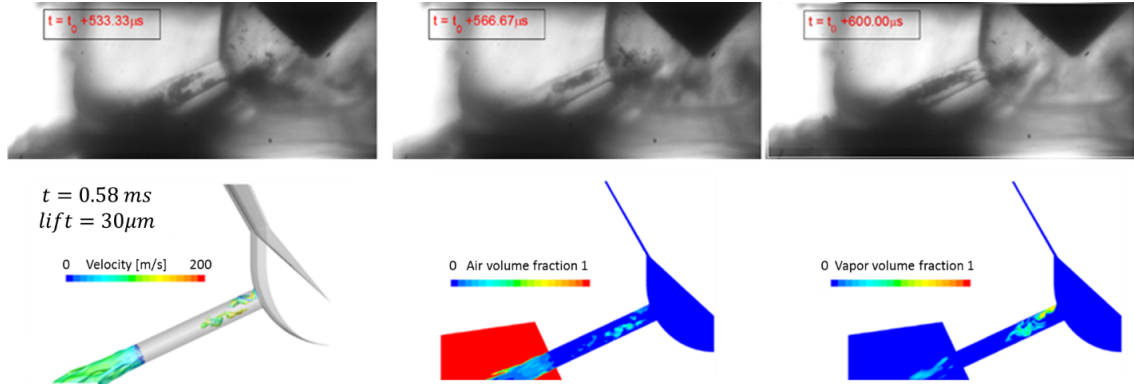
Figure 3.9: Results as flow further develops during the opening phase. Experimental visualisations for three time instances (top), 50% liquid volume fraction iso-surface coloured by velocity magnitude (bottom-left), air volume fraction contours (bottom-centre) and vapour volume fraction contours (bottom-right).

injection hole and another due to formation of geometric-induced cavitation at the hole inlet corner. Regarding the experimental results at very low lifts ($lift = 6\mu m$), a bubbly mixture appears in the sac; bubbles having sizes similar to the hole diameter appear in the hole. The simulation model predicts high velocities in the hole; however, since the flow coming from the seat is throttled a void structure appears in front of the hole. The bubbly mixture in the sac volume correlates to the void structure created in front of the hole, which is predicted to be composed of a mixture of fuel vapour and expanded air. On the other hand, the visualised bubbles computed inside the injection hole correlate to the big amount of cavitation computed in the hole.

A time sequence of the pressure field is presented in Figure 3.11. Before the needle valve closes, the predicted sac volume pressure is still higher than the ambient pressure ($t = 0.674ms$), but immediately after the needle valve closing ($t = 0.698ms$), a pressure wave is generated that travels towards the sac volume; this leaves the sac volume pressure below the ambient pressure ($t = 0.77ms$). In agreement with Figure 6, where air volume fraction inside the nozzle is seen to increase after needle closing, this induces the spray to weaken and air to be sucked back from the ambient into the nozzle until the sac pressure is balanced with the exterior pressure ($t = 1ms$).

Evidence is also provided in Figure 3.12, which shows a time sequence of air and vapour volume fraction fields. It clearly depicts the weakening flow momentum in the injection hole ($t = 0.698ms$) leading to air suction ($t = 77ms$). Finally, due to the pressure balancing with the ambient pressure, vapour completely disappears ($t = 1ms$), indicating that shortly after the needle closing only liquid and air remain inside the sac volume.
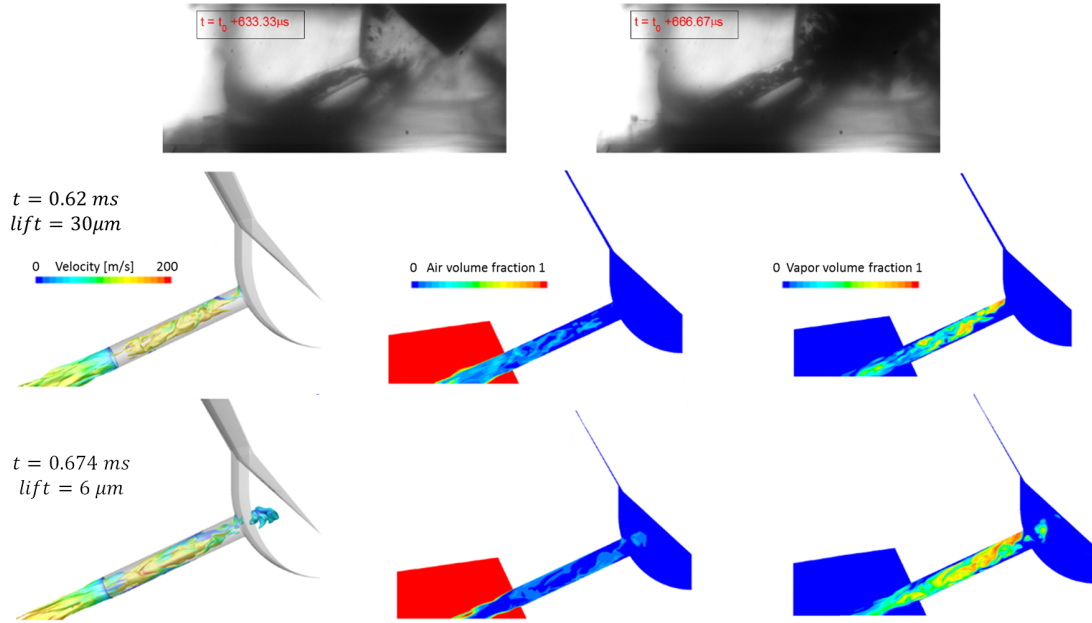
Figure 3.10: Needle closing results. Experimental visualisations for two time instants (top). Simulation results (center and bottom). For the simulation results 50% liquid volume fraction iso-surface coloured by velocity magnitude (left), air volume fraction contours (center) and vapour volume fraction contours (right) are presented.

3.5 Conclusions

This paper presents an investigation of cavitation and air interaction during a diesel pilot injection of a standard serial production six-hole geometry. The focus was to understand the complex interaction between the needle motion, cavitation formation and development, and gas suction. The strategy followed has been to use high speed visualisations of a transparent nozzle tip to record the multiphase phenomena and to use CFD to explain the physics behind the observations. The CFD methodology includes LES turbulence modelling, the needle valve movement, cavitation effects through a Rayleigh-Plesset based cavitation model, and the compressibility of both air and fuel. Starting from a flow field initialised according to the experimental observations (with an air bubble in the sac and a big portion of the hole filled with air), the main flow features observed are replicated by the simulations. In particular the following phenomena experimentally noticed have been explained and reproduced:

- The compression of the initial air bubble due to sac pressure build up. The inclusion of air compressibility in the simulation can be very relevant even for modest injection pressures in order to replicate the air compression in the sac at the start of the injection as well as the air expansion in the injection hole and sac.

- The appearance of cavitation stemming from the sac entry at the start of the injec-
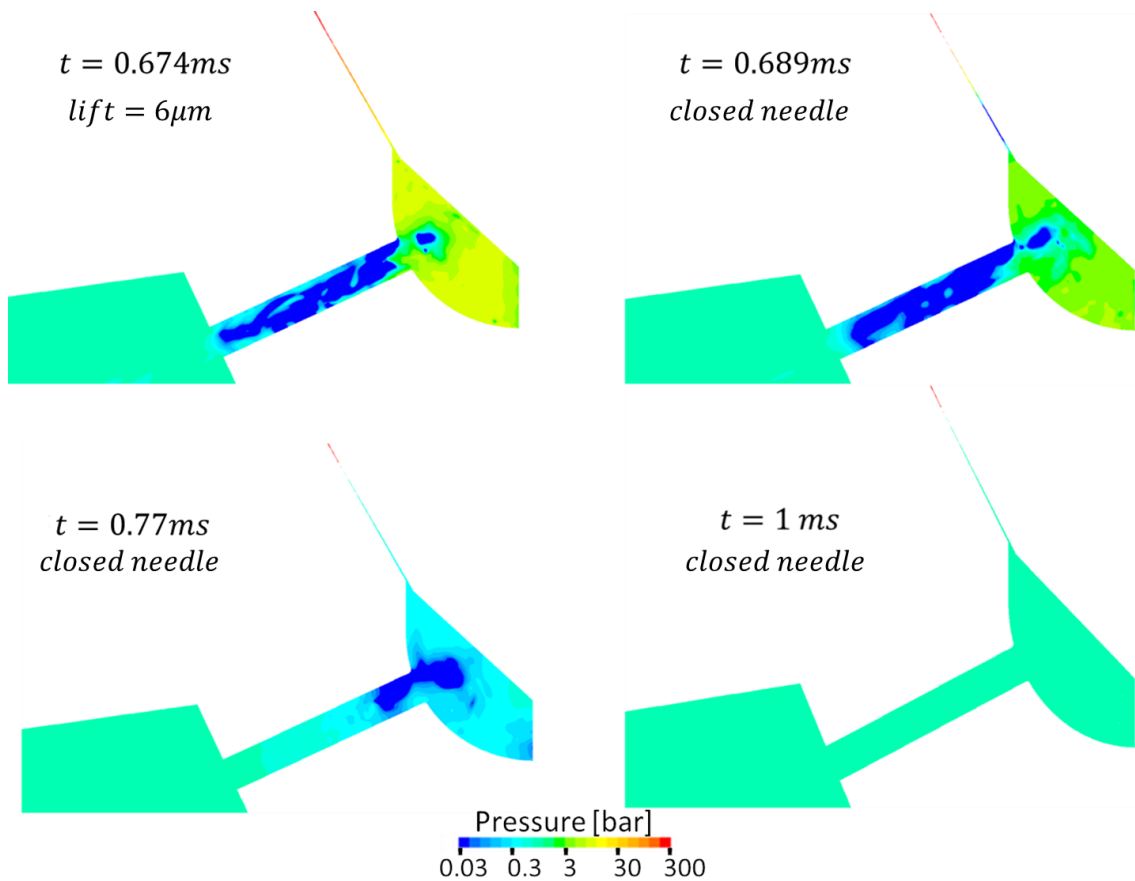
47

Figure 3.11: Pressure field time sequence. Notice that logarithmic scale has been used.

tion, due to flow separation and shear.

- The sac flow recirculation in the sac and flow patterns inside the hole. One part of the void observed in the simulation can be attributed to cavitation both geometrical (developed at the hole inlet upper lip) and vortical (due to complex flow structure coming from the sac). Furthermore, the initial air inside the nozzle expands in the hole contributing to the void areas observed. This shows that the void observed experimentally is a combination of both air and fuel vapour.

- An increase of void inside the hole and in the sac during the needle valve closing. The underlying reason being the flow throttling, since liquid momentum is still high but flow passage very restricted.

- The air suction after the needle closing. The closure of the valve creates an expansion wave that leaves the sac pressure below the ambient. This induces vapour creation and air expansion in the sac and consequently air is sucked from the ambient into the nozzle. When the pressure in the sac is recovered, all vapour collapses. Therefore, it is shown that the remaining foam at the end of the injection consists of a liquid
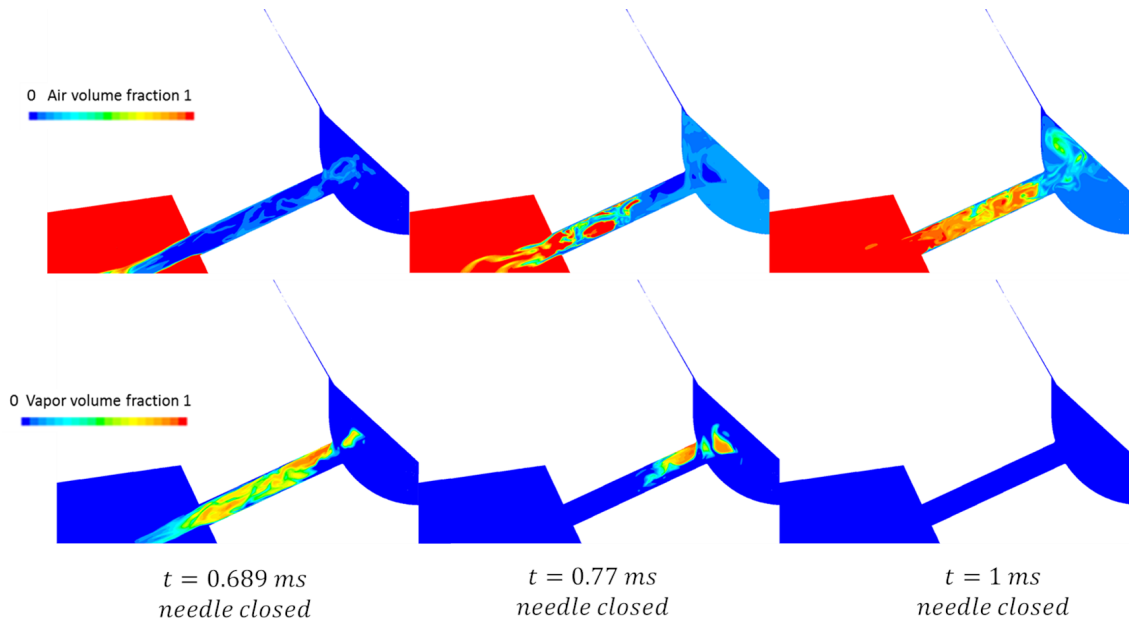
0 Air volume fraction 1

0 Vapor volume fraction 1

$t = 0.689\,ms$
needle closed

$t = 0.77\,ms$
needle closed

$t = 1\,ms$
needle closed

Figure 3.12: After needle closing results. Time sequence for air (top) and vapour (bottom) volume fraction fields.

and air mixture.

3.6   Critical Review: Modelling of the needle valve movement

In the last decade the modelling of the needle valve movement has been carried out in a variety of ways. The main methods found in the literature are linear interpolation between two base grids [35], the Cartesian cut-cell method [49], the cut-cell immersed boundary method [52, 148] and layering and stretching [20]. Modelling the dynamic movement of the needle is inherently difficult. At low lifts the cells in the seat are squeezed into very small gaps deteriorating their quality, which can have an impact on the robustness and accuracy of the simulation. Moreover, the contact between walls is not trivial to model since the continuity of the mesh is broken. Recent advances have been reported in [148] where the immersed boundary method has allowed simulations to be performed even at zero needle lift; however, this method has not been adopted here and as a compromise, the closed needle is modelled switching the needle seat surface (surface of minimum distance between needle and housing) to a wall when the needle lift is below a pre-fixed lift (usually $1\mu m$ in this Thesis). In general, the imposed needle profile can be taken from a 1D injector model simulation or measured from experiments.

Within this project both the mesh interpolation approach and the layering and stretching algorithms where tested for the simulation of the Diesel transparent nozzle tip. These

49

preliminary runs to decide on the method to follow were done with the same nozzle geometry and simulation setup as the one presented in Chapter 3 but with URANS turbulence modelling for reduced mesh resolution and computational time.

The stretching and layering algorithm is already inbuilt in Fluent and has been adapted from [20], below a certain prescribed lift ($10\mu m$) the mesh is stretched by propagating the wall movement into the grid, and for higher lifts the method increases the size of a single layer which is split in half when its size exceeds a predetermined threshold ($8\mu m$).

The interpolation approach is implemented into Fluent through a UDF and performed between two topologically identical meshes (base-grids) with the same number of cells. The initial mesh has a $1\mu m$ lift and the high lift mesh is based on the maximum lift reached for the injection. Based on the node position of this two meshes any intermediate lift is achieved by linear interpolation between the node position of the two base-grids. Another difficulty associated is the loss of resolution in the seat passage as the needle reaches high lifts, this requires interpolating the results into another pair of key-grids such as in [35]. This is mostly needed in Diesel fuel injectors or high flow GDi injectors for which the high needle stroke can induce a loss of resolution. However for the cases considered during this project, this was not needed due to the relatively low lift attained.

The comparison of the predicted mass flow rate through the needle seat surface for both methods is shown in Figure 3.13 (top). It can be observed that the predicted mass flow rate is very close for both methods, however the stretching+layering approach presents flow oscillations. A closer inspection of the mesh for this method reveals that this flow disturbances arise every time a layer is introduced Figure 3.13 (bottom). Since the mesh interpolation approach does not introduce any flow disturbance or oscillation it finally was the chosen method.
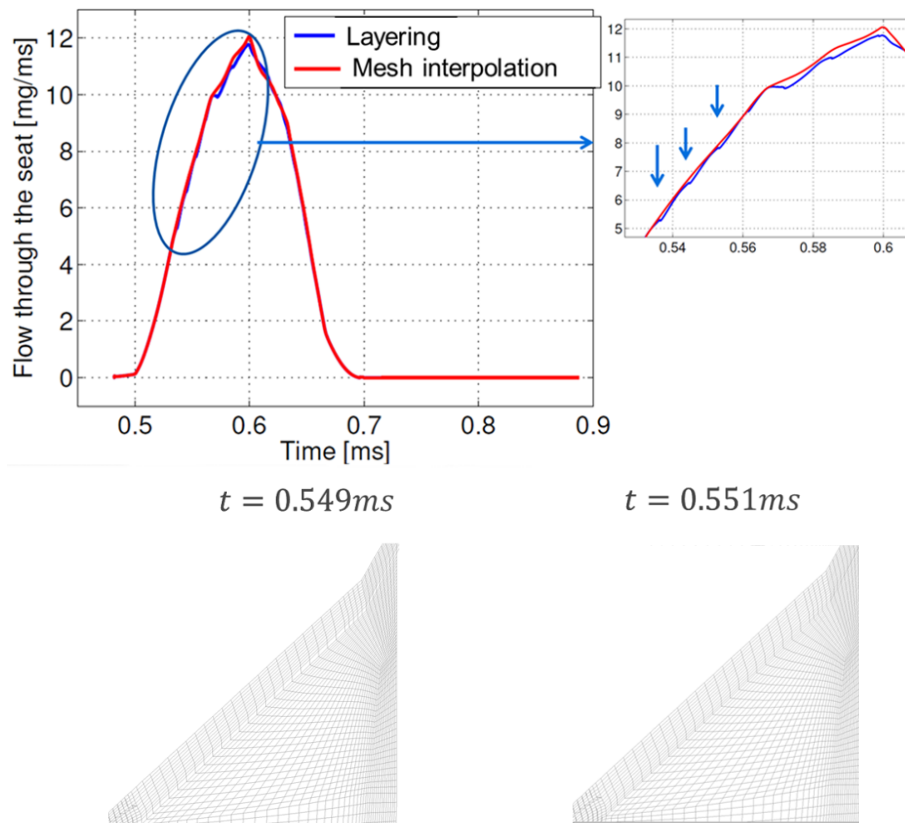
Figure 3.13: Comparison between mesh interpolation and layering methods. Mass flow rate through needle seat surface (top) and mesh zoom for the layering case (bottom)

Chapter 4

Modelling and prediction of cavitation erosion in GDi injectors operated with E100 fuels

This Chapter is based on my second publication befor its review (the final version was accepted for publication on the 28th November 2020 in FUEL). Ethanol (E100) as a renewable fuel is an attractive option for spark ignition engines to reduce their net CO_2 emissions, but it is well known that E100 influences the durability of hydraulic components. This work reports for the first time CFD predictions for locations prone to cavitation erosion in multi-hole GDi injectors operated with E100 fuels combined with experimental evidence of erosion damage after 400M injection cycles. To the best of my knowledge there is no paper in the literature dealing with the cavitation erosion phenomena and the three-phase flow (liquid, vapour and air) inside a GDi injector during the opening/closing of the needle valve.

The literature on this topic has been examined and critically correlated to the topic under investigation. A combination of LES and URANS together with a barotropic equation of state for modelling cavitation is used to assist in the interpretation of the underlying erosion physics. A barotropic equation of state is used to capture the correct collapse speed of collapsing vapour structures and its implementation is verified against the Rayleigh collapse of a vapour bubble. The performance of several cavitation erosion indices found in the literature has been evaluated for this particular problem and it is found that the numerical framework is capable of reproducing the observed cavitation erosion locations. The flow was thoroughly analysed, including the impact of air entrainment in subsequent injections and conclusions on the reasons for the observed erosion locations are derived.

I curated the erosion damage images for the investigation, developed and implemented the cavitation model into the CFD software, implemented the erosion indicators into

the CFD software, used the simulation methodology developed in Chapter 3, generated the grids, performed the simulation, analysed the results, produced a big part of the visualisations, supervised the PhD. student that generated the rest (Ramesh) and wrote the original draft of the manuscript.

4.1 Introduction

The increased use of bio-ethanol as a renewable fuel can facilitate the automotive industry to significantly reduce their net CO_2 emissions. For this reason bio-ethanol blended fuels have gained increasing interest in the transportation sector in order to meet the emission limits imposed by the different legislations worldwide. In Europe, E10 (10% ethanol-gasoline fuel mix) is the standard fuel mix for petrol engines, while a further increase of the ethanol percentage is under discussion by the relevant bodies. In Brazil there is even a market demand for developing engines able to run with E100 fuels [1].Due to its the production process, ethanol fuel can contain water and trace contaminants such as inorganic chlorides and sulphates, which can cause corrosion damage and deposit formation to the hydraulic components of the fuel injection system; thus, causing durability issues [154]. It is generally understood that the corrosion damage can be enhanced by cavitation erosion. Formation of cavitation inside GDi nozzles and its impact on the spray behaviour was reported in [113]. Besides, GDi engines are moving towards using higher injection pressures in the range of $350bar$ to more than $500bar$. The high pressure of the system enhances the cavitation occurrence and as a consequence the cavitation erosion risk in hydraulic components. In the present investigation, durability tests employing 400 million injection cycles have been performed at Delphi Technologies for some prototype nozzles; surface damage in the sac volume walls and spray hole inlet (where cavitation occurrence is expected) have been observed when E100 fuel was utilised.

Cavitation can be described as the process of vapour formation when the local pressure falls below the vapour pressure of the flowing liquid [93, 99]. Some authors have described it as analogous to fracture in solid materials as the local principal stresses increase beyond the vapour pressure [155]. Cavitation bubbles grow in low pressure regions from pre-existing nuclei, dissolved in the liquid (in similar fashion to boiling) [131, 81, 156]. When pressure recovers to values above the liquid's vapour pressure, vapour condenses back into liquid creating strong pressure waves, which can damage the nearby walls close to the collapse [157]. Remarkably, the cavitation collapse process can result in light emission and temperatures in some cases of the order of $9000K$ very localised in time and space [158, 141]. Given the severity of cavitation collapse, plastic deformation and/or erosion of metallic surfaces causing performance drift and/or failure in multiple industrial scenarios such as in for example ship propellers [159], and high pressure fuel injection systems

(including pumps [115, 160] and injectors [20]) have been reported.

Additionally, liquids usually contain dissolved gases that are released by pressure drop or cavitation [161]; therefore cavitation bubbles typically contain gases which greatly affects the collapse dynamics and severity [162]. Indeed, it was shown in [163] and numerically reproduced in [164] that the initial energy of a bubble splits into the rebound energy and the energy carried away by the emitted shock wave. Free gas content (given by the gas partial pressure inside the vapour bubble) has a damping effect that weakens the pressure wave and enhances the bubble rebound. As explained in [165, 166] common cavitation bubble collapse experiments use laser or spark-induced bubbles that behave like hydrodynamic cavitation bubbles; when the maximum radius is reached, the bubble dynamics are no longer influenced by the initial hot plasma forming inside the bubble.

The experiments of [91] with transparent glass GDi nozzles using different fuels relevant to spark ignition engines (including pure gasoline, E10 and E100 fuels), with injection temperatures ranging from $20C^o$ to $90C^o$ and back pressures ranging from $0.5bar$ to $1bar$ show that cavitation occurs at all the conditions tested. Further transparent nozzle experiments also confirm the presence of cavitation in GDi injectors [92, 27, 167]. Cavitation inside fuel injectors presents several distinct morphologies. Sharp throttle corners usually induce the so-called cloud cavitation which forms during the growth of cavitation bubbles at the entry of the injection hole; this is followed by shedding of the formed vapour clouds due to flow instability (see selectively [21, 25, 81]). Moreover, the swirling flow conditions prevailing due to the complex recirculation of the flow inside the injector's sac volume, also induce cavitation at the core of the formed vortices (so-called string cavitation, see selectively [140, 106, 78]). Notwithstanding, during the dynamic movement of the injector needle valve, needle seat cavitation has been observed [106] and substantial cavitation in the nozzle's sac volume at the end of the injection has been numerically predicted [52, 81]; distinguishing vapour from ingested air is not straightforward from experimental observations.

In terms of modelling the cavitating flow in fuel injection applications both Eulerian and Eulerian-Lagrangian [122] approaches have been reported, including full thermodynamic closure and friction-induced heating effects in high pressure fuel injection systems [35, 36, 34]; but the former seem to be prevalent in the recent literature. In Eulerian heterogeneous multi-fluid models (in their most general form) each phase has its own pressure, velocity and temperature; source terms in the conservation equations determine the momentum mass and energy exchange between the phases [37]. These models unavoidably present increased modelling and computational requirements. Under the assumption of all phases sharing the same pressure and isothermal flow [86], in a throttle flow resembling a Diesel injector, the slip velocity between the phases was found to be less than 15% of the liquid bulk velocity and only in very localized regions. As the inertia of the vapour/air

phases is small compared to that of the bulk liquid [38], mechanical and thermal equilibrium can be assumed, leading to a single velocity field for all co-existing phases. These models are known as homogeneous mixture or single-fluid models and resemble the traditional single-phase Navier-Stokes equations complemented by an additional transport equation expressing the mass conservation of vapour; a source term can be used to model the mass transfer between liquid and vapour. In the context of homogeneous mixture models, source terms based on the Rayleigh-Plesset equation for the collapse of a vapour bubble [99], such as the Schner-Sauer (SS) model [94] and the Zwart-Gerber-Belarmi (ZGB) model [40] are widely used; other formulations also exist [168] and are globally known as finite mass transfer models. These models contain empirically calibrated constants that determine the mass transfer rate and have been shown to be equivalent if the constants are chosen appropriately [95]. In their original formulation, these models typically utilise low values of the calibration constants, which results in nonphysical negative pressures (theoretically corresponding to liquid tension, but numerically presenting large errors [33]). Moreover, this also results in a severe over-prediction of the collapse time of cavitation bubbles [33, 169, 170]. The error can be reduced by model calibration to match the critical cavitation point measurement (CCP) for different throttle configurations as is reported in [171]; still this empirical approach is not efficient and reliable considering that all the model parameters need to be calibrated simultaneously. The ad-hoc increase of the calibration coefficients corrects these issues and is in line with the experimental evidence of [172], where the pressure inside a cavitation cavity for a flow of water through a throttle was measured. For water, there is a close agreement between the measured pressure and the vapour pressure, which indicates that the cavity is almost filled with saturated vapour of water and that the vapour and liquid mixture is in thermodynamic equilibrium. This motivates the use of thermodynamic equilibrium models in which the mixture's vapour volume fraction is obtained from the mixture density and the saturation densities of liquid and vapour at the equilibrium temperature, without the need to solve for any additional transport equation [41, 42]. Thermodynamic equilibrium models can be further simplified by not solving the energy equation and considering the density to be exclusively a function of pressure (barotropic models). Simulation results for the collapse of a bubble cluster show negligible impact of the barotropic assumption on the collapse characteristics of bubble clusters [173]; similarly, simulation results for a cavitating mixing layer show negligible heating effects [174]. Finally, barotropic models are essentially equivalent to finite rate mass transfer models with increased mass transfer coefficients in some fundamental test cases; e.g., 1D shock tests, 2D Rayleigh bubble collapse [33] and in 3D throttle flows [175]. However, as discussed in [33] one possible shortcoming of this last assumption is that it does not consider vorticity production due to pressure and density gradient misalignment (baroclinic torque). The interested reader can further refer to [42]

and [33] for reviews of modelling aspects of turbulent cavitating flows.

Resolution of turbulent structures is key in describing vortex cavitation, cavitation shedding and flow unsteadiness. URANS models may fail to predict simple shedding in throttle flows, although by modifying and reducing the eddy viscosity in cavitating regions the unsteadiness can be reproduced in some situations [50, 51]. Despite this, in [33] URANS models failed to predict incipient cavitation when the pressure difference driving the flow was low. This shows that URANS models are situational and lack universality in the prediction of cavitation. On the other hand, scale resolving simulations (such as LES and DES) can predict the formation of cavitation in the case of incipient cavitation for both barotropic and finite rate mass transfer models [33]. This type of modelling can also predict areas prone to cavitation erosion in fuel injectors, using both finite rate mass transfer [20] and barotropic models [52]; they have been thoroughly validated up to the accuracy of the measuring devices in the case of finite rate mass transfer models [43]. Unfortunately, the computational cost of scale resolving simulations is still prohibitive for use in daily industrial simulations; see for instance the data discussed in [20, 33] for fuel injection applications.

Identifying the parameters that are most suitable for cavitation erosion in a CFD simulation is still an open research question. Thanks to the advances in scale resolving simulations, detailed understanding of the cavitation erosion process and relevant mechanism have been revealed. Some studies rely on resolving the mechanical loads of cavitation collapses reaching the walls and recording the maximum pressure [20, 52]. The drawback of this method is that the value of the recorded pressure peaks can be mesh and time resolution dependent [41, 170]. In addition in fuel injectors due to the moving needle valve, the sac volume pressure presents variations of the order of the injection pressure which can obscure pressure peaks arising during the different injection phases [82]. Other investigations have successfully explored methods based on the potential energy available in cavities [176, 170, 177] or pressure time derivatives [178, 160]. Nevertheless, a simulation tool suitable for obtaining cavitation erosion diagnostic at industrailly affordable computational time scales while being able to support and interpret the durability tests, is very much desirable in the relevant industries.

Nowadays, cavitation erosion diagnostic in the industry still relies on durability tests. Injector durability tests are expensive since they require many operation cycles and they do not reveal the detailed flow processes leading to erosion; still, they can be used to validate relevant simulation models, which in turn are helpful to understand the underlying physics.

This work focuses on modelling the turbulent cavitating flow inside multi-hole GDi injectors operated with E100. The target is to develop an effective erosion diagnostic tool able to support, interpret and reduce the time and cost of durability tests. Ideally, LES of several injection cycles for the full nozzle geometry, including the needle valve

movement is required from a model fidelity point of view in order to resolve turbulence. Unfortunately, computational resources prohibit the use of such models and practically restrict them to the simulation of only a single injection event of just a sector of the full nozzle geometry, assuming periodic boundary conditions. Instead, URANS simulations are feasible for several injection cycles and the full nozzle geometry. However, using purely URANS entails risks as to whether the correct flow physical behaviour is being captured; thus, a reference LES solution to verify the URANS solution for the particular geometry is needed.

Regarding simulations of GDi nozzle flow, the so-called "Spray G" injector of the Engine Combustion Network (ECN) with moving needle valve has been studied with URANS for instance by [89], in order to predict spray targeting and provide input for subsequent Lagrangian spray simulations; in [90] they predicted the existence of cavitating vortices and linked their dynamics to oscillations in the mass flow rate and the forming spray. LES investigations have also been carried out focusing for example on the impact of real geometry features [72] or the effect of unresolved scales [123] in atomization. However, to the best of the author's knowledge, this is the first CFD investigation of cavitation erosion in a 5-hole GDi injector nozzle utilising E100, while combining both LES and URANS. Initially, a 72° sector of the nozzle geometry is simulated using LES. The LES approach is applied to ensure the model fidelity and accurate resolution of turbulent structures. Following, and in order to account for the injector's hole-to-hole interactions, a URANS simulation for the full nozzle geometry is also simulated. Additionally, the impact of the residual liquid remaining in the sac volume during the multiple cycle operation of the injector for the full nozzle geometry in the case of URANS modelling is discussed.

The paper is structured as follows; first an overview of the observed erosion patterns appearing after 400million injection cycles durability test on the GDi injector nozzle tip operated with E100 is provided. Then, the modelling approach is described in detail including the verification of the cavitation model against the Rayleigh collapse of a vapour bubble. Simulation results are then discussed and detailed information about the arising cavitation and the mechanisms behind the different erosion phenomena are provided.

4.2 Injector durability tests and observed erosion patterns

The experimental campaign consisted of seven 5-hole injectors submitted for durability analysis while operated with E100. The rail pressure in the tests was $350\,bar$. The hardware tests were performed at a temperature of, $T_{inj} = 40C^o$ and discharged into the ambient which corresponds to a back pressure of $p_{back} = 1atm$. The operating conditions correspond to ethanol vapour saturation pressure of $p_{sat}(T_{inj}) = 17909\;Pa$, while the saturation temperature obtained at the downstream pressure is $T_{sat}(p_{back}) = 78C^o$[179].

Therefore, ethanol is not injected in superheated state and the phase change under this conditions is driven by cavitation and not flash-boiling. The injections had an electrical pulse of $1\,ms$, and they were separated by $6\,ms$; the test was ran for 400 million injection cycles. The injection holes have a mean diameter of $170\,\mu m$ and length-to-diameter ratio of $L/D \sim 1$. After the tests, several erosion patterns were found during inspection of the parts using scanning electron microscope (SEM). All parts showed damage in areas where cavitation is expected to form and develop. Figure 4.1 presents the SEM images for three of the injectors; more specifically damage at the injection hole inlet, sac volume entry, sac center and in the injector's sealing band (pintle needle valve seat) can be observed.
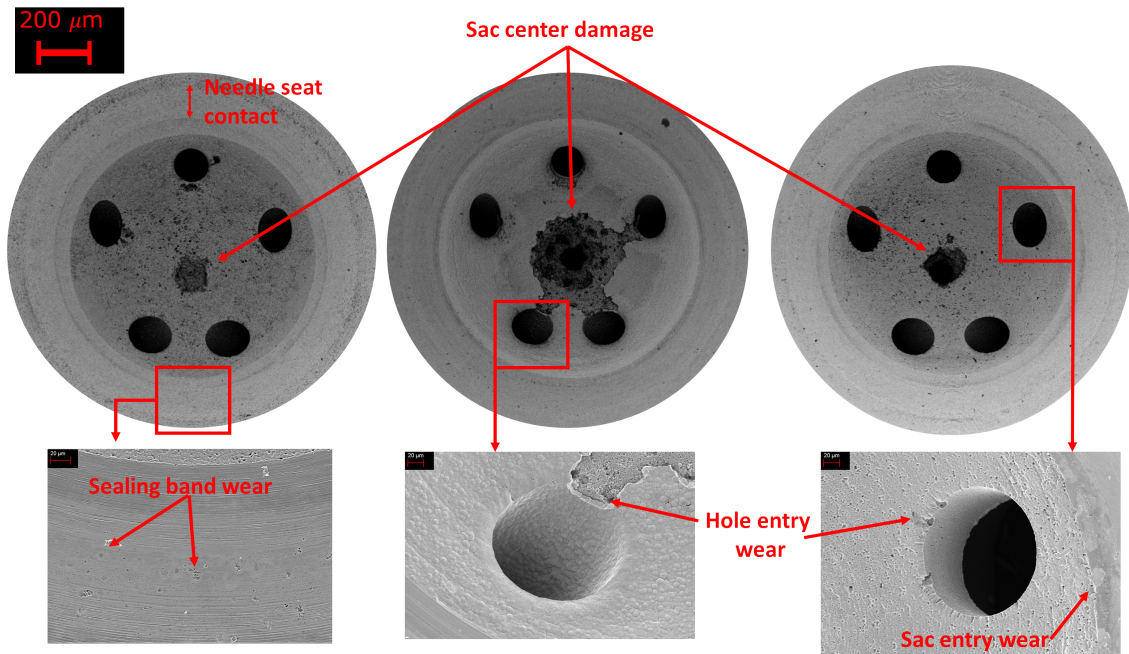

Figure 4.1: Damage patterns observed in a GDi nozzle after 400 M cycle durability test.

4.3 Modelling approach

The compressible formulation of the Navier-Stokes equations is solved numerically using the commercial CFD code ANSYS Fluent [85]. The multiphase flow is simulated using a three-phase (fuel liquid, fuel vapour and air) homogeneous mixture model, where all phases are assumed to be in mechanical and thermal equilibrium; thus, they share the same velocity and pressure. The flow is assumed isothermal and the energy conservation equation is not considered. A barotropic model has been implemented through a user defined function (UDF) specifying the variation of the fuel density as a function of pressure; additional UDFs are also used for accounting the needle valve movement and the cavitation induced surface erosion indicators.

4.3.1 Multiphase model

The physical properties appearing in the transport equations are determined by the corresponding values of the properties of the component phases in each control volume. Defining α_{fuel}, α_{air} as the volume fraction of fuel and air in a cell, respectively, the density in each cell is given by: $\rho = \alpha_{fuel}\rho_{fuel} + \alpha_{air}\rho_{air}$. Viscosity is computed using the same mixing rule between fuel and air, while it is assumed to be constant for each phase. The solved equations consist of the continuity and momentum equations for the mixture and the mass conservation equations for the air, where the volume constraint $\alpha_{fuel} + \alpha_{air} = 1$, in each cell must be respected:

$$\frac{\partial \rho}{\partial t} + \nabla \cdot (\rho \mathbf{v}) = 0 \tag{4.1}$$

$$\frac{\partial \rho \mathbf{v}}{\partial t} + \nabla \cdot (\rho \mathbf{v}\mathbf{v}) = -\nabla p + \nabla \cdot \sigma \tag{4.2}$$

$$\frac{\partial \alpha_{air}\rho_{air}}{\partial t} + \nabla \cdot (\alpha_{air}\rho_{air}\mathbf{v}) = 0 \tag{4.3}$$

The effective viscous stress tensor is defined as $\sigma = \tau + \tau_t = \mu(\nabla \mathbf{v} + (\nabla \mathbf{v})^T) + \tau_t$, where μ is the viscosity of the mixture and τ_t are the turbulent stresses estimated from the turbulence model used.

4.3.2 Turbulence model

The target when using LES is to capture the large scales that are dependent of the physical domain simulated while modelling the sub-grid turbulent scales. This is achieved by filtering of the Navier-Stokes equations using a spatial low-pass filter determined by the cell size of the computational domain used. This operation leaves the operators of the solved differential flow equations unchanged, considering the filtered magnitudes, while additional terms appear in the solved equations; these represent the sub-grid scale contributions to the equations of motion that have to be modelled [46]. The corresponding sub-grid scale model for the turbulent dissipation (viscosity) μ_t is the Wall-Adapting Local Eddy-Viscosity (WALE) model [118]. This model is capable of reproducing the turbulence wall behaviour ($\mu_t \sim o(y^3)$) and becomes 0 at $y = 0$, where y represents the normal distance to the wall. Another advantage is that it returns a zero turbulent viscosity for laminar shear flows; this is necessary for modelling the start of injection, when flow velocities are low.

On the other hand, Reynolds-averaged Navier–Stokes (RANS) or unsteady RANS (UR-ANS) provide the solution for the spatial and temporal mean flow variables at significantly reduced grid resolution as compared to LES. In the present work the $k - \omega\ SST$ model is employed; this is a blend between the standard $k - \varepsilon$ and $k - \omega$ models, and accounts

two additional transport equations for modelling the turbulent kinetic energy (k) and its specific dissipation rate (ω); it offers better accuracy in the vicinity of walls than the $k - \varepsilon$ and less sensitivity to the boundary conditions than the $k - \omega$ model [112].

4.3.3 Cavitation model

The proposed polynomial barotropic cavitation model is similar to that presented in [97]. Given the vapour saturation pressure of the working fluid p_{sat} and a pressure interval δp over which the mass transfer takes place we can define:

$$
\begin{aligned}
p_{satL} &= p_{sat} + \frac{\delta p}{2} \\
p_{satV} &= p_{sat} - \frac{\delta p}{2}
\end{aligned}
\tag{4.4}
$$

The fuel is in liquid state when $p > p_{satL}$ and follows a Tait equation of state (EOS):

$$
\rho(p) = \rho_{satL} \left(\frac{p - p_{satL}}{B'} + 1 \right)^{1/n}, \; p > p_{satL}
\tag{4.5}
$$

The constants n and B' are dependent on the fluid and in the case of ethanol have been fitted from the density measurements of [103]. Figure 4.2 (left) shows the comparison of the fitted equation of state and the measured density data. Figure 4.2 (right) shows that the error of the fitting is below 0.03% for all pressures in the measurement range.
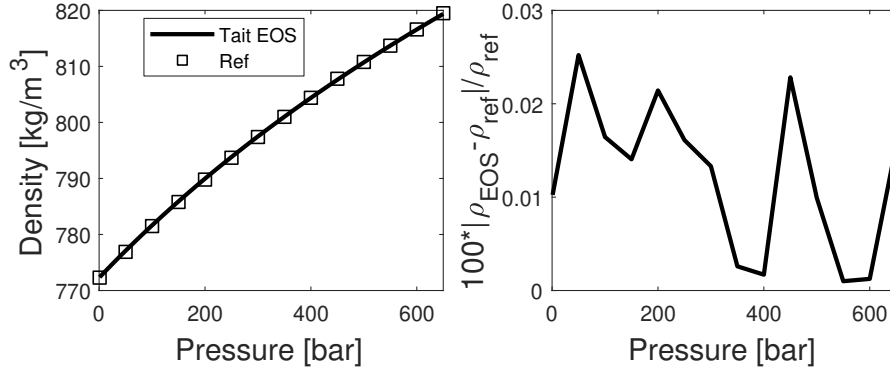

Figure 4.2: Comparison between the fitted Tait EOS and the density measurements of [103]. Desnity vs pressure (left) and % difference between fitted equation and measurements (right)

The model assumes a polytropic evolution for the vapour phase (when $p < p_{satV}$) and a third order polynomial for the mixture (when $p_{satV} < p < p_{satL}$). The full barotropic cavitation model proposed reads as:

$$
\rho_{fuel}(p) = \begin{cases} \rho_{satL}(\frac{p-p_{satL}}{B'}+1)^{1/n} & p > p_{satL} \\ Ap^3 + Bp^2 + Cp + D & p_{satV} < p < p_{satL} \\ (\frac{p}{C_{vap}})^{1/\gamma_{vap}} & p < p_{satV} \end{cases} \tag{4.6}
$$

In the case of the vapour phase, the value of γ_{vap}, C_{vap} can be determined by knowing the vapour phase density ρ_{satV} at pressure p_{satV}. Numerical trials have shown that using low values of ρ_{satV} leads to difficulty in obtaining a stable solution. Constants A, B, C, D for the mixture are unknown and they are calculated so that both density and speed of sound ($c_{fuel}^2 = \frac{\partial p}{\partial \rho_{fuel}}$) are piecewise continuous by solving the following linear system of equations:

$$
\begin{aligned}
Ap_{satL}^3 + Bp_{satL}^2 + Cp_{satL} + D &= \rho_{satL} \\
Ap_{satV}^3 + Bp_{satV}^2 + Cp_{satV} + D &= \rho_{satV} \\
3Ap_{satL}^2 + 2Bp_{satL} + C &= 1/c_{satL}^2 \\
3Ap_{satV}^2 + 2Bp_{satV} + C &= 1/c_{satV}^2
\end{aligned} \tag{4.7}
$$

This model presents a small pressure interval δp over which the mass transfer takes place and regulates the compressibility of the mixture (minimum speed of sound in the mixture). For homogeneous mixtures according to [93, 99] the minimum speed of sound should be between two extremes; the frozen speed of sound (no mass transfer assumed) and the equilibrium speed of sound (infinitely fast heat exchange and mass transfer); therefore the value of $\delta p = 20000 \ Pa$ is chosen to respect these bounds. The dependence of the fuel density, vapour volume fraction ($\alpha_{vap} = \frac{\rho_{satL}-\rho_{fuel}}{\rho_{satL}-\rho_{satV}}$) and speed of sound against pressure as well as the dependence of the speed of sound with the vapour volume fraction are all shown in Figure 4.3. Finally, the non-condensable air is modelled via an isentropic equation of state ($\rho_{air} = (\frac{p}{C_{air}})^{1/\gamma_{air}}$), where the constant C_{air} is calculated at ambient conditions (1 bar and 293 K); see Table 4.1 for the values of all the constants related to the fuel properties.

Liquid properties		Vapour properties		Air properties	
ρ_{satL}	772.3 kg/m^3	ρ_{satV}	1.2 kg/m^3		
p_{satL}	7909 Pa	p_{satV}	27909 Pa		
n	11.09	γ_{vap}	1	γ_{air}	1.4
B'	$7.007 \times 10^7 \ Pa$	C_{vap}	23258 $Pa/(kg/m^3)$	C_{air}	85708 $Pa/(kg/m^3)^{1.4}$
c_{satL}	1003.08 m/s	c_{satV}	80.35 m/s		
μ_L	$8.22 \times 10^{-4} \ Pa \ s$	μ_V	$2 \times 10^{-5} \ Pa \ s$	μ_{air}	$2 \times 10^{-5} \ Pa \ s$

Table 4.1: Fluid properties of ethanol and air used.

The model implementation has been verified against the Rayleigh spherical bubble collapse solution, describing the compression of a vapour bubble embedded in an infinite
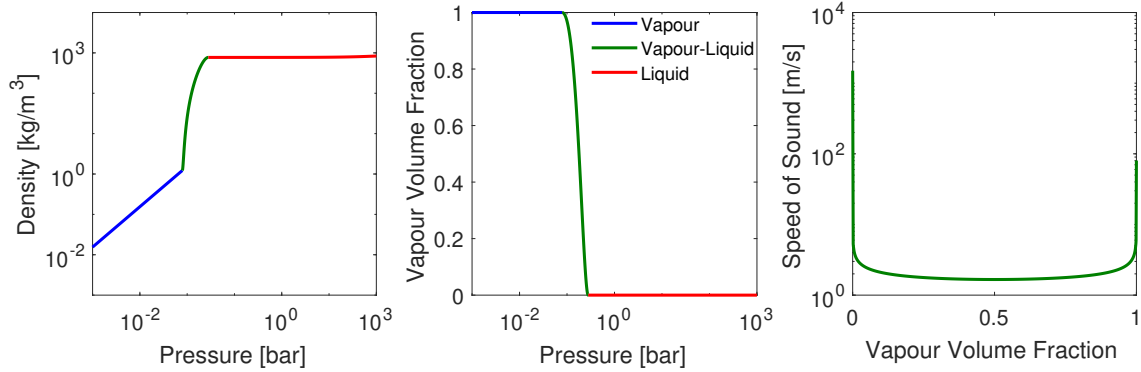
Figure 4.3: Polynomial barotropic EOS. Density (left), vapour volume fraction (middle), speed of sound vs vapour volume fraction (right).

high pressure liquid. The bubble wall collapse velocity is given in this case by [99]:

$$\frac{dR}{dt} = -\sqrt{\frac{2}{3}\frac{p - p_{sat}}{\rho_L}((\frac{R_0}{R}))^3 - 1)} \tag{4.8}$$

Where p is the far field pressure, p_{satV} is the vapour saturation pressure, ρ the liquid density, R_0 is the initial bubble radius and R is the bubble radius at time t. Integration of the previous equation yields an approximate collapse time of $\tau \approx 0.915 R_0 \sqrt{\frac{\rho_L}{p - p_{sat}}}$ [99].

The model is verified for a 2D axis symmetric case, starting from a 20 μm radius bubble at p_{satV}, embedded in 100 bar liquid. The difference found in the collapse time is 2.6% while yielding in the process a pressure in excess of 15000 bar at the bubble centre.

4.3.4 Moving mesh simulation methodology: mesh generation, boundary conditions and numerical setup.

The tested injector consists of a 5-hole GDi injector with nozzle hole diameter of 170 μm. In the case of LES, due to its demanding computational time only a 72° sector is simulated and periodic boundary conditions are considered (Figure 4.4 top). Pressure boundary condition are imposed at the inlet (350 bar) and at the outlet (101325 Pa). In the URANS case the full nozzle geometry is simulated.

The LES model setting is adapted from the basis of the previous studies on Diesel injection and primary breakup [17, 19, 119, 83, 81] and Gasoline [82, 12] injection and primary breakup simulations. In order to choose the appropriate filter/mesh size for the LES, the Taylor micro-scales (λ_g) is used [46]. This is an intermediate length scale at which fluid viscosity significantly affects the dynamics of turbulent eddies in the flow [47]. An estimation of the Reynolds number inside of the injection hole yields a value of $Re = \frac{(\rho V D)}{\mu} \sim 48000$, in turn this corresponds to a $\lambda_g \sim \sqrt{\frac{10D}{Re}} = 1.8 \ \mu m$. Consequently, a fully hexahedral mesh was created with the aforementioned resolution in the regions of interest, namely the seat, sac and spray hole, and was progressively coarsened in the

counter bore and discharge volume regions. Since resolution of the smallest eddies in the wall vicinity requires the non-dimensional wall distance based on the friction velocity to be of the order of 1 ($y^+ \sim 1$) [46], additional refinement is applied in the wall region. A mesh size of $\sim 0.5\ \mu m$ is used close to the walls. The average y^+ is about 1 in the region of interest and the maximum wall y^+ is about 10 around the sharp edge of the spray hole entrance. This results in a mesh count of 2.3 M elements for a geometrical sector in the LES case. The authors reported in [81] different LES quality metrics confirming the suitability of the mesh design method for a Diesel pilot injection and for conciseness these quality metrics are not reported here. In the URANS case, the resolution requirements are relaxed and a 2.7 M fully hexahedral mesh is employed for the full nozzle. This mesh resolution has been verified to be able to predict the mass flow rate at full lift and different injector designs with an accuracy of 3%, again for conciseness these results are not reported here. Table 4.2 presents the summary of the employed meshes for LES and URANS simulations.
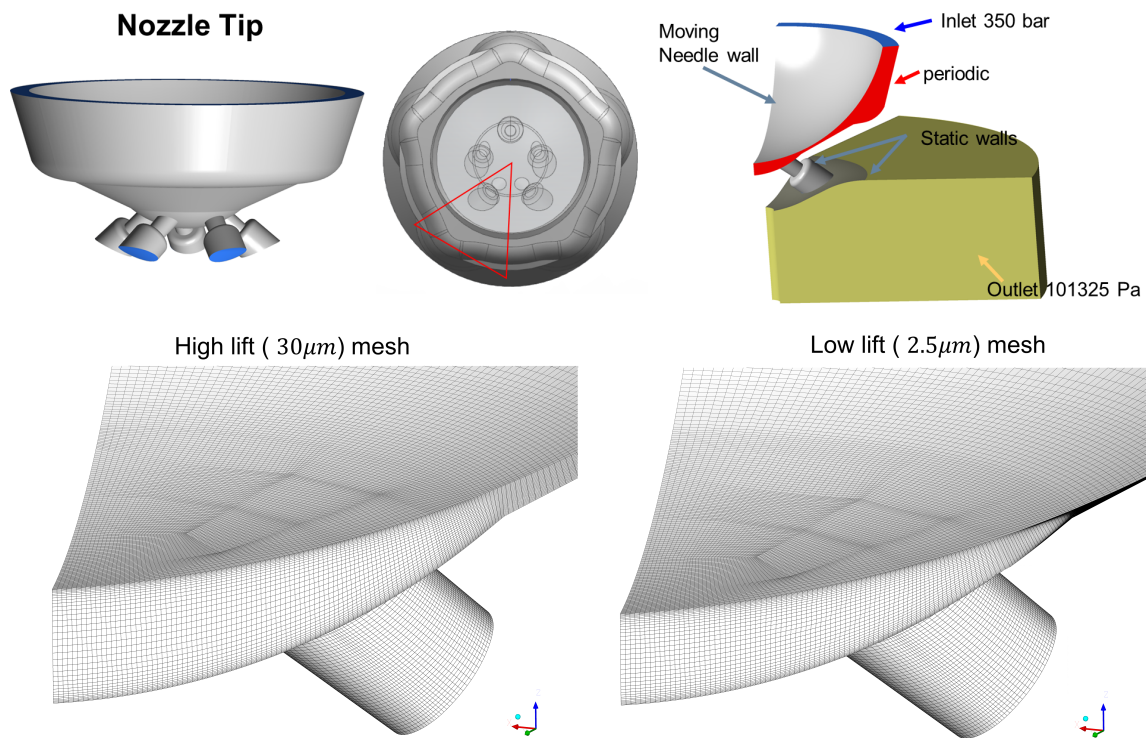

Figure 4.4: Simulation domain and boundary conditions (top) and LES mesh (bottom). Selected 72°sector for sector nozzle geometry simulation highlighted by a red triangle. LES mesh details for both 30μm lift (bottom-left) and low lift (bottom-right)

A node interpolation technique has been chosen for the moving mesh simulation already utilised by the authors in [82, 81]. This requires to generate two topologically identical meshes, one for the highest lift and one for the lowest. Node positions in the mesh are then interpolated between these two extreme values according to an imposed needle lift

63

	LES 72° sector mesh	URANS full nozzle mesh
Mesh count	2.3M	2.7M
# of cells across the hole diameter	105	57
Near wall resolution in the hole [μm]	0.5	1

Table 4.2: Mesh details.

profile. The imposed needle profile is taken from a 1D injector model simulation. Only a ballistic opening and closing are considered with a maximum needle lift of 30 μm and a minimum lift of 2.5 μm. For a detail of the LES meshes see Figure 4.4 bottom. For lifts under 2.5 μm the needle motion is stopped and an interior interface pre-defined at the sealing surface (surface of minimum distance between needle and housing) is changed to a wall separating the upstream part from the downstream region. In reality due to elastic deformation the needle valve seat is a band of finite width instead of a curve but this deformation is not modelled.

The solver selected is the coupled pressure-based solver available in ANSYS Fluent[109]. In terms of the discretization scheme for the momentum equation, the second order upwind is used in the URANS case [110]. In the LES case, a second order bounded central differencing scheme (hybrid between central and second order upwind) was used for momentum discretization; this scheme has small numerical dissipation and sufficient numerical stability for LES simulations [45]. For all simulations a body-force-weighted scheme is employed for pressure interpolation [85] while for the density interpolation a first order upwind scheme [110] is used. Finally, the calculation of the gradients was done using the Least Squares Cell-Based method.

The used solver is pressure-based and therefore the simulation stability is not limited by the acoustic wave propagation time scale. However, temporal resolution for LES requires minimum diffusion for the advection of the turbulent eddies. Therefore, a time step of 5×10^{-9} s is chosen for the LES case, yielding a $CFL \sim 1$ in the spray hole. For the URANS cases, a time step of 5×10^{-8} s is selected. One LES injection cycle and two successive URANS injection cycles have been simulated. The pressure field is initialised with 350 bar above the sealing band and with 101325 Pa downstream. Air volume fraction is set to 1 below the sealing and to zero above in the LES case and the first URANS injection. A second URANS injection is carried out as a continuation of the final flow calculated at the end of the previous injection cycle.

4.3.5 Cavitation erosion indicator

Selection of the most relevant criteria for the evaluation of cavitation erosion is an active research topic. In the current work three parameters have been tested and compared against the experimental observations:

1. The maximum pressure recorded throughout the simulation on the walls, $max(p(t))$, as used by[20, 52] in moving needle Diesel fuel injector nozzle flow simulations.

2. The accumulated total derivative of the pressure field on the walls $\int (\frac{Dp}{Dt})^+ dt$, where $(\frac{Dp}{Dt})^+ = max(\frac{Dp}{Dt}, 0)$, which is similar to the IFM method of [178] and the maximum pressure time derivative recorded on the wall and employed by [160].

3. The accumulated radiated power on the wall due to vapour collapse $\int \frac{De}{Dt} dt$, which was previously used in [176, 180]. Details on the definition of the radiated power due to cavitation collapse are given in the remaining part of this section.

The potential energy available in a spherical bubble of radius R_0 is [181, 180]:

$$E = \frac{4}{3}\pi R_0^3 (p_d - p_v) \, [J] \tag{4.9}$$

where, p_d is the ambient pressure driving the collapse and p_v is the vapour pressure inside the bubble. For a cavity with arbitrary shape the potential energy per unit volume can be approximated by [176, 180]:

$$e = \alpha_{vap}(p_d - p_v) \, [J/m^3] \tag{4.10}$$

The change per unit time of this last parameter is the specific power radiated due to a collapsing vapour cavity and can be expressed as:

$$\frac{De}{Dt} = \frac{D\alpha_{vap}}{Dt}(p_d - p_v) + \alpha_{vap}\frac{Dp_d}{Dt} \, [W/m^3] \tag{4.11}$$

where, $\frac{D()}{Dt} = \frac{\partial ()}{\partial t} + \mathbf{v}\nabla()$. However, as discussed in [180] assuming that only power is radiated when condensation takes place only the first term in Eq. 4.11 contributes to the radiated power and only if the material derivative of α_{vap} is negative. Therefore the radiated power by collapsing cavitation structures can be expressed as:

$$\frac{De}{Dt} = \left(\frac{D\alpha_{vap}}{Dt}\right)^- (p_d - p_v) \, [W/m^3] \tag{4.12}$$

where, $\left(\frac{D\alpha_{vap}}{Dt}\right)^- = min(\frac{D\alpha_{vap}}{Dt}, 0)$. In order to evaluate $\frac{De}{Dt}$, p_d remains to be defined. As pointed out in [180, 170], its definition is not trivial since the driving pressure for a cavity is not a local magnitude but rather the pressure "far away", as in the case of a collapsing bubble. It has been assumed that the pressure driving the reduction of cavitation volume fraction at each computational cell can be estimated by the averaged pressure over the cell faces of all neighbouring computational cells, i.e. $p_d = \frac{\sum_i p_i A_i}{\sum_i A_i}$, where the summations are extended to all the neighbouring cells with pressure p_i and shared face area A_i. Assuming that cavitation damage is caused by cumulative loading of

the nozzle walls, the aforementioned cavitation erosion indicators have been implemented into Fluent through user defined functions.

4.4   Results and discussion

Flow characterisation

The evolution of the void fraction inside the sac volume and the injection holes for both the vapour phase and the air together with the imposed needle profile is shown in Fig. 4.5 for both the LES sector nozzle geometry (solid line) and the URANS simulations (dotted lines). It can be observed that during the needle opening phase, air is pushed out of the sac volume due to its filling with fuel and that vapour is created.
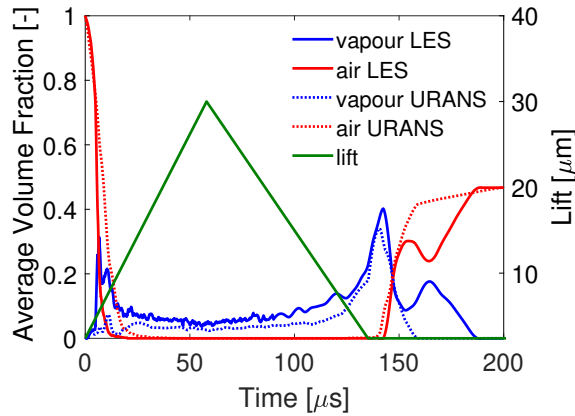

Figure 4.5: Volume fraction of air (red) and vapour (blue) inside the sac and orifices against time. Needle lift against time (green). LES sector nozzle geometry (left) and URANS full nozzle geometry 1st injection cycle (right).

A time sequence of the evolution of the liquid volume fraction field and the velocity field on a plane normal to the orifice and the 3D iso-surfaces of vapour volume fraction 10% (black) and air volume fraction 50% (magenta) are shown in Fig. 4.6 for both the LES sector nozzle (top) and the URANS simulation (bottom). High speed liquid coming from the needle seat area ($t = 2.5\mu s$) flows towards the sac volume center and recirculates ($t = 5\mu s$). This recirculation results in low pressure regions and the creation of vapour. Cavitation is also present in the small gap between the housing and the needle valve, where the flow is throttled. The LES simulation presents higher peak velocities compared to the URANS simulation and therefore the amount of vapour created due to the recirculation in the sac volume is also higher (see Fig. 4.5). The liquid is progressively directed towards the injection holes pushing the air out of the injector ($t = 10\mu s$). In the case of the LES the flow in the sac volume becomes a complex liquid, vapour and air mixture with finer structures than in the URANS case.
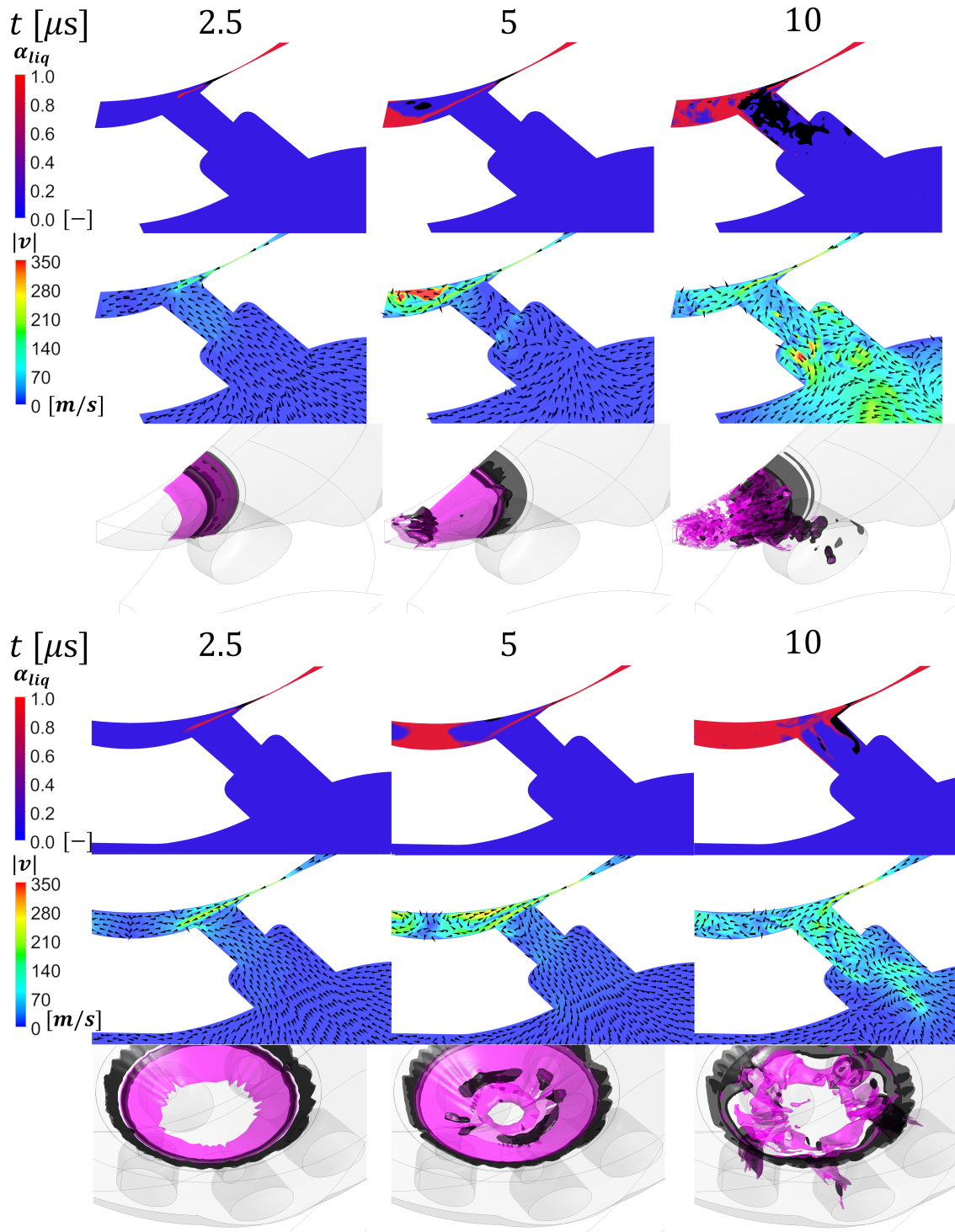
66

Figure 4.6: Time sequence for the start of injection. LES results (top) URANS results (bottom). For each modelling approach: liquid volume fraction in a plane perpendicular to the orifice with regions of $p < p_{satL}$ and $\alpha_{vap} > 0$ in black (top), velocity magnitude field and velocity vectors in the same plane (middle) and 3D iso-surfaces of vapour volume fraction 10% (black) and air volume fraction 50% (magenta) (bottom).
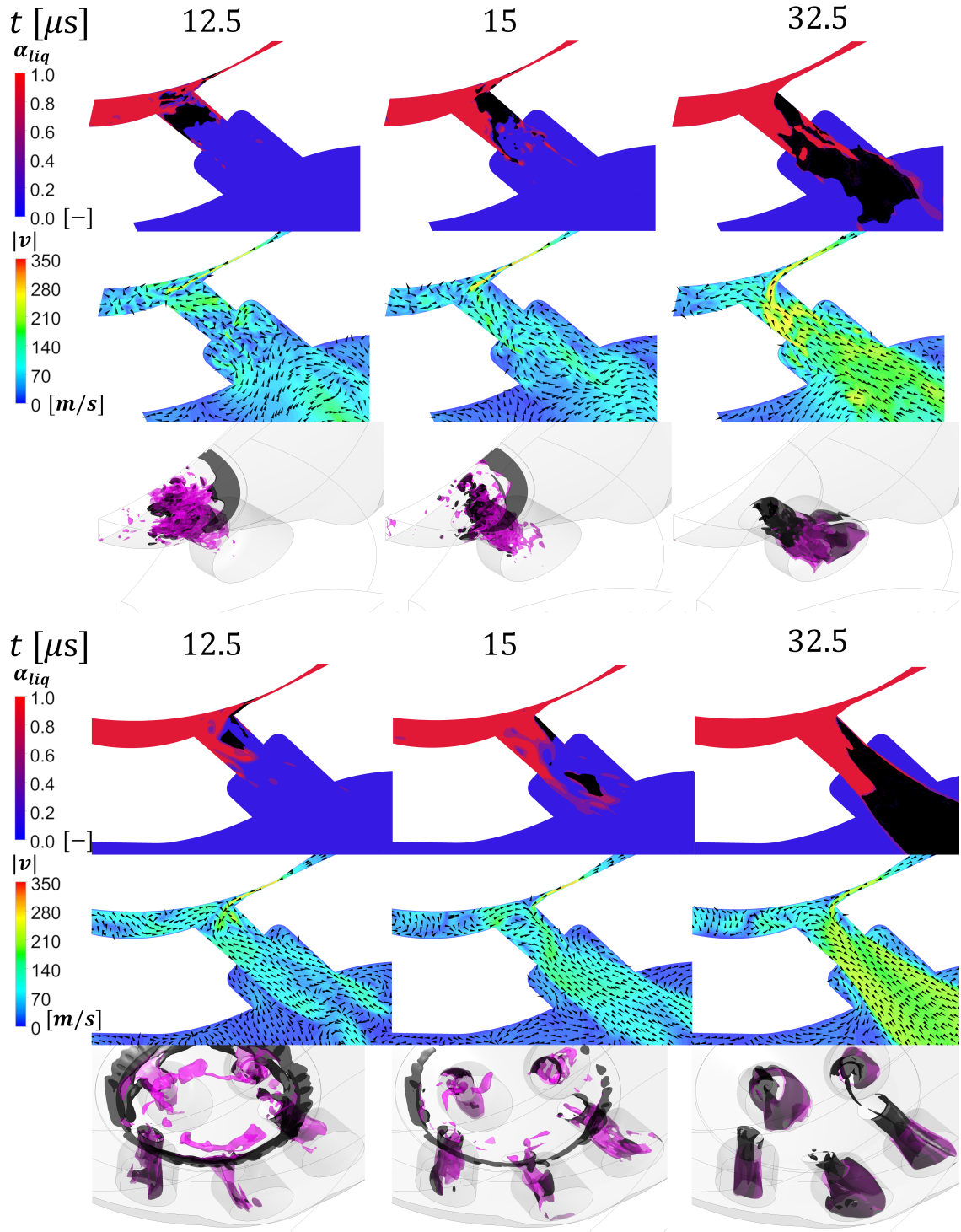
Figure 4.7: Time sequence for the needle opening phase. LES results (top) URANS results (bottom). For each modelling approach: liquid volume fraction in a plane perpendicular to the orifice with regions of $p < p_{satL}$ and $\alpha_{vap} > 0$ in black (top), velocity magnitude field and velocity vectors in the same plane (middle) and 3D iso-surfaces of vapour volume fraction 10% (black) and air volume fraction 50% (magenta) (bottom).

A time sequence of the flow as it further develops during the needle valve opening

for both simulations is presented in Fig. 4.7. As the needle lift increases, the cavitation present in the small gap at the sac entry recedes. The air in the sac volume is evacuated and the flow enters the injection hole first from the sac side, until the air is purged from the sac volume ($t = 12.5\mu s$) and then from the seat side ($t = 15\mu s$). Eventually, cavitation is mostly constrained to the injection holes ($t = 32.5\mu s$). This cavitation arises due to flow separation at the injection hole inlet where a cavitating shear layers is formed ($t = 15\mu s$ and $t = 32.5\mu s$).

The full nozzle geometry configuration results in hole-to-hole interactions leading to vortices connecting adjacent holes, which can be sufficiently strong to cavitate, see Fig.4.8 where the vortices represented by the Q-criterion; the 10% vapour volume fraction are simultaneously depicted for the full nozzle URANS geometry at $t = 32.5\mu s$. For the remaining needle opening phase, cavitation remains constrained to the holes until the needle closing phase.

Figure 4.8: URANS full nozzle hole-to-hole interaction. Vortex structures depicted by Q-criterion iso-surface (gold) and 10% vapour volume fraction iso-surface black in the sac volume and injection holes at $t = 32.5\mu s$.

In Fig. 4.9 the snapshots of the flow just before and after the needle valve closing are shown for both simulations. Shortly before the needle valve closure ($t = 135\mu s$), cavitation in the small gap between the needle and the housing wall reappears. Just after the needle closing, a ring of vapour is created which then collapses towards sealing ($t = 137.5\mu s$ and $t = 140\mu s$). Additionally, due to the relative high momentum in the injection hole, the sac pressure drops and the fuel cavitates causing big vapour bubbles to appear inside the nozzle's sac volume.
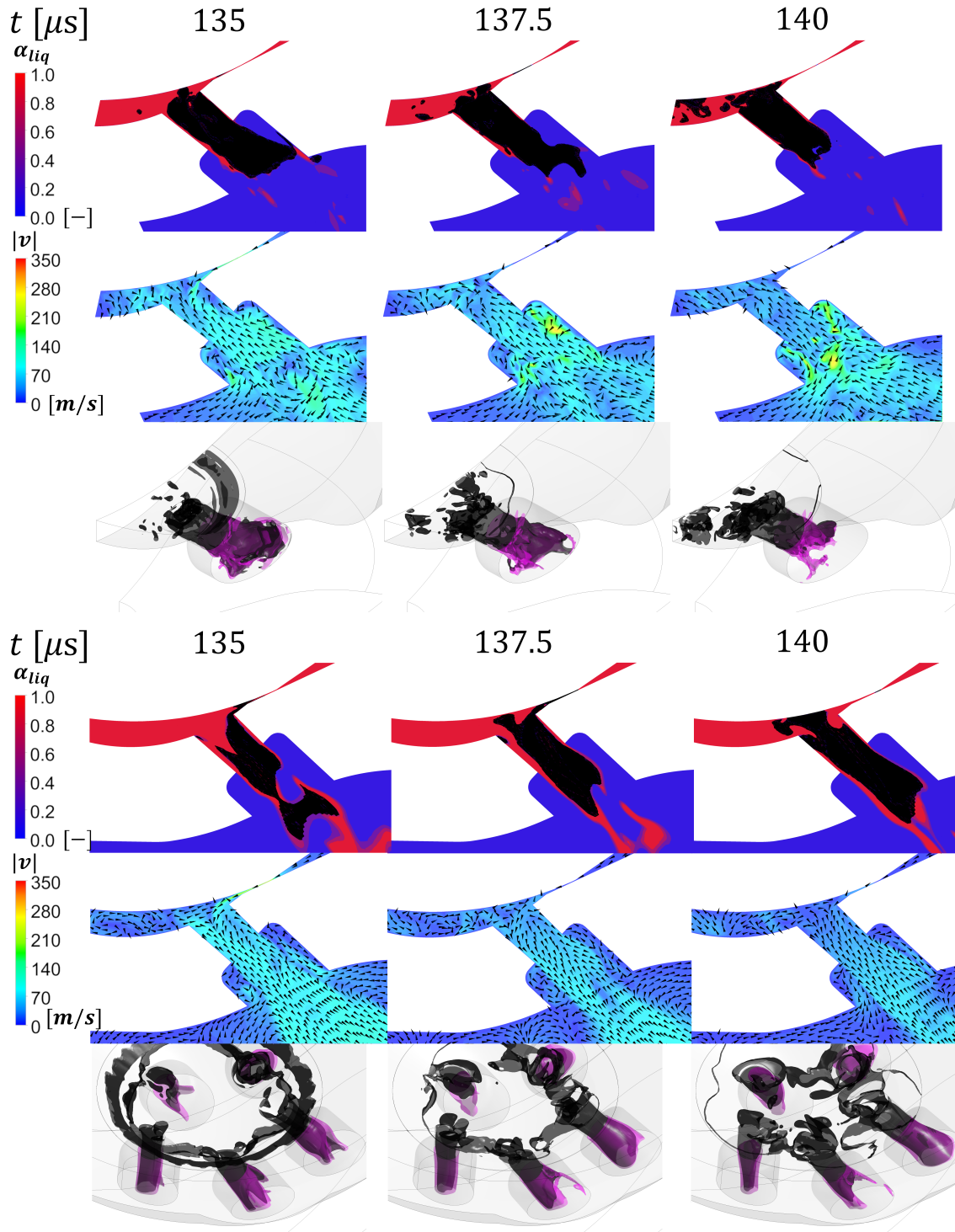
Figure 4.9: Time sequence for the needle closing phase. LES results (top) URANS results (bottom). For each modelling approach: liquid volume fraction in a plane perpendicular to the orifice with regions of $p < p_{satL}$ and $\alpha_{vap} > 0$ in black (top), velocity magnitude field and velocity vectors in the same plane (middle) and 3D iso-surfaces of vapour volume fraction 10% (black) and air volume fraction 50% (magenta) (bottom).

The final evolution of the flow is shown in Fig. 4.10. When the flow in the injection

hole sufficiently decelerates, the vapour in the injection hole starts to collapse entraining air into the injector ($t = 145\mu s$ and $t = 150\mu s$). The LES and URANS simulations present differences for the final collapse phase of the vapour. The LES sector model predicts a vapour bubble in the sac volume to be perfectly centered in the injector axis. This yields a fast focused collapse of the vapour in the sac center ($t = 145\mu s$ to $t = 150\mu s$), which is followed by a rebound ($t = 160\mu s$) before the vapour finally collapses and vanishes ($t = 190\mu s$), see also Fig. 4.5. On the other hand, the URANS full nozzle model predicts an asymmetric structure which presents a less focused collapse with no rebound.
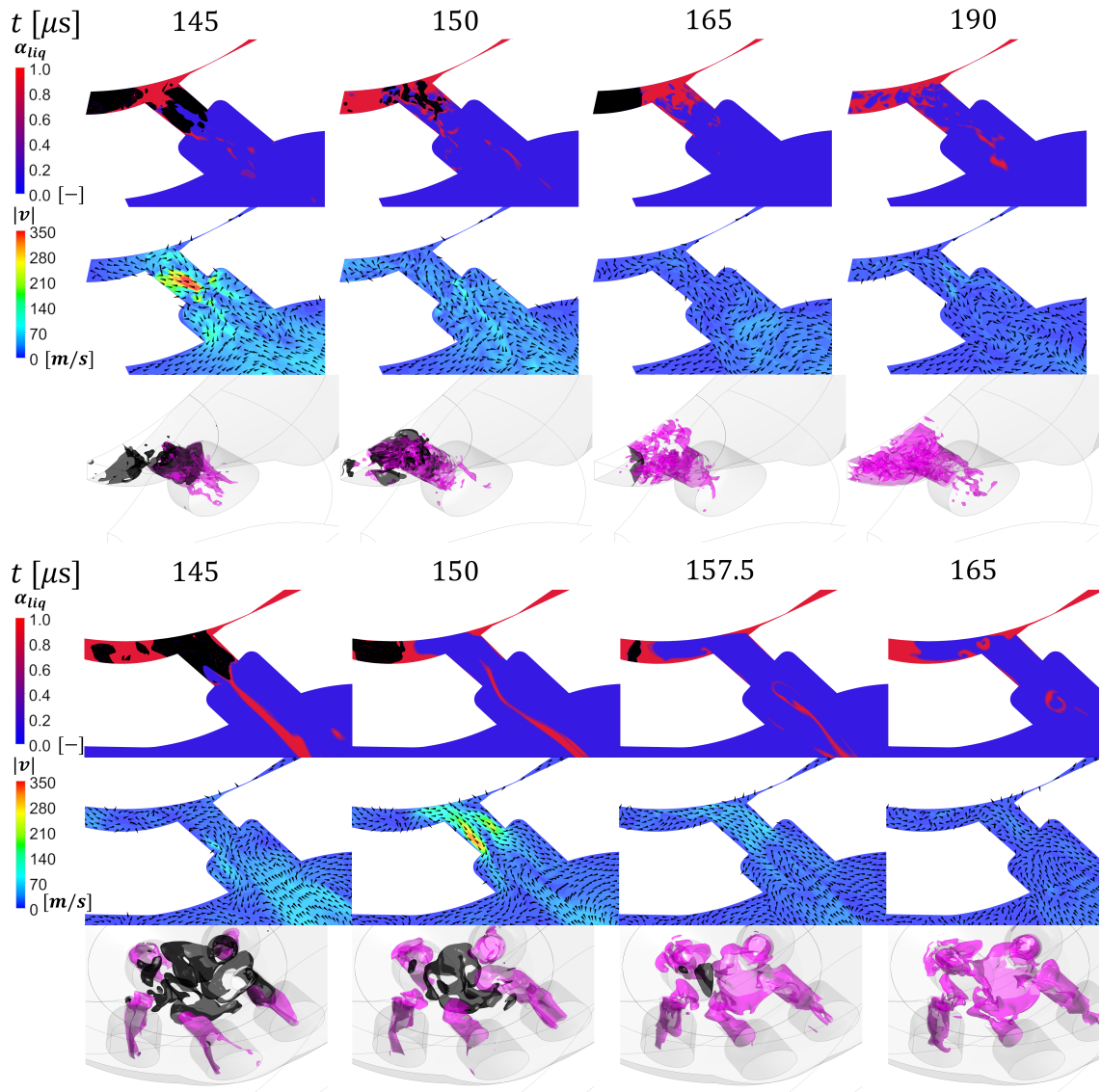

Figure 4.10: Time sequence for the flow after the needle closure. LES reuslts (top) URANS results (bottom). For each modelling approach: liquid volume fraction in a plane perpendicular to the orifice with regions of $p < p_{satL}$ and $\alpha_{vap} > 0$ in black (top), velocity magnitude field and velocity vectors in the same plane (middle) and 3D iso-surfaces of vapour volume fraction 10% (black) and air volume fraction 50% (magenta) (bottom).

Regardless of the modelling approach, vapour collapse in the sac volume center is predicted and a similar fraction of the sac volume and injection hole is occupied by air at the end of the injection. This suggests that the sac volume is not full of air between injections and that some residual liquid is present. Therefore, a second URANS full nozzle simulation was carried out starting from the results $65\mu s$ after needle closure of the first injection. Fig. 4.11 depicts the evolution of the volume fraction of the sac volume and injection holes filled with air (red) and vapour (blue) for both injections against time. Flow visualisations for the second URANS opening are shown in Fig. 4.12. During the second needle valve opening, the residual liquid in the sac volume cavitates due to the fast needle opening ($t = 2.5\mu s$ and $t = 5\mu s$); this causes a greater amount of vapour to be created compared to the first injection, as seen in Fig. 4.11. Moreover, during the second injection the residual liquid existing in the sac makes the high speed liquid coming from the needle valve seat to penetrate less into the sac volume before it starts to recirculate towards the injection holes ($t = 5\mu s$ and $t = 10\mu s$). $20\mu s$ after the start of injection, no major differences between the first and second injections are observed; the same phenomena during the needle closing and after the injection are predicted.
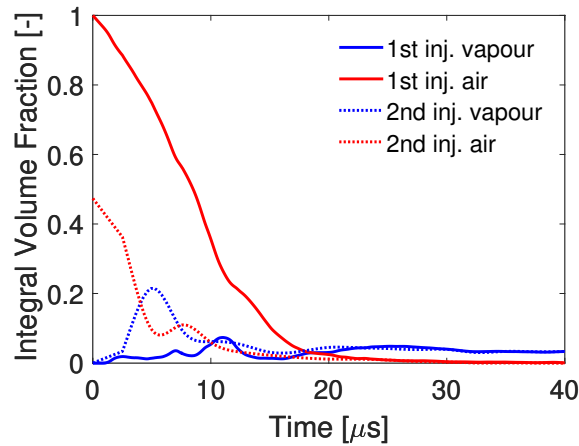

Figure 4.11: Volume fraction of air (red) and vapour (blue) inside the sac and orifices against time for the first (solid) and second (dotted) URANS injection.
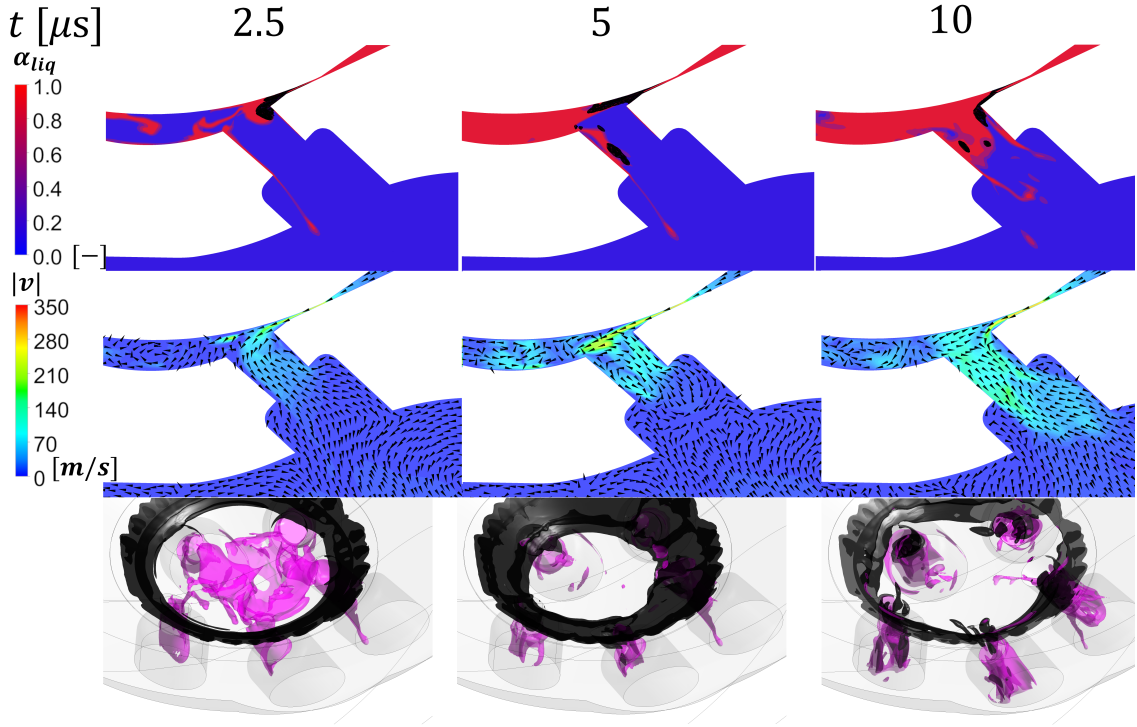
Figure 4.12: Flow visualisations for the opening of the second URANS injection. Liquid volume fraction in a plane perpendicular to the orifice with regions of $p < p_{satL}$ and $\alpha_{vap} > 0$ in black (top), velocity magnitude field and velocity vectors in the same plane (middle) and 3D iso-surfaces of vapour volume fraction 10% (black) and air volume fraction 50% (magenta) (bottom).

Assessment of cavitation erosion prone locations

In this section the results obtained for the cavitation erosion indicators previously described in section 4.3.5 are presented for both the LES sector nozzle geometry simulation and the second URANS event. Fig. 4.13 shows the maximum pressure recorded throughout the simulation ($max(p(t))$), $\int(Dp/Dt)^+dt$, and $\int(De/Dt)dt$ on the injector wall. In the LES case $max(p(t))$ returns high values in the area where the flow recirculates during the injector opening, inside the injection hole, in the region upstream of the injection hole and in the injector axis region. The maximum pressures detected are of the order of $\sim 1500bar$ in the needle sealing area. In the case of URANS, $max(p(t))$ does not provide sufficient contrast to identify any erosion prone location. For the LES case $\int(Dp/Dt)^+dt$, returns high values at the injection hole inlet and the injector axis region, while the URANS simulation returns high values at the inlets of the injection holes and between the two holes which were identified to be strongly interacting with cavitating vortex strings; there is also a hint of high values towards the needle valve sealing area. The final indicator, $\int(De/Dt)dt$, presents high values in the LES case at the injection hole inlet, sac volume entry corner, needle valve sealing band region and sac volume centre re-

gion. In the URANS simulation the same areas of high $\int (De/Dt)dt$ are identified but the sac volume center region shows a more dispersed pattern. Overall, the indicators point at high cavitation erosion risk in the needle valve sealing band, sac volume entry corner, hole entry and sac volume centre regions, which were the areas that presented wear according to the durability tests (see Fig. 4.1).

In the LES simulation $\int (Dp/Dt)^+ dt$, presents the least areas with agreement with the hardware test, while $max(p(t))$ and $\int (De/Dt)dt$ identify the same erosion risk areas. In the URANS simulation $max(p(t))$ presents no agreement with the hardware test, $\int (Dp/Dt)^+ dt$ shows moderate agreement in the orifice inlets and $\int (De/Dt)dt$ identifies as erosion risk areas the regions that showed damage in the hardware tests. Tables 4.3 and 4.4 show a summary of the correlations found between the indicators and the hardware tests for the LES sector nozzle modelling and the URANS full nozzle modelling, respectively.

It has to be noticed that $\int (Dp/Dt)^+ dt$ accounts for all changes in pressure, not only those coming from vapour collapse; regions with unstable flow can present high pressure derivatives that may not always be attributed to the collapse of vapour structures. On the other hand, De/Dt implicitly accounts exclusively for the pressure derivatives arising from cavitation collapse,

$$\frac{De}{Dt} = (p_d - p_v)\left(\frac{D\alpha_{vap}}{Dt}\right)^- = -\frac{p_d - p_v}{\rho_{satL} - \rho_{satV}}\left(\frac{D\rho}{Dt}\right)^+ = -\frac{p_d - p_v}{\rho_{satL} - \rho_{satV}}\frac{1}{c^2}\left(\frac{Dp}{Dt}\right)^+$$

and therefore it is expected to present higher correlation with the experimentally observed damage. Regarding $max(p(t))$, the work of [182] shows that the cavitation collapse pressure is inversely proportional to the cell size at the collapse centre but that the location of collapse events is not affected by grid resolution. Concerning the URANS modelling approach employed in this study, the reduced grid resolution and higher effective flow viscosity result in pressure peaks that are indistinguishable from the injection pressure but with the same cavitation locations than the more finely resolved LES. Eventhough in LES the choice of indicator is less important, since the flow and pressure is better resolved, in general $\int (De/Dt)dt$ seems to be the most appropriate indicator as it depends on the cavitation locations which are less affected by grid resolution and it implicitly accounts for the pressure variations induced by cavitation collapse
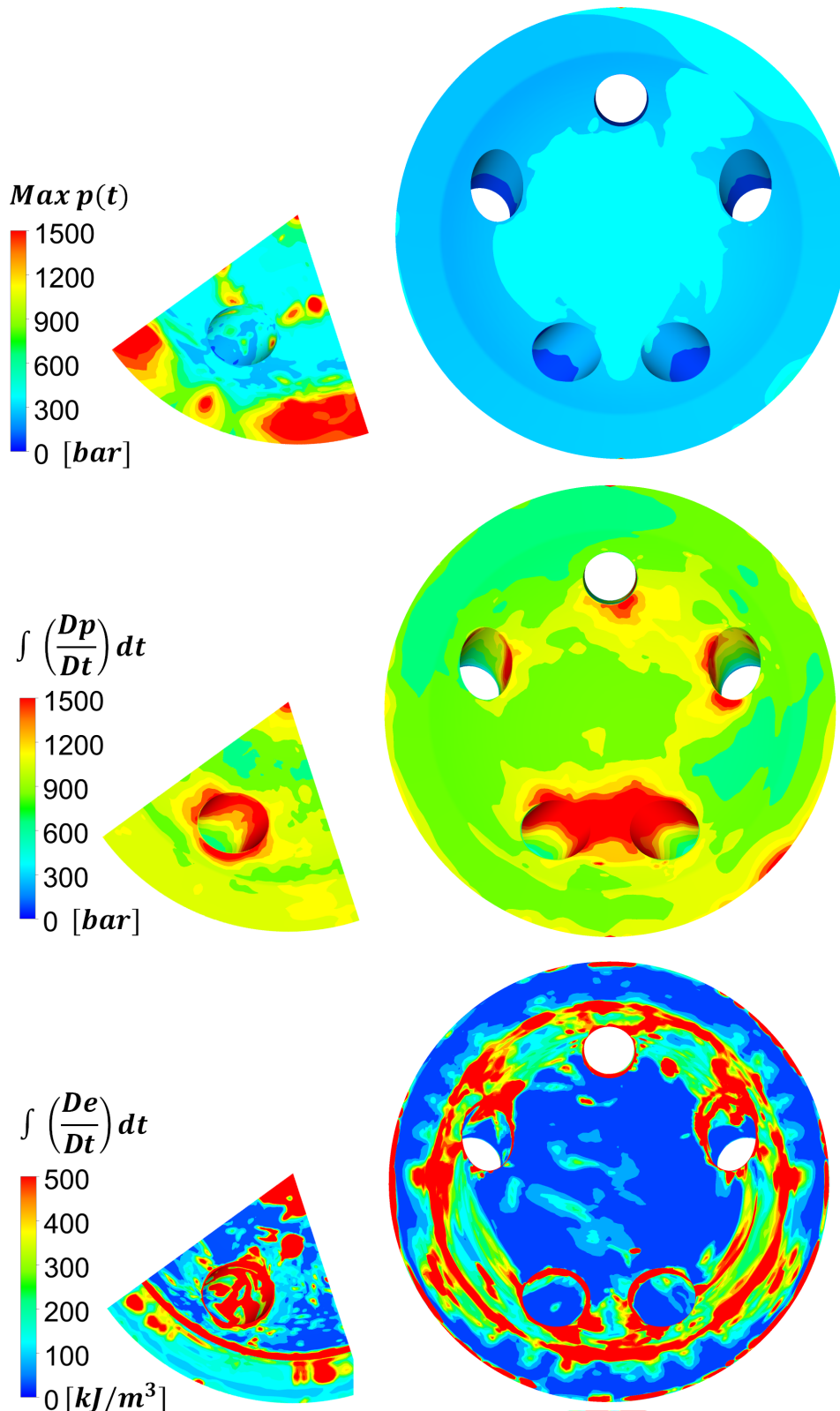
Figure 4.13: Cavitation erosion indicators on the injector wet wall for the LES sector nozzle geometry (left) and the URANS full nozzle (right). Only the region downstream of the sealing is shown. Maximum pressure recorded throughout the simulation (top), $\int (Dp/Dt)dt$ (middle) and $\int (De/Dt)dt$ (bottom) on the injector wet wall.

Region	Parameter		
	$max(p(t))$	$\int(Dp/Dt)dt$	$\int(De/Dt)dt$
Sealing band	Good	Poor	Good
Sac entry corner	Good	Poor	Good
Injection hole inlet	Good	Good	Good
Sac volume center	Good	Good	Good

Table 4.3: LES sector nozzle modelling. Correlation to hardware tests of the cavitation erosion indicators evaluated.

Region	Parameter		
	$max(p(t))$	$\int(Dp/Dt)dt$	$\int(De/Dt)dt$
Sealing band	Poor	Some	Good
Sac entry corner	Poor	Poor	Good
Injection hole inlet	Poor	Good	Good
Sac volume center	Poor	Good	Good

Table 4.4: URANS full nozzle modelling. Correlation to hardware tests of the cavitation erosion indicators evaluated.

Erosion development process over one injection cycle

Next, further insight about how the damage develops during an injection event is given based on the results for the second URANS injection as it is deemed to have more realistic initialisation than the first injection event. Fig.4.14 presents how the erosion at the sac volume inlet corner arises at the beginning of the injection. The 10% fuel vapour volume fraction iso-surface and the nozzle wall coloured by the value of $\int_{t=0}^{t=t_0}(De/Dt)dt$ are shown for two instants during the needle valve opening phase. When cavitation at the sac volume entry disappears, radiated power due to cavitation accumulates in the sac entry area. A similar erosion pattern was also observed experimentally in the case of Diesel injection in [138].
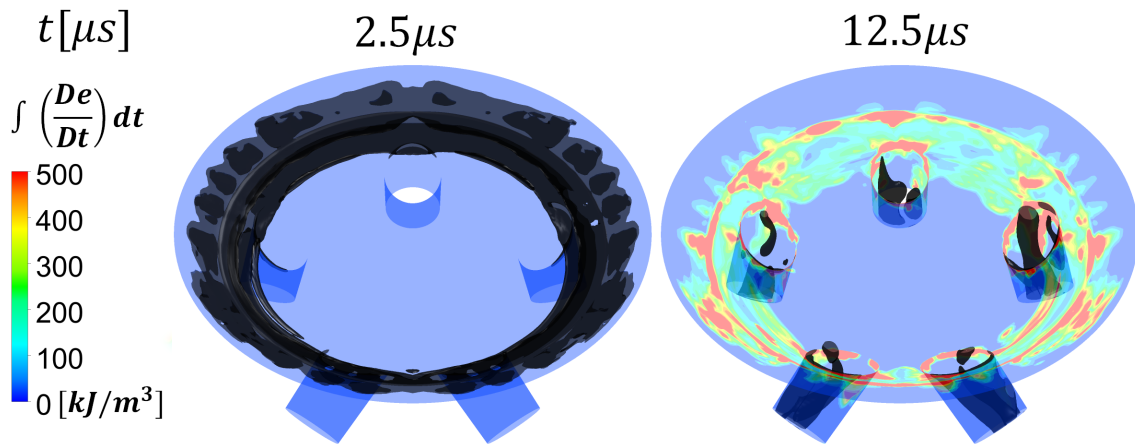
Figure 4.14: Mechanism for sac volume entry wear. 10% fuel vapour volume fraction iso-surface (black) and injector nozzle wall coloured by $\int_{t=0}^{t=t_0}(De/Dt)dt$.

Further evidence of how the sealing band damage is occurs is depicted in Fig.4.15. This wear is caused by the ring of vapour created just after the needle closing. This structure collapses towards the sealing band and radiated power accumulates in the sealing band region

Figure 4.15: Mechanism for sealing band wear. 10% fuel vapour volume fraction iso-surface (black) and injector nozzle wall coloured by $\int_{t=0}^{t=t_0}(De/Dt)dt$.

Finally, Fig.4.16 shows the mechanism behind the sac volume centre wear. It can be attributed to repeated loading of the sac volume wall over many injection cycles due to the asymmetric collapsing vapour structure predicted at the end of the injection.
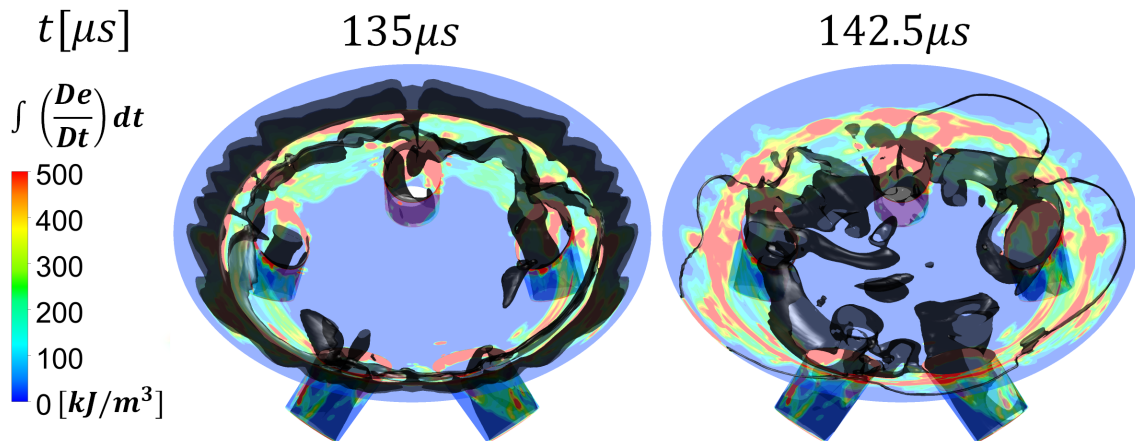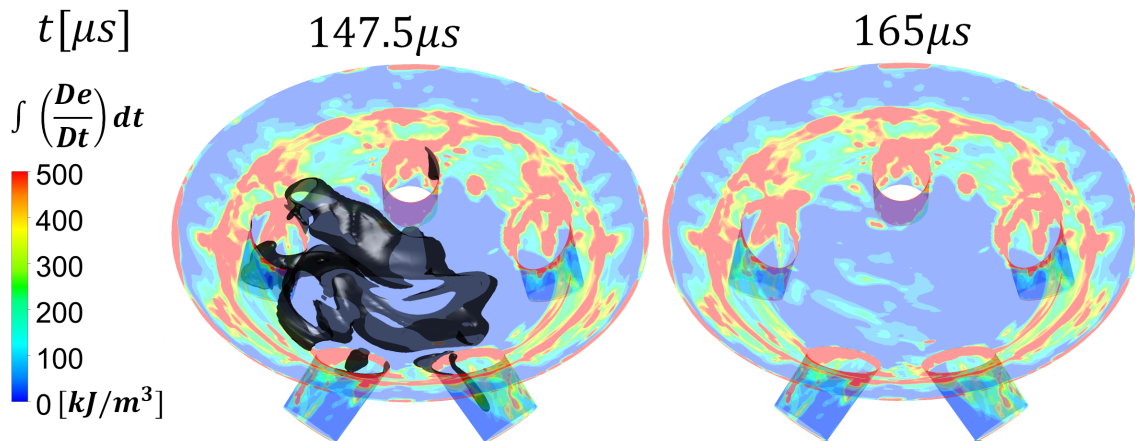
Figure 4.16: Mechanism for sac volume center wear. 10% fuel vapour volume fraction iso-surface (black) and injector nozzle wall coloured by $\int_{t=0}^{t=t_0}(De/Dt)dt$.

4.5 Conclusions

An investigation on the modelling and prediction of cavitation erosion sites in GDi injectors operated with E100 has been presented. Erosion sites were identified after 400 million cycles hardware durability tests in production 5-hole GDi injectors; erosion has been observed for all injectors tested at the sac volume center, sac volume entry corner, injection hole inlet and at needle seat contact band

A barotropic cavitation model has been utilised to predict the collapse of vapour structures during the opening and closing of the injector's needle valve. This cavitation model has been verified against the theoretical Rayleigh-Plesset solution for the collapse of a vapour bubble. LES approach has been used to simulate an injection cycle, but due to its computational cost its use was restricted to the modelling of a 72° sector. The reduced mesh and time step requirements for the URANS turbulence modelling approach allowed for the use of the full nozzle geometry which accounts for the hole-to-hole interactions.

When the sac volume was assumed to be filled with air at the start of the needle valve movement, both simulation approaches predict high speed liquid flowing from the needle seat area into the sac volume, which recirculates creating cavitation. Cavitation is also created in the small gap between the sac volume entry, the injector housing wall and the needle valve, downstream of the needle seat. The predicted peak velocities during the flow recirculation are higher in the LES and result in higher amount of vapour predicted. The morphology of the flow in the sac volume at the start of the injection is a more finely mixed foam in the LES approach compared to URANS. As the needle valve lift increases, cavitation in the sac volume disappears, the air assumed to be present inside the sac volume is evacuated and cavitation moves into the injection holes. Both simulation approaches predict flow separation at the injection hole inlet and cavitating shear layers.

On the other hand, the full geometry URANS approach predicts strong vortical interaction between adjacent holes, resulting in connecting cavitating vortex strings.

During the injector needle closing phase, cavitation reappears in the small gap created downstream of the needle seat area. Just after the needle closure, a ring of vapour is created, which collapses towards the needle seat. Simultaneously, since the flow still has momentum while exiting the nozzle holes, the flow is throttled at the needle seat and vapour is created in the sac volume. When the pressure progressively balances, air is entrained from the sorrounding ambient and vapour in the sac volume collapses. In the sector nozzle LES, the vapour created in the sac forms a structure centered in the injector axis, which subsequently collapses towards the injector axis. The focusing towards the injector axis results in a strong collapse followed by a rebound and a second collapse. In the full nozzle URANS case the vapour structure created in the sac is asymmetric resulting in a less focoused collapse with no rebound. At the end of injection, the sac volume is filled with a mixture of air and liquid.

The URANS approach allowed to explore the impact of the state of the sac volume between injections in terms of cavitation and flow development. It was found that the remaining liquid in the sac volume is prone to cavitate due to the sudden valve opening resulting in higher amounts of vapour during the injector opening but that the remaining air causes the fuel recirculation to happen further upstream.

Finally three cavitation erosion parameters suggested in the literature, namely $max(p(t))$, $\int (Dp/Dt)^+ dt$ and $\int (De/Dt)dt$ were evaluated. $\int (Dp/Dt)^+ dt$ shows the poorest correlation to the hardware damage patterns of all three indicators whichever the modelling approach since it accounts for all pressure derivatives regardless of them being induced by cavitation or not. The $max(p(t))$ indicator shows good correlation in the LES case due to the fine resolution employed but its performance when used with URANS is poor. Lastly, $\int (De/Dt)dt$, which can be thought of the energy per unit volume the wall absorbs correlates well with the erosion prone areas for both LES and URANS approaches as it mostly depends on the location of cavitation which did not change significantly between approaches.

4.6 Critical review: Mesh resolution assessment for GDi nozzle flow URANS simulations

In the case of URANS turbulence modelling (unlike for LES, as explained previously) there is no physical way of determining which mesh resolution is suitable. However the prediction of the mass flow rate is a key CFD requirement in the industry as well as a simple integral assessment on the performance of the simulation methodology. A successful simulation framework in the fuel injection industry requires in the first place to be able to accurately

predict the design's mass flow rate and the mass distribution per hole. Any further research can then rely on the foundation of the mass flow rate being correctly predicted. Part of the content of the mesh and cavitation model sensitivity section was carried out by Kacper Stasiuk (Trainee at Delphi Technologies) under the author's supervision. The simulation methodology and setup for prediction of mass flow rate was initiated and developed by the author but some simulations where carried out by other Delphi Technologies colleagues.

4.6.1 Mesh quality criteria and mass flow rate sensitivity to mesh resolution in URANS simulations

General meshing best practices include to reduce volume change between neighbouring, keeping minimum angles to values as high as possible, reduce cell skewness as much as possible and a 3D determinant (normalized triple product of the vectors starting from each cell node; measure of how close to a perfect cube the cell is) as high as possible. All these factors help reducing the global error by reducing the discretization error and model errors [151]. Additionally, even if the $k - \omega \, SST$ model is implemented in Fluent following a y^+ insensitive approach (including an automatic switch between wall functions and resolved stress), boundary layers should be properly resolved by having the first cell correspond to a y^+ value that is inside the viscous sub-layer [85]. In practice at Delphi Technologies the general mesh quality criteria followed for fuel injector simulations are presented in Table 4.5. These criteria have proven to be good practical guidelines that lead to robust simulations.

Quality criteria	Value
Maximum volume change	< 8
Minimum angle	$> 24^o$
Minimum determinant	> 0.5
Boundary layer resolution	10-15 elements with 1.1 cell growth ratio

Table 4.5: Mesh quality requirements followed by the author.

To asses the sensitivity of the mass flow rate to the mesh resolution a URANS simulations were carried out for three different grids for a 60° nozzle sector geometry with $160 \mu m$ injection hole diameter and an inlet pressure of $350 bar$. A summary of the mesh parameters and the impact on the flow is presented in Table 4.6. Although there is 2.89% difference in the predicted flow rate between the coarse and fine mesh, the results show that the medium resolution is good enough for obtaining grid independent mass flow rate and shows that further refinement of the boundaries and the bulk flow does not bring impact to the results. An equivalent mesh resolution was employed for the URANS simulations in the paper included in the chapter.

	Coarse	Medium	Fine
Mesh size [elements $\times 10^6$]	0.54	0.84	1.23
y^+ in spray hole	~ 40	~ 15	~ 5
Wall spacing in spray hole [μm]	2	0.6	0.3
# of cells across the injection hole diameter	45	60	80
Mass flow rate [mg/ms]	2.887	2.972	2.973

Table 4.6: Flow rate sensitivity to the mesh resolution.

4.6.2 Mass flow rate sensitivity to the cavitation model in GDi injectors. Case study.

In this section, the Zwart-Gerber-Belamri (ZGB) cavitation model and the homogeneous polynomial barotropic cavitation model are compared in a simulation of the flow in a GDi injector nozzle tip. The inlet pressure is set to $101bar$ and the outlet pressure to $1bar$. The simulations are performed with the URANS approach. The injector tip (which we will call Nozzle A) is a production nozzle with a mean hole outlet diameter of $136\mu m$. The working fluid is N-heptane injected at 20^oC. The ZGB model was ran with a time step of $2.5 \times 10^{-7}s$ while the barotropic model requires a value of $5 \times 10^{-8}s$ to maintain the simulation stability. The simulations predicts an average mass flow rate of $6.72g/s$ for the ZGB model and $6.71g/s$ for the barotropic model, whereas the experimental flow rate is $6.44g/s$. This is s 4.2% difference between the experimental value and the two phase model and 4% difference with the barotropic model. For convenience during CFD simulations the pressure at the boundary is taken as the rail pressure. Nevertheless, previous internal work at Delphi Technologies shows a 4% pressure drop from the fuel rail to the injector tip where the pressure boundary condition is imposed ($\frac{p_{rail}-p_{tip}}{p_{rail}} \sim 0.04$). Most of this pressure drop arises at the orifice present at the entrance of the injector. This restriction has the purpose of damping pressure waves and oscillations to improve the injector flow metering control. For incompressible flow in the Bernoulli regime the mass flow rate through an orifice scales as $\dot{m} \sim \sqrt{\Delta p}$, where Δp is the pressure difference between rail and the atmosphere. It then follows that a 4% difference in Δp leads to a 2% impact on the flow. Therefore the total error compared to the measured value of the flow is 2.2% for the ZGB model and 2% for the barotropic model, and the impact of the cavitation model on the flow is about 0.15%.

In Fig. 4.17 (top) a representative time instance of the 10% volume fraction iso-surface inside the nozzle is shown; both models show a similar vortex flow pattern as revealed by the cavitation strings. The cavitation produced by the flow separation at the hole inlets is also similar. However the liquid volume fraction contours at the hole outlet (Fig. 4.17 - bottom) reveal that the cavitation clouds are filled with vapour to a greater extent in the case of the barotropic model. This can be attributed to the insufficient value of the mass

transfer coefficients. Indeed, [43], suggest to use a value of $F \sim 10^8 \, m^{-1}$ in the ZGB "to maintain numerical stability and prevent liquid tension from becoming unphysical"; F is equal to $\frac{3F_{vap}\alpha_{nuc}}{R}$ in the case of evaporation and to $\frac{3F_{cond}}{R}$ in the case of condensation, see 2.7. Compared to this suggestion, the standard ZGB cavitation model provides low values for both evaporation ($\frac{3F_{vap}\alpha_{nuc}}{R} = \frac{3 \times 50 \times 5 \times 10^{-4}}{10^{-6}} = 7.5 \times 10^4 m^{-1}$) and condensation ($\frac{3F_{cond}}{R} = \frac{3 \times 0.01}{10^{-6}} = 3 \times 10^4 m^{-1}$) coefficients. However for this particular problem, this fact does not impact the prediction of the nozzle mass flow rate and this value is driven by the liquid density. This is an advantage for the prediction of mass flow rate since one does not need to rely on the barotropic model which requires at least 5 times smaller time step and therefore at least 5 times more simulation time. However, if the collapse speed of vapour clouds are relevant the barotropic model is the suitable choice [33]. Although for this last case, in principle increasing the mass transfer coefficients would also be a possible solution, when using 3-phase modelling the commercial CFD code predicts spurious sources of air. The inability to investigate this due to the commercial nature of the code lead to the barotropic model be the model of choice when the collapse speed of vapour clouds is relevant; in particular when cavitation erosion prone areas are of interest.
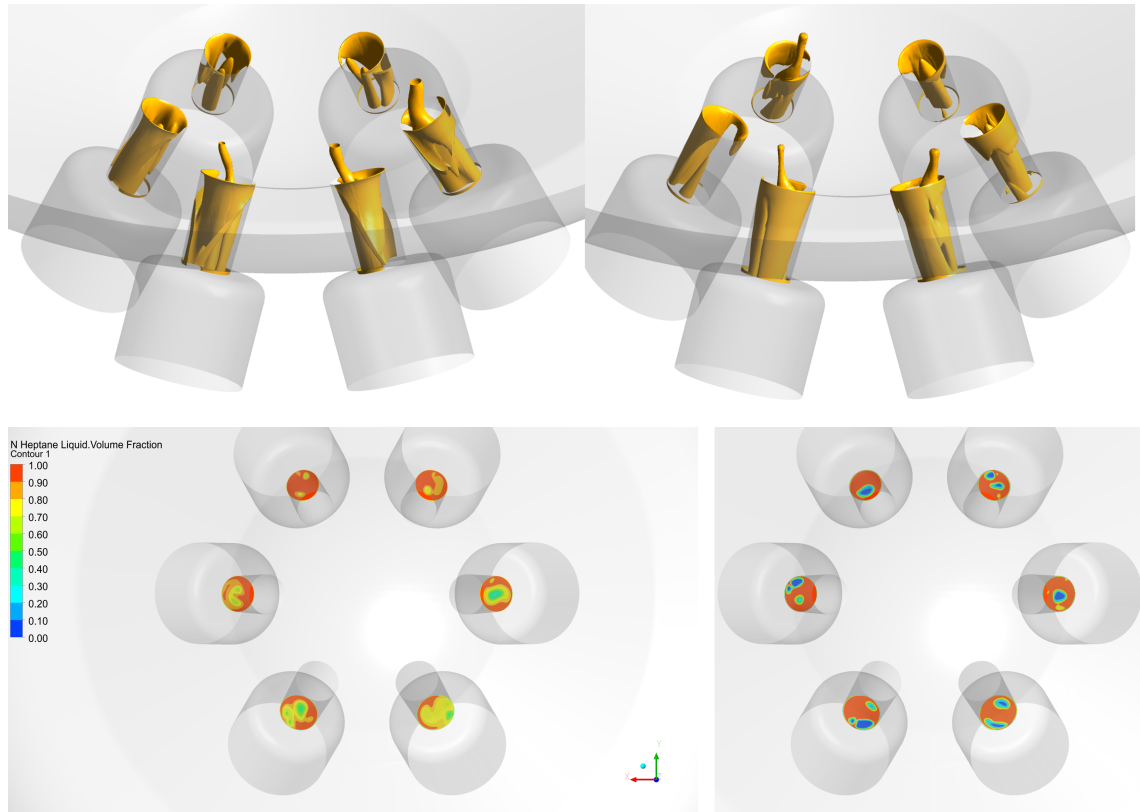

Figure 4.17: Cavitation model impact on flow for a representative time instant. ZGB model (left), barotropic model (right). Vapour volume fraction 10% iso-surface (top) and liquid volume fraction contours at injector hole outlet (bototm)

4.6.3 Mass Flow rate prediction in GDi injectors

Next the URANS simulation methodology was also tested in the prediction of the mass flow rate for 6 different multi-hole GDi nozzles. The nozzles were tested at different injection pressures ranging from $100bar$ to $350bar$ and with back pressures ranging from $1bar$ to $10bar$ and with two different fuels (N-heptane and Stoddard). The fuel temperature was kept at 20^oC. The simulations are performed with the URANS approach and the ZGB cavitation model with a time step of $2.5 \times 10^{-7}s$. The tested nozzles have between 5 and 6 holes hand were both central and side mounted. Table 4.7 shows a summary of the results. For each tested nozzle the spray pattern from the patternation test is also depicted; this is the accumulated mass after an injection in an hexacell mesh at a certain vertical distance $(40mm)$ of the injector tip and provides the spray targeting and mass distribution of each spray plume [74]. The spray pattern is provided here as a reference on the injector type and hole number, from the spray layout it follows that Nozzles A and E1 are central mounted while the rest are side mounted. Overall the the predicted mass flow rate is less than $< \pm 3.2\%$ away from the measurement, with a mean error of 1.49% across all the tested nozzles. It is suspected that further improvements in the accuracy can be achieved by taking into account manufacturing tolerances and using measured nozzle geometries instead of nominal design geometries; however such study was not carried out as part of this work and the accuracy in terms of flow prediction is considered satisfactory to meet industrial needs.
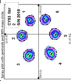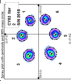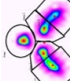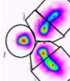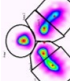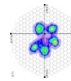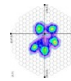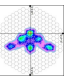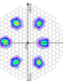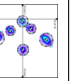
Nozzle	Spray pattern	Operating conditions	Fuel	$\dot{m}_{measured}$ [g/s]	$\dot{m}_{CFD}$ [g/s]	$100*(\dot{m}_{CFD} - \dot{m}_{measured})/\dot{m}_{measured}$	Error* [%]
A		101 vs 1bar	Stoddard	6.86	7.16	4.2	2.2
A		110 vs 10 bar	N-heptane	6.8	7.10	4.2	2.5
B1		351 vs 1 bar	N-heptane	12.6	13.05	3.5	1.5
B2		351 vs 1 bar	N-heptane	12.2	12.55	2.9	0.9
B3		101 vs 1 bar	Stoddard	6.8	7.03	3.4	1.4
C		101 vs 1 bar	N-heptane	7.21	7.48	3.7	1.6
C		110 vs 10 bar	N-heptane	7.4	7.79	5.3	3.2
D		100 vs 1 bar	N-heptane	5.95	6.02	1.2	-0.8
E1		200 vs 1 bar	N-heptane	8.91	9.06	1.7	-0.3
E2		101 vs 1 bar	Stoddard	7.95	8.15	2.5	0.5

Table 4.7: Mass flow rate prediction validation. *total error computed under the assumption of 4% pressure loss from the rail leading to 2% impact on the flow

Chapter 5

Conclusions and future work

5.1 Conclusions

A simulation framework for the simulation of Diesel fuel and GDi injector nozzle flow under dynamic needle conditions was presented in this Thesis. The vertical movement of the needle was accounted with a mesh node interpolation technique consisting in the creation of two topologically identical grids, one for the lowest lift and one for the highest. Any intermediate lift is retrieved by linear interpolation of the grid node position for the two mentioned grids. The needle lift profile was obtained from either measurements from real sized transparent nozzle replicas or from 1D system simulations.

The simulations were performed with the commercial code ANSYS Fluent. The multiphase model employed consists on a 3-phase (liquid fuel, vapour fuel, air) homogeneous model where all phases share the same pressure, temperature and velocity. For Diesel fuel injection, a full compressible thermodynamic model for ISO4113 testing oil was implemented and the energy equation is considered. For GDi, compressibility of the phases is taken into account but not the thermal effects. Two cavitation models have been used in this thesis, Zwart-Gerber-Belamri model and a polynomial barotropic cavitation model. The implementation of the polynomial barotropic model was tested against the Rayleigh collapse of a vapour bubble embedded in high pressure liquid. It was confirmed that the polynomial barotropic cavitation models is capable of correctly capturing the collapse speed of vapour structures. Both cavitation models have been compared in the case of GDi injection, and although they provide similar mass flow rate predictions, when erosion is of interest the barotropic model is chosen for its capacity to predict the collapse speed of cavitation accurately.

Although LES is a high fidelity turbulence modelling approach and the prefered method for the flows studied in this thesis, its computational cost limits its applicability to the study to one injection hole and a geometrical sector with periodic boundary conditions. On the other hand, the URANS approach allows for the use of the full nozzle geometry at

reduced cost. The drawback is that the situational nature of the URANS approach needs the verification of the solutions by reference to experimental measurements or higher fidelity simulations such as LES.

The chosen sub-grid scale LES turbulence model was the WALE due to its correct behaviour close to the walls and in laminar regions. Special care was taken in designing high quality hexahedral meshes for the LES simulations. The mesh resolution in the bulk flow is calculated from the Taylor micro-scales, while additional refinement in the walls in performed to match a specific predefined y^+ value. The resulting grid resolution satisfies $y^+ < 10$ in all the walls of interest, and sub-grid scale viscosity ratio, $\mu_t/\mu < 10$ and is considered suitable for LES simulations. The time step in the simulations is chosen so that the convective Courant–Friedrichs–Lewy number satisfies $CFL \sim 1$. For designing the URANS meshes used in this thesis a more practical approach was taken. A study to asses the sensitivity of the mass flow rate with the mesh resolution was performed. With the optimal resolution obtained the capacity of the methodology to accurately predict the flow in 6 different GDi multi-hole was assessed, obtaining a maximum deviation with the measured flow of 3.2%.

The LES simulation methodology was validated in the the case of Diesel fuel injection against micro-visualisations of a pilot injection of a real sized transparent replica. Unlike previous studies dealing with single hole injectors of less industrial relevance, or studies in multi-hole injectors that did not have direct validation, this work combined both experiment and simulation in real sized Diesel fuel injector nozzles. Residual air is experimentally observed before the start of the injection in the form of bubbles. Capturing the compression and expansion of this air in the holes requires the inclusion of air compressibility effects. It was confirmed that void originating at the sac volume entry is cavitation formed by flow separation and shear. The flow void patterns observed in the injection hole are reproduced. Cavitation developing at the injection hole inlet and due to vortical structures coming from the sac is observed. The initial air contained inside the nozzle is also seen to expand in the hole. Therefore, the experimentally observed void could potentially be a combination of both cavitating fuel and air. At the end of the injection, the simulation predicts cavitation in the sac volume compatible with the observed experimental void. After the needle closure the simulation clarified the mechanism behind air entrainment into the sac volume and cavitation collapse due to the sac volume pressure balancing with the ambient. The flow remaining in the sac volume between injections is therefore highly likely to be a mixture of liquid and air. This air is expected to aggregate into the initially observed bubbles due to surface tension.

The simulation methodology was then applied to the prediction of erosion prone areas in GDi nozzles operated with E100 fuel. Internal durability tests performed at Delphi Technologies for 400 million injection cycles reported erosion damage in GDi nozzles at

different locations namely, in the needle seat sealing band, sac volume entry, injection hole inlet and sac volume centre. In this case the barotropic cavitation model was used since it is deemed more suitable than the standard ZGB model due to its capacity of predicting cavitation collapse. Both LES and URANS approaches were compared, as well as the impact of the initialisation of the flow in the case of URANS. The mechanisms behind the different erosion locations are elucidated. The sac volume entry damage is caused by cavitation created in the small gap between the needle valve and the injector housing. The needle seat sealing band damage can be traced back to the needle valve closure and the creation of a ring of vapour that collapses towards the sealing band. Finally, the sac volume centre damage can be attributed to the collapse of cavitation arising in the sac volume after the end of the injection. The initial flow state of the sac is shown to have an impact on the amount of vapour predicted at the beginning of an injection due to the residual liquid being prone to cavitate; otherwise the phenomena predicted are essentially identical. In order to identify locations with high cavitation risk from the flow predictions, three indicators found in the literature were evaluated. The evaluated indicators were the maximum pressure recorded on the walls of the injector, the accumulated pressure derivatives and the accumulated erosive power. In the case of LES the proper resolution of the velocity and flow fields makes the choice of indicator less relevant; the maximum recorded pressure and the accumulated erosive power both showed good agreement with SEM hardware images after the durability tests; however the accumulated pressure derivative indicator agreement is rated as poorer. The reason is that this last indicator accounts for all pressure variations not just the pressure variations associated with cavitation collapse. In the case of URANS the reduced spatial and temporal resolution resulted in the maximum pressure indicator not being useful. Nevertheless, the accumulated erosive power indicator showed good agreement with the erosion hardware images since it relies on cavitation being correctly predicted in the right locations; the cavitating flow regions did not substantially change between URANS or LES. The accumulated pressure derivative also performed poorly in URANS for the same reason as in LES. Based on this results it is concluded that the cheaper URANS simulation approach can support the interpretation of hardware durability test in the case of GDi injectors.

5.2   Industrial impact

The numerical simulation framework developed has been fully integrated in the GDi injector design process at Delphi Technologies. Previous modelling work at Delphi Technologies did not account for cavitation. The method has been used for example to identify the impact of real world manufacturing tolerances on mass flow rate and force on the needle valve, provide input conditions for Lagrangian spray simulations (one-way coupling) [89],

support durability test results by providing physical interpretation of erosion patterns and asses the performance of different design options in the prototype phase among other uses. An example of how design performance can be assessed by simulation is now provided.

Assessment of the end of injection sac purging against tip residual fuel measurements

The particulate emission in GDi engines is known to be linked to the residual liquid in the sac after the injection [10, 12]. One industrial application of the numerical framework has been to determine the sac volume shape design performance in terms of how much residual liquid is left in the sac volume after the end of injection. The work shown in this section was partially carried out by Ramesh under the author's supervision. Figure 5.1-top shows the two different sac volume shape designs that have been evaluated.

A URANS simulation with injection pressure of $100bar$ was performed for each design. The employed cavitation model was the barotropic cavitation model adapted to N-heptane at 30^oC. Figure 5.1-bottom, shows the predictions for the average volume fraction of each phase inside the sac volume. It can be seen that $0.5ms$ after the end of the injection the prediction for design CR15 is that 55% of the sac volume is occupied with liquid fuel while for design CU68 48% of the sac volume is occupied with liquid fuel. These results can be compared to the measured mass of liquid remaining in the sac volume at the end of the injection, tip residual fuel measurement (TRF). For the TRF measurement principle and setup the reader should refer to [183]. Table 5.1 presents the comparison between the measured results $\sim 25ms$ after the end of the injection and the CFD predictions; even if the absolute value with the measurement is different the observed trend is correct. A possible explanation is that in the experiment there is enough time for some of the N-heptane to evaporate, since it is known to be volatile and evaporation is not modelled in the simulation. This is an example of how design performance can be ranked with the developed method.

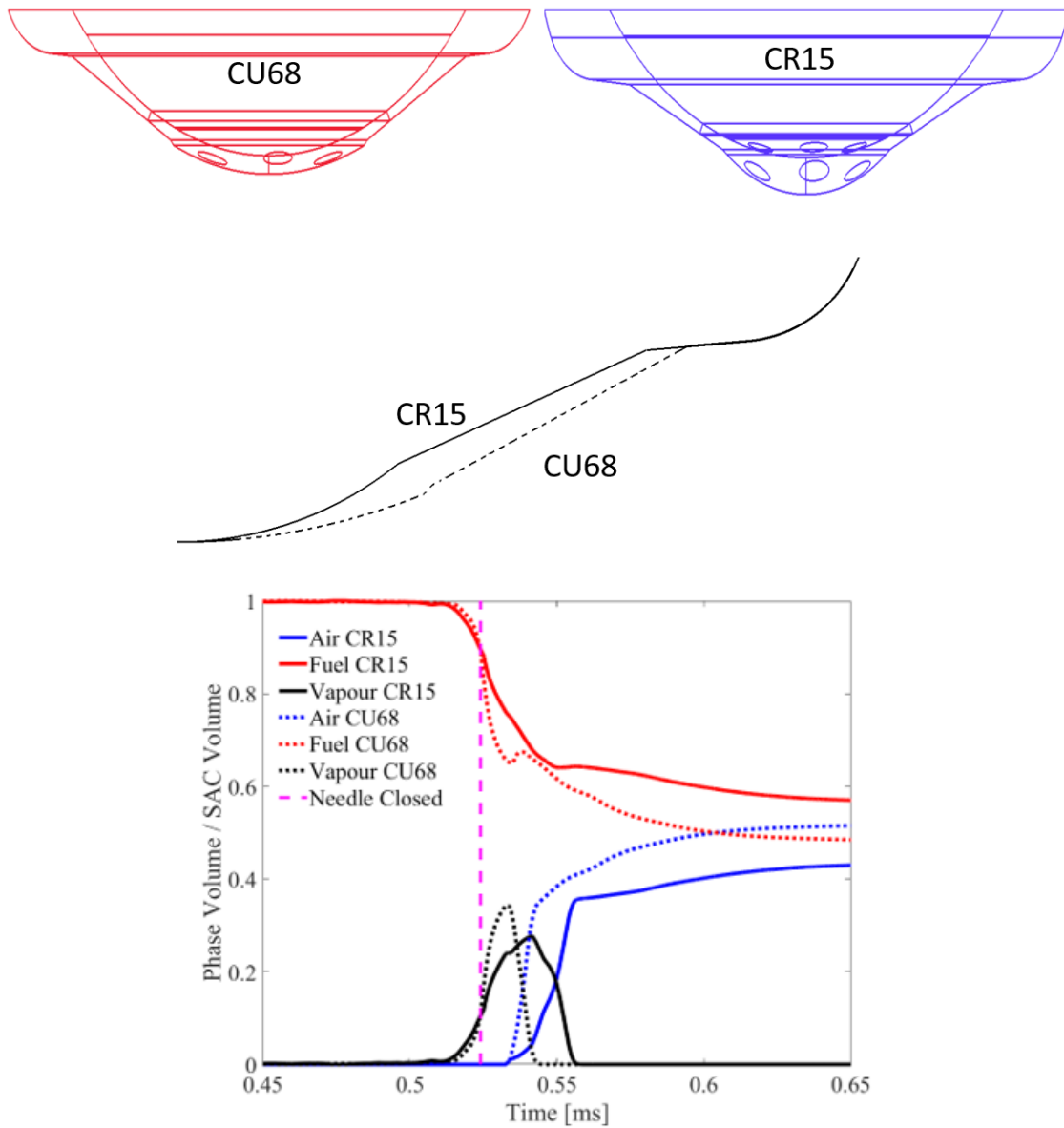Figure 5.1: Sac volume design comparison. Sac volume designs evaluated (top) and simulation volume fraction predictions (bottom)

Sac volume design	Quantity	CFD prediction	TRF measurement
CU68	Mass liquid $[\mu g]$	9.17	3.54
	Fuel volume fraction	0.48	
CR15	Mass liquid $[\mu g]$	18.1	9.12
	Fuel volume fraction	0.55	

Table 5.1: CFD vs experiment.

5.3 Future work

Based on the research presented and my own experience my recommendations for future work are the following:

- **Need for automatic pre-processing CAD and meshing tools.** It is in the author's experience that CAD and meshing can be a huge bottleneck in industrial CFD. Research on automatic tools to handle geometrical files and the automatic parametrisation of geometrical features would greatly speed up the work of both researchers and engineers worldwide. There is also a need to produce high quality, user independent meshes both for URANS and LES applications. One potential solution is to resort to the Immersed Boundary method [184] which can deal with arbitrary movement of boundaries and has been applied in fuel injection simulations [52, 148]. Even if CFD commercial codes such as Converge exist, to my best knowledge there is no tool that preprocesses a geometry and provides a high quality mesh in "one click"; in my opinion that should the sought paradigm.

- **Assessing real nozzle geometry effects and the impact of manufacturing tolerances.** Although very recent efforts have been devoted to understand the effect of real geometrical defects of the injector nozzle in the flow and the near nozzle spray [72, 185], it is the author's experience that these effects can be very relevant to accurately make injector nozzle flow predictions and further knowledge on their impact has to be acquired.

- **Cavitation coupled to wall damage.** Even if recent efforts have been devoted to coupling cavitation with wall deformation [186], such tools are far away from being widely employed in the industry

- **Near nozzle flow primary breakup, atomisation and its link to cavitation.** Extending the simulation methodology presented in this thesis to the near nozzle flow and primary breakup simulation can breach the link between the nozzle flow and the primary breakup behaviour. Although explored to some extent by the author [12, 84], no peered review scientific paper was published due to lack of validation and certainty on the results. Even if the link of cavitation and primary breakup has been recently studied in scaled up nozzles at low injection pressures [187, 96, 188, 189], there is evidence that at high injection pressures, cavitation is numerically predicted inside the near nozzle spray. Although not explicitly mentioned, evidence can be seen from the vapour visualisations in the near spray region presented in this thesis as well as in [12, 84]. This fact is also explicitly mentioned in [190] for GDi transparent replica nozzle flow simulations or just hinted from the visualisations of Diesel fuel

injection in [52]. In any case, to the best of my knowledge there is no experimental technique that neither verifies or disproves this prediction.

- **Simulations of closing spray.** Simulations reported in [148] attempt to predict the wall wetting at the end of injection. Further research on the topic to assess how the sac volume shape, injector hole orifices shape and other geometrical parameters affect the wall wetting and attempts to link this wetting with emission performance should be made.

- **Adaptive grid refinement of LES and near nozzle flow simulations.** The high cost of resolving the nozzle flow and near nozzle spray with LES makes resorting to adaptive grid refinement likely needed. However to my knowledge, no work is available employing local adaptive grid refinement based on the local flow conditions for the injector nozzle flow simulation. Work on the near nozzle spray is scarce and/or for conditions far from those found in real fuel injection applications.

- **Linking the nozzle flow characteristics with the near spray and far spray.** The most important goal of any research in the field under study (aside from durability assessment of components), should be to link the injector nozzle design with the nozzle flow charachteristics (vortex and cavitation patterns), with the near spray characteristics (spray morphology, ligament size, breakup modes) and the far spray characteristics (such as spray penetration, spray angle and spray momentum). I do not know of any holistic theory or method that is able to do this and be industrially practical, even if there have been multiple attempts [74, 89, 75].

- **Using Artificial Intelligence to obtain an optimal injector nozzle design based on historical data of simulation nozzle flow and experiments.** In the current era, we are witnessing the rise of Artificial Intelligence and Machine Learning, it would not be wise not to test such methods for obtaining optimal injector nozzle designs for specific engine applications based on historical experimental and simulation result databases available for instance at Delphi Technologies. However to the best of my knowledge such methods either have not been attempted or have not been published.

Bibliography

[1] R D Reitz, H Ogawa, R Payri, T Fansler, S Kokjohn, Y Moriyoshi, AK Agarwal, D Arcoumanis, D Assanis, C Bae, K Boulouchos, M Canakci, S Curran, I Denbratt, M Gavaises, M Guenthner, C Hasse, Z Huang, T Ishiyama, B Johansson, TV Johnson, G Kalghatgi, M Koike, SC Kong, A Leipertz, P Miles, R Novella, A Onorati, M Richter, S Shuai, D Siebers, W Su, M Trujillo, N Uchida, B M Vaglieco, RM Wagner, and H Zhao. Ijer editorial: The future of the internal combustion engine. *International Journal of Engine Research*, 21(1):3–10, 2020. `https://doi.org/10.1177/1468087419877990`.

[2] Outlook for energy: a perspective for 2040. Technical report, Exxon Mobile, 2019. `https://corporate.exxonmobil.com/-/media/Global/Files/outlook-for-energy/2019-Outlook-for-Energy_v4.pdf` - Last accesed 6th April 2020.

[3] A technical summary of euro 6/vi vehicle emission standards. Technical report, The international council for clean transportation, 2016. `https://theicct.org/publications/technical-summary-euro-6vi-vehicle-emission-standards` - Last accesed 6th April 2020.

[4] D. A. Pierpont, D. T. Montgomery, and Rolf D. Reitz. Reducing particulate and nox using multiple injections and egr in a d.i. diesel. In *SAE Technical Paper*. SAE International, 1995. `https://doi.org/10.4271/950217`.

[5] Shigeru Shundoh, Masanori Komori, Kinji Tsujimura, and Shinji Kobayashi. Nox reduction from diesel combustion using pilot injection with high pressure fuel injection. In *SAE Technical Paper*. SAE International, 1992. `https://doi.org/10.4271/920461`.

[6] G. M. Bianchi, P. Pelloni, F. E. Corcione, and F. Luppino. Numerical analysis of passenger car hsdi diesel engines with the 2nd generation of common rail injection systems: The effect of multiple injections on emissions. In *SAE 2001 World Congress*. SAE International, mar 2001. `https://doi.org/10.4271/2001-01-1068`.

[7] D. T. Montgomery and Rolf D. Reitz. Six-mode cycle evaluation of the effect of egr and multiple injections on particulate and nox emissions from a d.i. diesel engine. In *International Congress & Exposition*. SAE International, feb 1996. `https://doi.org/10.4271/960316`.

[8] K. Omae, T. Tomoda, H. Hashimoto, S. Matsumoto, A. Tanaka, and K. Uchiyama. Innovative fuel injection system for future toyota diesel passenger cars. In *Aachener Kolloquium*, 2012.

[9] M. Ikemoto, K. Shimode, K. Omae, and N.Toda. Diesel spray and combustion development using nozzle flow visualization , spray and combustion analyses. In *Proceedings of International Congress : SIA Powertrain -Rouen*, 2016.

[10] Axel Berndorfer, Stephan Breuer, Walter Piock, and Paul Von Bacho. Diffusion combustion phenomena in gdi engines caused by injection process. In *SAE 2013 World Congress & Exhibition*. SAE International, apr 2013. `https://doi.org/10.4271/2013-01-0261`.

[11] M. Raza, L. Chen, F. Leach, and S. Ding. A review of particulate number (pn) emissions from gasoline direct injection (gdi) engines and their control techniques. *Energies*, (1417), November 2018. `https://doi.org/10.3390/en11061417`.

[12] Junmei Shi, Eduardo Gomez Santos, Guy Hoffmann, and Gavin Dober. Large eddy simulation as an effective tool for gdi nozzle development. *MTZ worldwide*, 79:58–63, October 2018. `https://doi.org/10.1007/s38313-018-0089-2`.

[13] Martin Brandt, Alexander Hettinger, Andreas Schneider, Hartwig Senftleben, and Tim Skowronek. Extension of operating window for modern combustion systems by high performance ignition. In Michael Günther and Marc Sens, editors, *Ignition Systems for Gasoline Engines*, pages 26–51, Cham, 2017. Springer International Publishing. `https://doi.org/10.1007/978-3-319-45504-4_2`.

[14] Arthur Lefebvre. *Atomization and Sprays*. CRC Press, 1988.

[15] Carsten Baumgarten. *Mixture Formation in Internal Combustion Engines*. Springer-Verlag Berlin Heidelberg, 2006.

[16] C. Arcoumanis, H. Flora, M. Gavaises, and M. Badami. Cavitation in real-size multi-hole diesel injector nozzles. In *SAE 2000 World Congress*. SAE International, mar 2000. `https://doi.org/10.4271/2000-01-1249`.

[17] J. Shi, P. Aguado Lopez, G. Dober, N. Guerrassi, W. Bauer, and M. Lai. Using les and x-ray imaging to understand the influence of injection hole geometry on diesel spray formation. In *Thiesel, Valencia*, 2016.

[18] A. Andriotis and Manolis Gavaises. Influence of vortex flow and cavitation on near-nozzle diesel spray dispersion angle. *Atomization and Sprays*, 19:247–261, 01 2009. `10.1615/AtomizSpr.v19.i3.30`.

[19] J. Shi, P. Aguado Lopez, E. Gomez Santos, N. Guerrassi, G. Dober, W. Bauer, M. Lai, and J. Wang. Evidence of vortex driven primary breakup in high pressure fuel injection. In *Proceedings of the 28th Conference on Liquid Atomization and Spray Systems, ILASS Europe, Valencia*, 2017. `http://dx.doi.org/10.4995/ILASS2017.2017.5707`.

[20] Phoevos Koukouvinis, Manolis Gavaises, Jason Li, and Lifeng Wang. Large eddy simulation of diesel injector including cavitation effects and correlation to erosion damage. *Fuel*, 175:26 – 39, 2016. `https://doi.org/10.1016/j.fuel.2016.02.037`.

[21] A. Andriotis, M. Gavaises, and C. Arcoumanis. Vortex flow and cavitation in diesel injector nozzles. *Journal of Fluid Mechanics*, 610:195–215, 2008. `https://doi.org/10.1017/S0022112008002668`.

[22] N. Mitroglou, M. Lorenzi, M. Santini, and M. Gavaises. Application of x-ray micro-computed tomography on high-speed cavitating diesel fuel flows. *Experiments in Fluids*, 57(11):175, November 2016. `https://doi.org/10.1007/s00348-016-2256-z`.

[23] Daniel J Duke, Katarzyna E Matusik, Alan L Kastengren, Andrew B Swantek, Nicholas Sovis, Raul Payri, Juan P Viera, and Christopher F Powell. X-ray radiography of cavitation in a beryllium alloy nozzle. *International Journal of Engine Research*, 18(1-2):39–50, 2017. `https://doi.org/10.1177/1468087416685965`.

[24] H. Chaves, R. Miranda, and R. Knake. Particle image velocimetry measurements of the cavitating flow in a real size transparent vco nozzle. In *Proceedings of the 22nd European conference on liquid atomization and spray systems, ILASS, Como*, 2008. `https://doi.org/10.1017/jfm.2013.32`.

[25] Ioannis K. Karathanassis, Phoevos Koukouvinis, Efstathios Kontolatis, Zhilong Lee, Jin Wang, Nicholas Mitroglou, and Manolis Gavaises. High-speed visualization of vortical cavitation using synchrotron radiation. *Journal of Fluid Mechanics*, 838:148–164, 2018. `https://doi.org/10.1017/jfm.2017.885`.

[26] Jin Wang. X-ray vision of fuel sprays. *Journal of Synchrotron Radiation*, 12(2):197–207, Mar 2005.

[27] Sebastian Bornschlegel, Chris Conrad, Alexander Durst, Jin Wang, and Michael Wensing. Multi-hole gasoline direct injection:in-nozzle flow and primary breakup

investigated in transparent nozzlesand with x-ray. *International Journal of Engine Research*, 19(1):67–77, 2018. `https://doi.org/10.1177/1468087417746860`.

[28] Manuel A. Reddemann, Florian Mathieu, and Reinhold Kneer. Transmitted light microscopy for visualizing the turbulent primary breakup of a microscale liquid jet. *Experiments in Fluids*, 54(11):1607, October 2013. `https://doi.org/10.1007/s00348-013-1607-2`.

[29] Weidi Huang, Seoksu Moon, Jin Wang, Kei Murayama, Toshiyuki Arima, Yuzuru Sasaki, and Akira Arioka. Nozzle tip wetting in gasoline direct injection injector and its link with nozzle internal flow. *International Journal of Engine Research*, 21(2):340–351, 2020. `https://doi.org/10.1177/1468087419869774`.

[30] Michael Wensing, Thomas Vogel, and Gudrun Gotz. Transition of diesel spray to a supercritical state under engine conditions. *International Journal of Engine Research*, 17(1):108–119, 2016. `https://doi.org/10.1177/1468087415604281`.

[31] Piotr Strek, Daniel Duke, Andrew Swantek, Alan Kastengren, Christopher F. Powell, and David P. Schmidt. X-ray radiography and cfd studies of the spray g injector. In *SAE Technical Paper*. SAE International, 04 2016. `https://doi.org/10.4271/2016-01-0858`.

[32] I. H. Sezal, S. J. Schmidt, G. H. Schnerr, M. Thalhamer, and M. Förster. Shock and wave dynamics in cavitating compressible liquid flows in injection nozzles. *Shock Waves*, 19(1):49–58, Apr 2009. `https://doi.org/10.1007/s00193-008-0185-3`.

[33] Phoevos Koukouvinis, Homa Naseri, and Manolis Gavaises. Performance of turbulence and cavitation models in prediction of incipient and developed cavitation. *International Journal of Engine Research*, 18(4):333–350, 2017. `https://doi.org/10.1177/1468087416658604`.

[34] Andreas Theodorakakos, George Strotos, Nicholas Mitroglou, Chris Atkin, and Manolis Gavaises. Friction-induced heating in nozzle hole micro-channels under extreme fuel pressurisation. *Fuel*, 123:143 – 150, 2014. `https://doi.org/10.1016/j.fuel.2014.01.050`.

[35] George Strotos, Phoevos Koukouvinis, Andreas Theodorakakos, Manolis Gavaises, and George Bergeles. Transient heating effects in high pressure diesel injector nozzles. *International Journal of Heat and Fluid Flow*, 51:257 – 267, 2015. `https://doi.org/10.1016/j.ijheatfluidflow.2014.10.010`.

[36] J. Shi, N. Guerrassi, G. Dober, K. Karimi, and Y. Meslem. Complex physics modelling of diesel injector nozzle flow and spray supported by new experiments. In *Thiesel, Valencia*, 2014.

[37] Richard Saurel and Olivier Lemetayer. A multiphase model for compressible flows with interfaces, shocks, detonation waves and cavitation. *Journal of Fluid Mechanics*, 431:239–271, 2001. `https://doi.org/10.1017/S0022112000003098`.

[38] Michele Battistoni, Sibendu Som, and Douglas Longman. Comparison of mixture and multi-fluid models for in-nozzle cavitation prediction. In *Proceedings of ASME Internal Combustion Engine Division Fall Technical Conference, ICEF, Dearborn*, 10 2013.

[39] M.M. Awad and Y.S. Muzychka. Effective property models for homogeneous two-phase flows. *Experimental Thermal and Fluid Science*, 33(1):106 – 113, 2008. `https://doi.org/10.1016/j.expthermflusci.2008.07.006`.

[40] P. J. Zwart, A. G. Gerber, and T. Belamri. A two-phase flow model for predicting cavitation dynamics. In *Proceedings of the International Conference on Multiphase Flow, ICMF, Yokohama*, 2004.

[41] Steffen J. Schmidt, Michael Mihatsch, Matthias Thalhamer, and Nikolaus A. Adams. Assessment of the prediction capability of a thermodynamic cavitation model for the collapse characteristics of a vapor-bubble cloud. In *In Proceedings of the WIMRC, 3rd International Cavitation Forum 2011, Warwick, UK*, 2011.

[42] Christian P. Egerer, Stefan Hickel, Steffen J. Schmidt, and Nikolaus A. Adams. Large-eddy simulation of turbulent cavitating flow in a micro channel. *Physics of Fluids*, 26(8):085102, 2014. `https://doi.org/10.1063/1.4891325`.

[43] Phoevos Koukouvinis, Nicholas Mitroglou, Manolis Gavaises, Massimo Lorenzi, and Maurizio Santini. Quantitative predictions of cavitation presence and erosion-prone locations in a high-pressure cavitation test rig. *Journal of Fluid Mechanics*, 819:21–57, 2017.

[44] A. Kolmogorov. The Local Structure of Turbulence in Incompressible Viscous Fluid for Very Large Reynolds Numbers. *Akademiia Nauk SSSR Doklady*, 30:301–305, 1941.

[45] Florian R. Menter. Best practice: scale-resolving simulations in ansys cfd. In *ANSYS Technical report*, 2015.

[46] Stephen B. Pope. *Turbulent Flows*. Cambridge University Press, 2000.

[47] H. Tennekes and J.L. Lumley. *A First Course in Turbulence*. MIT Press, 1972.

[48] Jun-Mei Shi, K. Wenzlawski, Jerome Helie, Hans Nuglisch, and J. Cousin. Urans and sas analysis of flow dynamics in a gdi nozzle. In *ILASS*, 01 2010.

[49] Michele Battistoni, Qingluan Xue, and Sibendu Som. Large-eddy simulation (les) of spray transients: Start and end of injection phenomena. *Oil Gas Sci. Technol. - Rev. IFP Energies nouvelles*, 71(1):4, 2016. https://doi.org/10.2516/ogst/2015024.

[50] J-L. Reboud, B. Stutz, and O. Coutier-Delgosha. Two-phase flow structure of cavitation: experiment and modelling of unsteady effects. In *Proceedings of the third international symposium on cavitation, Grenoble*, 1998.

[51] O. Coutier-Delgosha, J. L. Reboud, and Y. Delannoy. Numerical simulation of the unsteady behaviour of cavitating flows. *International Journal for Numerical Methods in Fluids*, 42(5):527–548, 2003. https://doi.org/10.1002/fld.530.

[52] Felix Orley, Stefan Hickel, Steffen J Schmidt, and Nikolaus A Adams. Large-eddy simulation of turbulent, cavitating fuel flow inside a 9-hole diesel injector including needle movement. *International Journal of Engine Research*, 18(3):195–211, 2017. https://doi.org/10.1177/1468087416643901.

[53] A. Gosman and E. Ioannides. Aspects of computer simulation of liquid-fuelled combustors. In *19th Aerospace Sciences Meeting*. https://doi.org/10.2514/6.1981-323.

[54] Rolf D. Reitz. Modeling atomization processes in high-pressure vaporizing sprays. *Atomisation Spray Technology*, 3(4):309–337, January 1987.

[55] Peter J. O'Rourke and Anthony A. Amsden. The tab method for numerical calculation of spray droplet breakup. In *SAE Technical Paper*. SAE International, 11 1987.

[56] P.J. O'Rourke. *Collective Drop Effects on Vaporizing Liquid Sprays*. PhD thesis, Princeton, New Jersey, 1981.

[57] David P. Schmidt and C.J. Rutland. A new droplet collision algorithm. *Journal of Computational Physics*, 164(1):62 – 80, 2000.

[58] Donald W. Stanton and Christopher J. Rutland. Modeling fuel film formation and wall interaction in diesel engines. In *SAE Technical Paper*. SAE International, 02 1996.

[59] G. Bella, V. Rocco, and S. Ubertini. Combustion and spray simulation of a di turbocharged diesel engine. In *SAE Technical Paper*. SAE International, 10 2002.

[60] Yunqing Liu, Yuan Shen, Yi You, and Fuquan Zhao. Numerical simulation on spray atomization and fuel-air mixing process in a gasoline direct injection engine. In *SAE Technical Paper*. SAE International, 04 2012.

[61] Ariane Vallet and Roland Borghi. Modelisation eulerienne de l'atomisation d'un jet liquide. *Comptes Rendus de l'AcadÃ©mie des Sciences - Series IIB - Mechanics-Physics-Astronomy*, 327(10):1015 – 1020, 1999.

[62] Jeremy Chesnel, Julien Reveillon, Thibaut Menard, and F.X. Demoulin. Large eddy simulation of liquid jet atomization. *Atomization and spray*, 21:711–736, 01 2012.

[63] M. Ishii and K. Mishima. Two-fluid model and hydrodynamic constitutive relations. *Nuclear Engineering and Design*, 82(2):107 – 126, 1984.

[64] Milan Vujanovic, Zvonimir Petranovic, Wilfried Edelbauer, Jakov Baleta, and Neven Duic. Numerical modelling of diesel spray using the eulerian multiphase approach. *Energy Conversion and Management*, 104:160 – 169, 2015. Special Issue on Sustainable development of energy, water and environment systems.

[65] C.W Hirt and B.D Nichols. Volume of fluid (vof) method for the dynamics of free boundaries. *Journal of Computational Physics*, 39(1):201 – 225, 1981.

[66] Ruben Scardovelli and StÃ©phane Zaleski. Direct numerical simulation of free-surface and interfacial flow. *Annual Review of Fluid Mechanics*, 31(1):567–603, 1999.

[67] Stanley Osher and James A Sethian. Fronts propagating with curvature-dependent speed: Algorithms based on hamilton-jacobi formulations. *Journal of Computational Physics*, 79(1):12 – 49, 1988.

[68] Mark Sussman and Elbridge Gerry Puckett. A coupled level set and volume-of-fluid method for computing 3d and axisymmetric incompressible two-phase flows. *Journal of Computational Physics*, 162(2):301 – 337, 2000.

[69] Daniel Fuster, Anne Bague, Thomas Boeck, Luis [Le Moyne], Anthony Leboissetier, Stephane Popinet, Pascal Ray, Ruben Scardovelli, and Stephane Zaleski. Simulation of primary atomization with an octree adaptive mesh refinement and vof method. *International Journal of Multiphase Flow*, 35(6):550 – 565, 2009.

[70] J. Shinjo and A. Umemura. Simulation of liquid jet primary breakup: Dynamics of ligament and droplet formation. *International Journal of Multiphase Flow*, 36(7):513 – 532, 2010.

[71] M. Herrmann. The influence of density ratio on the primary atomization of a turbulent liquid jet in crossflow. *Proceedings of the Combustion Institute*, 33(2):2079 – 2088, 2011. `https://doi.org/10.1016/j.proci.2010.07.002`.

[72] Zongyu Yue, Michele Battistoni, and Sibendu Som. Spray characterization for engine combustion network spray g injector using high-fidelity simulation with detailed injector geometry. *International Journal of Engine Research*, 21(1):226–238, 2020. `https://doi.org/10.1177/1468087419872398`.

[73] Jeremy Chesnel, Julien Reveillon, F.X. Demoulin, and Thibaut Menard. Subgrid analysis of liquid jet atomization. *Atomization and Sprays*, 21, 01 2011.

[74] Bizhan Befrui, Giovanni Corbinelli, Mario D'Onofrio, and Daniel Varble. Gdi multi-hole injector internal flow and spray analysis. In *SAE 2011 World Congress & Exhibition*. SAE International, apr 2011.

[75] Mathis Bode, Tobias Falkenstein, Marco Davidovic, Heinz Pitsch, Hiroyoshi Taniguchi, Kei Murayama, Toshiyuki Arima, Seoksu Moon, Jin Wang, and Akira Arioka. Effects of cavitation and hydraulic flip in 3-hole gdi injectors. *SAE Int. J. Fuels Lubr.*, 10:380–393, 03 2017.

[76] Ming-Chia Lai, Yi Zheng, Xing-Bin Xie, Seoksu Moon, Zunping Liu, Jian Gao, Xusheng Zhang, Kamel Fezzaa, Jin Wang, and Junmei Shi. Characterization of the near-field spray and internal flow of single-hole and multi-hole sac nozzles using phase contrast x-ray imaging and cfd. *SAE Int. J. Engines*, 4:703–719, 04 2011.

[77] Ming-Chia Lai, Yi Zheng, Mark Shost, Xingbin Xie, Atsushi Matsumoto, Jin Wang, Xusheng Zhang, Seoksu Moon, Jian Gao, Kamel Fezzaa, Lars Zigan, Ingo Schmitz, Michael Wensing, and Alfred Leipertz. Characterization of internal flow and spray of multihole di gasoline spray using x-ray imaging and cfd. In *SAE International Powertrains, Fuels and Lubricants Meeting*. SAE International, aug 2011.

[78] Ming-Chia Lai, F. Wang, Xiaoxuan Xie, Jun-Mei Shi, Gavin Dober, Noureddine Guerrassi, Yann Meslem, Y. Gao, J Wang, E. Durfresne, and Seoksu Moon. Correlating the nozzle flow to spray and primary breakup using visualization and multiphase simulation. In *Conference: SIA Powertrain*, 05 2014.

[79] Eduardo Gomez Santos. Thermal-hydraulic phenomena in high pressure diesel injection systems. Master's thesis, ETSI Aeronauticos Madrid, 2015.

[80] Kristijan Krapic. Numerical approach for injector performance analysis under dynamic needle operations. Master's thesis, University of Stuttgart, 2016.

[81] Eduardo Gomez Santos, Junmei Shi, Manolis Gavaises, Celia Soteriou, Mark Winterbourn, and Wolfgang Bauer. Investigation of cavitation and air entrainment during pilot injection in real-size multi-hole diesel nozzles. *Fuel*, 2019. `https://doi.org/10.1016/j.fuel.2019.116746`.

[82] E. Gomez Santos, J. Shi, W. Bauer, and M. Gavaises. Modelling and prediction of cavitation erosion in gasoline direct injection injectors operated with e100 fuel using a barotropic equation of state. In *Proceedings of the IMechE Fuel Systems Conference, London*, 2018.

[83] J. Shi, P. Aguado Lopez, E. Gomez Santos, N. Guerrasi, W. Bauer, M.-C. Lai, and J. Wang. High pressure diesel spray development: the effect of nozzle geometry and flow vortex dynamics. In *Proceedings of the 14th International Conference on Liquid Atomization and Spray Systems, ICLASS, Chicago*, 2018.

[84] Eduardo Gomez Santos, Ramesh Venkatasubramanian, and Junmei Shi. Ansys hall of fame award. best in show commercial. 2018. `https://www.ansys.com/other/hall-of-fame/archive/2018/delphi-technologies` - Last accesed 8th April 2020.

[85] *ANSYS Fluent*, 2018.

[86] Marco Cristofaro, Wilfried Edelbauer, Manolis Gavaises, and Phoevos Koukouvinis. Numerical simulation of compressible cavitating two-phase flows with a pressure-based solver. In *Proceedings of the 28th Conference on Liquid Atomization and Spray Systems, ILASS Europe, Valencia*, 09 2017. `http://dx.doi.org/10.4995/ILASS2017.2017.4629`.

[87] D.R.H. Beattie and P.B. Whalley. A simple two-phase frictional pressure drop calculation method. *International Journal of Multiphase Flow*, 8(1):83 – 87, 1982. `https://doi.org/10.1016/0301-9322(82)90009-X`.

[88] N.Z Aung and T Yuwono. Evaluation of mixture viscosity models in the prediction of two-phase flow pressure drops. *ASEAN Journal on Science and Technology for Development*, 29(2), 2012. `https://doi.org/10.29037/ajstd.58`.

[89] Kaushik Saha, Sibendu Som, Michele Battistoni, Yanheng Li, Eric Pomraning, and P. K. Senecal. Numerical investigation of two-phase flow evolution of in- and near-nozzle regions of a gasoline direct injection engine during needle transients, apr 2016.

[90] E.T. Baldwin, R.O. Grover, S.E. Parrish, D.J. Duke, K.E. Matusik, C.F. Powell, A.L. Kastengren, and D.P. Schmidt. String flash-boiling in gasoline direct injection simulations with transient needle motion. *International Journal of Multiphase Flow*, 87:90 – 101, 2016. `https://doi.org/10.1016/j.ijmultiphaseflow.2016.09.004`.

[91] P.G. Aleiferis, J. Serras-Pereira, A. Augoye, T.J. Davies, R.F. Cracknell, and D. Richardson. Effect of fuel temperature on in-nozzle cavitation and spray formation of liquid hydrocarbons and alcohols from a real-size optical injector for direct-

injection spark-ignition engines. *International Journal of Heat and Mass Transfer*, 53(21):4588–4606, 2010. `https://doi.org/10.1016/j.ijheatmasstransfer.2010.06.033`.

[92] Dmitrii Mamaikin, Tobias Knorsch, Philipp Rogler, Philippe Leick, and Michael Wensing. High speed shadowgraphy of transparent nozzles as an evaluation tool for in-nozzle cavitation behavior of gdi injectors. In *Conference: ILASS2017 - 28th European Conference on Liquid Atomization and Spray Systems*, 09 2017. `http://dx.doi.org/10.4995/ILASS2017.2017.4639`.

[93] C. Brennen. *Cavitation and bubble dynamics.* Oxford: Oxford University Press, 1995.

[94] Gunter Schnerr and J. Sauer. Physical and numerical modeling of unsteady cavitation dynamics. 05 2001.

[95] Michael Kinzel, Jules Lindau, and Robert Kunz. A unified homogenous multiphase cfd model for cavitation. In *Proceedings of the ASME 2017 Fluids Engineering Division Summer Meeting (FEDSM2017), Waikoloa*, 07 2017. `https://doi.org/10.1115/FEDSM2017-69363`.

[96] Murali-Girija Mithun, Phoevos Koukouvinis, and Manolis Gavaises. Numerical simulation of cavitation and atomization using a fully compressible three-phase model. *Phys. Rev. Fluids*, 3:064304, Jun 2018. `https://doi.org/10.1103/PhysRevFluids.3.064304`.

[97] Charles Song, Jianming He, Fayi Zhou, and Ge Wang. Numerical simulation of cavitating and non-cavitating flows over a hydrofoil. *Report prepared for the office of Naval Research U.S. Navy, Department of Defense*, page 83, 04 1997.

[98] *Data from NIST Standard Reference Database 69: NIST Chemistry WebBook.* `https://webbook.nist.gov/cgi/cbook.cgi?ID=142-82-5` last accessed 7th January 2020.

[99] J. P. Franc and J. M. Michel. *Fundamentals of Cavitation.* Kluwer Academic Publishers, 2005.

[100] Nikolay Kolev. *Multiphase Flow Dynamics 3: Turbulence, Gas Absorption and Release, Diesel Fuel Properties.* 01 2007.

[101] El Hadji Ibrahima Ndiaye, Jean-Patrick Bazile, Djamel Nasri, Christian Boned, and Jean Luc Daridon. High pressure thermophysical characterization of fuel used for testing and calibrating diesel injection systems. *Fuel*, 98:288 – 294, 2012. `https://doi.org/10.1016/j.fuel.2012.04.005`.

[102] Miroslaw Chorazewski, Fatiha Dergal, Terufat Sawaya, Ilham Mokbel, Jean-Pierre E. Grolier, and Jacques Jose. Thermophysical properties of normafluid (iso 4113) over wide pressure and temperature ranges. *Fuel*, 105:440 – 450, 2013. `https://doi.org/10.1016/j.fuel.2012.05.059`.

[103] Guillaume Watson, Claus K. Zeberg-Mikkelsen, Antoine Baylaucq, and Christian Boned. High-pressure density measurements for the binary system ethanol + heptane. *J. Chem. Eng. Data*, 51(1):112–118, January 2006. `https://doi.org/10.1021/je050261u`.

[104] *Data from Stoddard supplier.*

[105] M. McLorn. *Fundamental Behaviour of Valves Used in Diesel Fuel Injection Equipment.* PhD thesis, (Unpublished), City, University of London, 2013.

[106] Nicholas Mitroglou, Michael McLorn, Manolis Gavaises, Celia Soteriou, and Mark Winterbourne. Instantaneous and ensemble average cavitation structures in diesel micro-channel flow orifices. *Fuel*, 116:736 – 742, 2014. `https://doi.org/10.1016/j.fuel.2013.08.060`.

[107] M. Winterbourn, C. Soteriou, N. Mitroglou, M. Gavaises, and C. Daveau. Visualising injection events in a fully operational diesel injector with a multi-hole transparent tip. In *Thiesel, Valencia*, 2014.

[108] J. P. Van Doormaal and G. D. Raithby. Enhancements of the simple method for predicting incompressible fluid flows. *Numerical Heat Transfer*, 7(2):147–163, 1984. `https://doi.org/10.1080/01495728408961817`.

[109] Z.J. Chen and A.J. Przekwas. A coupled pressure-based computational method for incompressible/compressible flows. *Journal of Computational Physics*, 229(24):9150 – 9165, 2010. `https://doi.org/10.1016/j.jcp.2010.08.029`.

[110] J.H. Ferziger and M. Peric. *Computational Methods for Fluid Dynamics.* Springer Berlin Heidelberg, 2012.

[111] B.P. Leonard. The ultimate conservative difference scheme applied to unsteady one-dimensional advection. *Computer Methods in Applied Mechanics and Engineering*, 88(1):17 – 74, 1991. `https://doi.org/10.1016/0045-7825(91)90232-U`.

[112] F. R. Menter. Two-equation eddy-viscosity turbulence models for engineering applications. *AIAA Journal*, 32(8):1598–1605, 1994. `https://doi.org/10.2514/3.12149`.

[113] Lars Zigan, Junmei Shi, Ivan Krotow, Ingo Schmitz, Michael Wensing, and Alfred Leipertz. Fuel property and fuel temperature effects on internal nozzle flow, atomization and cyclic spray fluctuations of a direct injection spark ignition injector. *International Journal of Engine Research*, 14(6):543–556, 2013.

[114] George Bergeles, Jason Li, Lifeng Wang, Phoevos Koukouvinis, and Manolis Gavaises. An erosion aggressiveness index (eai) based on pressure load estimation due to bubble collapse in cavitating flows within the rans solvers. *SAE International Journal of Engines*, 8, 09 2015.

[115] Phoevos Koukouvinis, Ioannis K Karathanassis, and Manolis Gavaises. Prediction of cavitation and induced erosion inside a high-pressure fuel pump. *International Journal of Engine Research*, 19(3):360–373, 2018. `https://doi.org/10.1177/1468087417708137`.

[116] Ziru Li, Mathieu Pourquie, and Tom Terwisga. Assessment of cavitation erosion with a urans method. *Journal of Fluids Engineering*, 136:041101, 04 2014.

[117] G Erlebacher, M Y Hussaini, C G Speziale, and T A Zang. Toward the large-eddy simulation of compressible turbulent flows. *Journal of Fluid Mechanics*, 238:155–185, 1992.

[118] F. Nicoud and F. Ducros. Subgrid-scale stress modelling based on the square of the velocity gradient tensor. *Flow, Turbulence and Combustion*, 62(3):183–200, Sep 1999. `https://doi.org/10.1023/A:1009995426001`.

[119] Junmei Shi, Pablo Aguado Lopez, Noureddine Guerrassi, and Gavin Dober. Understanding high-pressure injection primary breakup by using large eddy simulation and x-ray spray imaging. *MTZ worldwide*, 78:50–57, 05 2017. `https://doi.org/10.1007/s38313-017-0039-4`.

[120] European-Comission. Commission regulation (eu) 2017/1151 of 1 june 2017, July 2017. `https://eur-lex.europa.eu/legal-content/EN/TXT/?uri=CELEX:02017R1151-20190101`.

[121] H. Afzal, C. Arcoumanis, M. Gavaises, and N. Kampanis. Internal flow in diesel injector nozzles modelling and experiments. In *Fuel injection systems. Proceedings*, 1999. `https://doi.org/10.1016/j.fuel.2013.08.060`.

[122] E. Giannadakis, M. Gavaises, and C. Arcoumanis. Modelling of cavitation in diesel injector nozzles. *Journal of Fluid Mechanics*, 616:153–193, 2008. `https://doi.org/10.1017/S0022112008003777`.

[123] F.J. Salvador, J.-V. Romero, M.-D. Rosello, and J. Martinez-Lopez. Validation of a code for modeling cavitation phenomena in diesel injector nozzles. *Mathematical and Computer Modelling*, 52(7):1123 – 1132, 2010. `https://doi.org/10.1016/j.mcm.2010.02.027`.

[124] Seoksu Moon, Weidi Huang, Zhilong Li, and Jin Wang. End-of-injection fuel dribble of multi-hole diesel injector: Comprehensive investigation of phenomenon and discussion on control strategy. *Applied Energy*, 179:7 – 16, 2016. `https://doi.org/10.1016/j.apenergy.2016.06.116`.

[125] Hyun Kyu Suh and Chang Sik Lee. Effect of cavitation in nozzle orifice on the diesel fuel atomization characteristics. *International Journal of Heat and Fluid Flow*, 29:1001–1009, 08 2008. `https://doi.org/10.1016/j.ijheatfluidflow.2008.03.014`.

[126] R. Miranda, H. Chaves, U. Martin, and F. Obermeier. Cavitation in a transparent real size vco injection nozzle. In *Proceedings of the 9th International conference on liquid atomisation and spray systems, ICLASS, Sorrento*, 2003.

[127] I. Gilles-Birth, M. Rechs, U. Spicher, and S. Bernhardt. Experimental investigation of the in-nozzle flow of valve covered orifice nozzles for gasoline direct injection. In *Proceedings of the 7th International symposium on internal combustion diagnostics, Baden-Baden*, 2006.

[128] C Arcoumanis, M Gavaises, H Flora, and H Roth. Visualisation of cavitation in diesel engine injectors. *Mecanique & Industries*, 2(5):375 – 381, 2001. `http://www.sciencedirect.com/science/article/pii/S1296213901011198`.

[129] H. Roth, E. Giannadakis, M. Gavaises, C. Arcoumanis, K. Omae, I. Sakata, M. Nakamura, and H. Yanagihara. Effect of multi-injection strategy on cavitation development in diesel injector nozzle holes. In *SAE 2005 World Congress & Exhibition*. SAE International, apr 2005. `https://doi.org/10.4271/2005-01-1237`.

[130] C. Arcoumanis, M. Gavaises, E. Abdul-Wahab, and V. Moser. Modeling of advanced high-pressure fuel injection systems for passenger car diesel engines. In *International Congress & Exposition*. SAE International, mar 1999. `https://doi.org/10.4271/1999-01-0910`.

[131] N. Mitroglou and M. Gavaises. Cavitation inside real-size fully transparent fuel injector nozzles and its effect on near-nozzle spray formation. In *DIPSI workshop on droplet impact phenomena and spray investigations, University of Bergamo, Italy*, 2011.

[132] G. Sridhar and J. Katz. Effect of entrained bubbles on the structure of vortex rings. *Journal of Fluid Mechanics*, 397:171–202, 1999. `https://doi.org/10.1017/S0022112099006187`.

[133] Andrew J. Cihonski, Justin R. Finn, and Sourabh V. Apte. Volume displacement effects during bubble entrainment in a travelling vortex ring. *Journal of Fluid Mechanics*, 721:225–267, 2013.

[134] Jaehyug Choi and Steven L. Ceccio. Dynamics and noise emission of vortex cavitation bubbles. *Journal of Fluid Mechanics*, 575:1–26, 2007. `https://doi.org/10.1017/S0022112006003776`.

[135] Jaehyug Choi, Chao-Tsung Hsiao, Georges Chahine, and Steven Ceccio. Growth, oscillation and collapse of vortex cavitation bubbles. *Journal of Fluid Mechanics*, 624:255–279, 2009. `https://doi.org/10.1017/S0022112008005430`.

[136] Sadegh Dabiri, William A. Sirignano, and Daniel D. Joseph. Interaction between a cavitation bubble and shear flow. *Journal of Fluid Mechanics*, 651:93–116, 2010. `https://doi.org/10.1017/S0022112009994058`.

[137] M. Blessing, G. Konig, C. Kruger, U. Michels, and V. Schwarz. Analysis of flow and cavitation phenomena in diesel injection nozzles and its effects on spray and mixture formation. In *SAE 2003 World Congress & Exhibition*. SAE International, mar 2003. `https://doi.org/10.4271/2003-01-1358`.

[138] M. Gavaises, D. Papoulias, A. Andriotis, E. Giannadakis, and A. Theodorakakos. Link between cavitation development and erosion damage in diesel injector nozzles. In *SAE World Congress & Exhibition*. SAE International, apr 2007. `https://doi.org/10.4271/2007-01-0246`.

[139] Benjamin Reid, Graham Hargrave, Colin P. Garner, and Graham Wigley. An investigation of string cavitation in a true-scale fuel injector flow geometry at high pressure. *Physics of Fluids*, 22, 03 2010. `https://doi.org/10.1063/1.3372174`.

[140] Manolis Gavaises, Benjamin Reid, Nicholas Mitroglou, Graham Hargrave, C.P. Garner, Edward Long, and Robert Mcdavid. On the formation of string cavitation inside fuel injectors. *Experiments in Fluids*, 55, 01 2014. `https://doi.org/10.1007/s00348-013-1662-8`.

[141] Russel Lockett and Alberto Bonifacio. Hydrodynamic luminescence in a model diesel injector return valve. *International Journal of Engine Research*, 07 2019. `https://doi.org/10.1177/1468087419870421`.

[142] L. Thimm, P. Trtik, H. Hansen, S. Jollet, and F. Dinkelacker. Experimental cavitation and spray measurement in real size diesel injection nozzles with high resolution neutron imaging. In *Proceedings of the 29th Conference on Liquid Atomization and Spray Systems, ILASS Europe, Paris*, 2019.

[143] R. P. Fitzgerald, G. Della Vecchia, J. E. Peraza, and G. C. Martin. Features of internal flow and spray for a multi-hole transparent diesel fuel injector tip. In *29th Conference on Liquid Atomization and Spray Systems, ILASS, Paris*, 2019.

[144] Andrea Emilio Catania, Stefano d'Ambrosio, Roberto Finesso, and Ezio Spessa. Effects of rail pressure, pilot scheduling and egr rate on combustion and emissions in conventional and pcci diesel engines. *SAE Int. J. Engines*, 3:773–787, 04 2010. `https://doi.org/10.4271/2010-01-1109`.

[145] Stephen Busch, Kan Zha, Paul C. Miles, Alok Warey, Francesco Pesce, Richard Peterson, and Alberto Vassallo. Experimental and numerical investigations of close-coupled pilot injections to reduce combustion noise in a small-bore diesel engine. *SAE Int. J. Engines*, 8:660–678, 04 2015. `https://doi.org/10.4271/2015-01-0796`.

[146] Stephen Busch, Kan Zha, Alok Warey, Francesco Pesce, and Richard Peterson. On the reduction of combustion noise by a close-coupled pilot injection in a small-bore direct-injection diesel engine. *Journal of Engineering for Gas Turbines and Power*, 138(10), 04 2016. `https://doi.org/10.1115/1.4032864`.

[147] Gavin Dober, Christophe Garsi, Noureddine Guerrassi, Harun Ismail, and Junmei Shi. Investigations of the spray structure of large and small diesel injections using spray momentum measurements and their link to injector performance. In *In Proceedings of SIA Powertrain Conference*, 06 2016.

[148] Martin Gold, Richard Pearson, Jack Turner, Dan Sykes, Viacheslav Stetsyuk, Guillaume de Sercey, Cyril Crua, Foivos Koukouvinis, Manolis Gavaises, and Murali-Girija Mithun. Simulation and measurement of transient fluid phenomena within diesel injection. *SAE Int. J. Adv. & Curr. Prac. in Mobility*, 1:291–305, 01 2019. `https://doi.org/10.4271/2019-01-0066`.

[149] Harun Ismail, Gavin Dober, Junmei Shi, Koroush Karimi, and Noureddine Guerrassi. Delphi technologies internal report. 2016.

[150] Gautam Kalghatgi. *Fuel/Engine Interactions*. SAE International, 2013.

[151] F. Moukalled, L. Mangani, and M. Darwish. *The Finite Volume Method in Computational Fluid Dynamics. An Advanced Introduction with OpenFOAM and Matlab.* Springer International Publishing, 1 edition, 2015.

[152] I. B. Celik, Z. N. Cehreli, and I. Yavuz. Index of Resolution Quality for Large Eddy Simulations. *Journal of Fluids Engineering*, 127(5):949–958, 09 2005. `https://doi.org/10.1115/1.1990201`.

[153] F. Brusiani and G. M. Bianchi. Les simulation of ice non-reactive flows in fixed grids. In *SAE Technical Paper*. SAE International, 04 2008. `https://doi.org/10.4271/2008-01-0959`.

[154] Frank Black. An overview of the technical implications of methanol and ethanol as highway motor vehicle fuels. In *SAE Technical Paper*. SAE International, 10 1991. `https://doi.org/10.4271/912413`.

[155] R. C. Hendricks, R. L. Mullen, and M. J. Braun. Analogy between fluid cavitation and fracture mechanics. In *Proceedings of the Thermal Engineering Conference, Honolulu*. American Society of Mechanical Engineers, 1983.

[156] Kassandra Makri, Russel Lockett, and Mahesh Jeshani. Dynamics of post-injection fuel flow in mini-sac diesel injectors part 1: Admission of external gases and implications for deposit formation. *International Journal of Engine Research*, 0(0):1468087419895425, 0. `https://doi.org/10.1177/1468087419895425`.

[157] A. Shima, K. Takayama, Y. Tomita, and N. Oshawa. Mechanism of impact pressure generation from spark-generated bubble collapse near a wall. *AIAA Journal*, 21(1):55–59, 1983. `https://doi.org/10.2514/3.8027`.

[158] Emil A. Brujan, David S. Hecht, Frank Lee, and Gary A. Williams. Properties of luminescence from laser-created bubbles in pressurized water. *Phys. Rev. E*, 72:066310, Dec 2005. `https://doi.org/10.1103/PhysRevE.72.066310`.

[159] Tom Terwisga, Erik Van Wijngaarden, Johan Bosschers, and Gert Kuiper. Achievements and challenges in cavitation research on ship propellers. *International Shipbuilding Progress*, 54:2–3, 01 2007.

[160] Maxwell Brunhart, Celia Soteriou, Christian Daveau, Manolis Gavaises, Phoevos Koukouvinis, and Mark Winterbourn. Cavitation erosion risk indicators for a thin gap within a diesel fuel pump. *Wear*, page 203024, 2019. `https://doi.org/10.1016/j.wear.2019.203024`.

[161] Michele Battistoni, Daniel Duke, Andrew B. Swantek, F. Zak Tilocco, Christopher F. Powell, and Sibendu Som. Effects of noncondensable gas on cavitating nozzles. *Atomization and Sprays*, 25(6):453–483, 2015. `https://doi.org/10.1615/AtomizSpr.2015011076`.

[162] Murali-Girija Mithun, Phoevos Koukouvinis, Ioannis K Karathanassis, and Manolis Gavaises. Numerical simulation of three-phase flow in an external gear pump using immersed boundary approach. *Applied Mathematical Modelling*, 72:682 – 699, 2019. `https://doi.org/10.1016/j.apm.2019.03.022`.

[163] M. Tinguely, D. Obreschkow, P. Kobel, N. Dorsaz, A. de Bosset, and M. Farhat. Energy partition at the collapse of spherical cavitation bubbles. *Phys. Rev. E*, 86:046315, Oct 2012. `https://doi.org/10.1103/PhysRevE.86.046315`.

[164] Theresa Trummler, Steffen Schmidt, and Nikolaus Adams. Large eddy simulation of a collapsing vapor bubble containing non-condensable gas. In *In Proceedings of 10th internationsal symposium on cavitation (CAV2018), Baltimore*, 05 2018. `https://cav2018.jhu.edu/wp-content/uploads/Trummler-Theresa.pdf` last accessed last accessed 8th November 2019.

[165] Takehiko Sato, Marc Tinguely, Masanobu Oizumi, and Mohamed Farhat. Evidence for hydrogen generation in laser- or spark-induced cavitation bubbles. *Applied Physics Letters*, 102(7):074105, 2013. `https://doi.org/10.1063/1.4793193`.

[166] P. Koukouvinis, M. Gavaises, O. Supponen, and M. Farhat. Numerical simulation of a collapsing bubble subject to gravity. *Physics of Fluids*, 28(3):032110, 2016. `https://doi.org/10.1063/1.4944561`.

[167] Chris Conrad, Sebastian Bornschlegel, Alexander Durst, Dominik Jordan, and Michael Wensing. Influence of the nozzle geometry on in-nozzle cavitation investigated in real-size glass nozzles with shadowgraphy and lif. In *ICLASS 2018, 14th Triennial International Conference on Liquid Atomization and Spray SystemsAt: Chicago, USA*, 07 2018.

[168] C.L. Merkle, J. Feng, and P.E.O. Buelow. Computational modeling of the dynamics of sheet cavitation. In *In Proceedings of the 3rd International Symposium on Cavitation, Grenoble, France*, 1998.

[169] Ebrahim Ghahramani and Rickard Bensow. Analysis of the finite mass transfer models in the numerical simulation of bubbly flows. 01 2018. `https://doi.org/10.1115/1.861851_ch18`.

[170] S. Schenke, T. Melissaris, and T. J. C. van Terwisga. On the relevance of kinematics for cavitation implosion loads. *Physics of Fluids*, 31(5):052102, 2019. `https://doi.org/10.1063/1.5092711`.

[171] Junmei Shi and Mohammad Arafin. Cfd investigation of fuel property effect on cavitating flow in generic nozzle geometries. In *ILASS Europe 2010, 23rd Annual*

Conference on Liquid Atomization and Spray Systems, Brno, Czech Republic, 01 2010.

[172] S Washio, S Fujiyoshi, and S Takahashi. Observation of cavitation inception in separating water flows through constricted channels. *Proceedings of the Institution of Mechanical Engineers, Part C: Journal of Mechanical Engineering Science*, 223(9):2071–2080, 2009. `https://doi.org/10.1243/09544062JMES1438`.

[173] Michael Simon Mihatsch. *Numerical Prediction of Erosion and Degassing Effects in Cavitating Flows*. Dissertation, Technische Universitat Munchen, Munchen, 2017.

[174] Christian Egerer. *Large-Eddy Simulation of Turbulent Cavitating Flows*. Dissertation, Technische Universitat Munchen, Munchen, 2016.

[175] Phoevos Koukouvinis and Manolis Gavaises. Simulation of throttle flow with two phase and single phase homogenous equilibrium model. *Journal of Physics: Conference Series*, 656:012086, 12 2015. `https://doi.org/10.1088/1742-6596/656/1/012086`.

[176] Regiane Fortes Patella, Antoine Archer, and Cedric Flageul. Numerical and experimental investigations on cavitation erosion. *IOP Conference Series: Earth and Environmental Science*, 15:2013–, 11 2012. `https://doi.org/10.1088/1755-1315/15/2/022013`.

[177] Themistoklis Melissaris, Norbert Bulten, and Tom Terwisga. *On Cavitation Aggressiveness and Cavitation Erosion on Marine Propellers using a URANS Method*. 01 2018. `https://doi.org/10.1115/1.861851_ch160`.

[178] C. Eskilsson and R. E. Bensow. Estimation of cavitation erosion intensity using cfd: numerical compariosn of three different methods. In *In Proceedings of the Fourth International Symposium on Marine Propulsors, Austin, Texas, USA*, 2015. `http://www.marinepropulsors.com/proceedings/2015/MA1-2.pdf` last accessed 8th November 2019.

[179] *Data from NIST Standard Reference Database 69: NIST Chemistry WebBook*. `https://webbook.nist.gov/cgi/cbook.cgi?ID=C64175&Mask=4&Type=ANTOINE&Plot=on#Refs` last accessed 12th November 2019.

[180] Soren Schenke and Tom J.C. van Terwisga. An energy conservative method to predict the erosive aggressiveness of collapsing cavitating structures and cavitating flows from numerical simulations. *International Journal of Multiphase Flow*, 111:200 – 218, 2019. `https://doi.org/10.1016/j.ijmultiphaseflow.2018.11.016`.

[181] A. Vogel and W. Lauterborn. Acoustic transient generation by laser produced cavitation bubbles near solid boundaries. *The Journal of the Acoustical Society of America*, 84(2):719–731, 1988. `https://doi.org/10.1121/1.396852`.

[182] Michael S. Mihatsch, Steffen J. Schmidt, and Nikolaus A. Adams. Cavitation erosion prediction based on analysis of flow dynamics and impact load spectra. *Physics of Fluids*, 27(10):103302, 2015.

[183] Gavin Dober. Influence of engine test conditions on nozzle tip coking and associated advanced diagnostic techniques. In *Conference: SAE Fuels and Lubricants Conference 2018, At Heidelberg, Germany*, 09 2018.

[184] Rajat Mittal and Gianluca Iaccarino. Immersed boundary methods. *Annual Review of Fluid Mechanics*, 37(1):239–261, 2005.

[185] Arpit Agarwal and Mario F Trujillo. The effect of nozzle internal flow on spray atomization. *International Journal of Engine Research*, 21(1):55–72, 2020.

[186] Prasanta Sarkar. *Simulation of cavitation erosion by a coupled CFD-FEM approach.* PhD thesis, Universite Grenoble Alpes, 2019.

[187] Felix Oerley, Theresa Trummler, Stefan Hickel, Michael Mihatsch, Steffen Schmidt, and Nikolaus Adams. Large-eddy simulation of cavitating nozzle flow and primary jet break-up. *Physics of Fluids*, 27:086101, 08 2015.

[188] Theresa Trummler, D. Rahn, S. J. Schmidt, and Nikolaus A. Adams. Large eddy simulations of cavitating flow in a step nozzle with injection into gas. *Atomization and Sprays*, 28(10):931–955, 2018.

[189] A. Ahmed, B. Duret, J. Reveillon, and F.X. Demoulin. Numerical simulation of cavitation for liquid injection in non-condensable gas. *International Journal of Multiphase Flow*, 127:103269, 2020.

[190] F Giussani, Federico Piscaglia, Jerome Helie, and S Aithal. A 3-phase solver for the simulation of internal nozzle cavitating flows in fuel-injectors using openfoam. In *ILASS Europe 2019, 29th Conference on Liquid Atomization and Spray Systems, 2-4 September 2019, Paris, France*, 09 2019.